Application of Surface Plasmonics for Semiconductor Light-Emitting Diodes

Fadil, Ahmed

Publication date:
2015

Document Version
Publisher's PDF, also known as Version of record

Ph.D. Thesis
Doctor of Philosophy

DTU Fotonik
Department of Photonics Engineering

Application of Surface Plasmonics for Semiconductor Light-Emitting Diodes

Ahmed Fadil

Kongens Lyngby
2015

DTU Fotonik
Department of Photonics Engineering
Technical University of Denmark

Ørsteds Plads
Building 343
2800 Kongens Lyngby, Denmark
Phone +45 4525 6352
info@fotonik.dtu.dk
www.fotonik.dtu.dk

Preface

This thesis was prepared at the Department of Photonics Engineering, Technical University of Denmark (DTU Fotonik) in partial fulfillment of the requirements for the degree of Doctor of Philosophy. The work presented here was carried out in the period from 1st July, 2012 to 30th November, 2015, at DTU Fotonik and the Department of Materials Science and Engineering, Meijo University, Japan.

The project was financed by Innovation Fund Denmark through the "Super Bright Light-Emitting Diodes" (SBLED) project (grant no. 0603-00494B), and supervised by:

- Haiyan Ou (main supervisor)
  Associate Professor, DTU Fotonik
- Carsten Dam-Hansen (co-supervisor)
  Senior Researcher, DTU Fotonik
- Paul Michael Petersen (co-supervisor)
  Professor, DTU Fotonik

Acknowledgements

During the span of this project, I have received help from many people to whom I would like to express my gratitude.

First and foremost I would like to thank my supervisors Prof. Haiyan Ou, Dr. Carsten Dam-Hansen and Prof. Paul Michael Petersen for their invaluable guidance throughout the years. In particular, I would like to thank Haiyan Ou for giving me the opportunity to work on this project, and for always being there with her insightful guidance, excellent mentoring and fruitful discussions. Thank you for all the moral support and encouragement even when things were not going well. I will always be grateful for introducing me to the micro-fabrication technology in field of LEDs. Thank you for being a wonderful supervisor.

A warm gratitude to Dr. Yuntian Chen, who supervised during the initial phases of the project and assisted throughout the years with fruitful discussions in the field of plasmonics. His insight on the theoretical aspects were invaluable in understanding the experimental results and highly appreciated.

I would also like to thank Dr. Daisuke Iida for growing all the LED wafers, and for sharing his knowledge and experience on the InGaN material system throughout the years, without which this project would not have been possible.

I am also grateful to Prof. Satoshi Kamiyama from Meijo University and his group for hosting and providing me the great opportunity to work with their group in Japan, and for growing GaN LED wafers for this project. Thank you Yamamoto, Tsuchiya, Kawai, Terashima, Kondo, Sowa and Ito for never being too busy to support and assist with the fabrication processes.

A sincere thanks to Prof. Zhiqiang Liu and Prof. Xiaoyan Yi from the Institute of Semiconductors, CAS in China for their collaboration on the project and providing their assistance with semiconductor processing. Thank you Jun Ma and Teng Zhang for your advice, and all the help with characterizing our samples.

A special thanks to Yiyu Ou for his advice and support from the beginning of the project. Thank you for teaching me all the characterization methods, helping me with the lab equipment, and providing brilliant ideas for the project.

I would also like to thank Oleksii Kopylov for valuable discussions on microfabrication processes and advice on electrical characterization methods.

Thanks to Xiaolong Zhu for his assistance and collaboration with the nanosphere lithography process, Kaiyu Wu for his assistance with Raman spectroscopy, and Weifang Lu for her assistance with XPS measurements.

I am also thankful for all the help provided by Dr. Dmitry Suyatin from Lund University in Sweden by giving us the opportunity to do GaN dry-etching using their ICP-RIE machine.

Many thanks to Jonas Michael-Lindhard, Jesper Hanberg, Conny Hjort and Berit Herstrøm from DTU Danchip for sharing their experience, and advising on cleanroom processing.

I would also like to thank my friends, colleagues and office mates, including our team-members Yiyu Ou, Meng Xiong, Weifang Lu, Li Lin, Jiehui Li, Yi Wei and Stanley Lim for their support.

Innovation Fund Denmark is also acknowledged for the financial support of the SBLED project.

Last but not least, I would like to thank my parents and my wife for their continuous support and patience with me during all these years in the university.

Abstract

This thesis addresses the lack of an efficient semiconductor light source at green emission colours. Considering InGaN based quantum-well (QW) light-emitters and light-emitting diodes (LEDs), various ways of applying surface plasmonics and nano-patterning to improve the efficiency, are investigated.
By placing metallic thin films or nanoparticles (NPs) in the near-field of QW light-emitters, it is possible to improve their internal quantum efficiency (IQE) through the Purcell enhancement effect. It has been a general understanding that in order to achieve surface plasmon (SP) coupling with QWs and thereby IQE enhancement, the metal NP resonance should match the emission wavelength. This criterion is critically analysed, and based on the experimental findings, a more complicated relation is revealed. The requirements which must be satisfied to avoid optical suppression are presented.
The SP-QW coupling does not necessarily lead to emission enhancement. The findings of this work show that the scattering and absorption properties of NPs play a crucial role in determining whether the implementation will improve or degrade the optical performance. By applying these principles, a novel design is presented to obtain light extraction efficiency (LEE) improvement through nano-patterning, and IQE improvement through SP-QW coupling.
Considering the fabrication process aspect, dry-etching damage on the semiconductor light-emitters from the nano-patterning is also addressed. Different ion-damage treatment methods are presented to improve the efficiency of the QWs. Furthermore, a design for electrically driven LED device with SP compatibility is proposed, and requirements on p-type GaN layer thickness and current spreading properties are investigated experimentally.

Resumé

Denne afhandling adresserer manglen på en energieffektiv halvleder lyskilde på den grønne bølgelængde område. Ved at betragte InGaN lysdioder (LED'er) baseret på kvantebrøndsstrukturer (QW), er overflade plasmoner og nano-strukturer blevet undersøgt som mulige løsninger til at forbedre effektiviteten.
Ved at placere et tyndt lag metal eller metal nanopartikler i nær-feltet af QW, er det muligt at forbedre den interne kvanteeffektivitet (IQE) gennem Purcell faktoren. Den generelle opfattelse vedr. koblingen mellem QW og overflade plasmoner (SP) har været, at resonansen for metal nanopartikler skal overlappe med emissionsbølgelængden for at opnå en forøgelse af IQE. Dette kriterie er blevet analyseret, og på baggrund af de eksperimentelle fund har forholdet vist sig at være mere kompliceret. Betingelser som skal opfyldes for at undgå en forringelse af lysudsendelsen er blevet fremlagt.
Koblingen mellem SP-QW vil ikke nødvendigvis medføre en forstærkning af lysudsendelsen. Resultaterne i dette projekt har vist at nanopartiklernes spredning- og absorptionstværsnit har en vigtig rolle i at afgøre hvorvidt emissionen vil blive forstærket eller forringet. Ved at anvende disse principper, er et nyt design præsenteret til at forbedre lysekstraktionen vha. nano-strukturering, og forbedre IQE gennem SP-QW kobling.
Skade påført halvlederen og QW af tør-æts processen er også blevet adresseret. Forskellige behandlingsmetoder er blevet præsenteret som kan forbedre effektiviteten af QW lysudsendelsen efter en tør-æts.
Desuden er der fremlagt en design for elektrisk drevne LED enheder som er kompatible med metal nanopartikler for SP-QW kobling. Krav til tykkelsen af p-doteret GaN lag og egenskaberne af strøm spredningen er blevet eksperimentelt undersøgt.

Ph.D. Publications

Articles in international peer-reviewed journals:

1. **A. Fadil**, Y. Ou, T. Zhan, K. Wu, D. Suyatin, W. Lu, P. M. Petersen, Z. Liu, and H. Ou, "Fabrication and improvement of nanopillar InGaN/GaN light-emitting diodes using nanosphere lithography," *Journal of Nanophotonics* **9**, 093062, p. 1-9 (2015).
2. D. Iida, **A. Fadil**, Y. Chen, Y. Ou, O. Kopylov, M. Iwaya, T. Takeuchi, S. Kamiyama, I. Akasaki, and H. Ou, "Internal quantum efficiency enhancement of GaInN/GaN quantum-well structures using Ag nanoparticles," *AIP Advances* **5**, 097169, p. 1-9 (2015).
3. **A. Fadil**, D. Iida, Y. Chen, J. Ma, Y. Ou, P. M. Petersen, and H. Ou, "Surface plasmon coupling dynamics in InGaN/GaN quantum-well structures and radiative efficiency improvement," *Scientific Reports* **4**, p. 1-7 (2014).

Contributions to international peer-reviewed conferences:

1. **A. Fadil**, D. Iida, Y. Ou, P. M. Petersen, H. Ou, "Dielectric coating and surface plasmon enhancement of multi-color quantum-well structures," *European-Asian workshop on Light-Emitting Diodes*, 2015, Lyngby, Denmark.
2. **A. Fadil**, Y. Ou, D. Iida, H. Ou, "Metal nanoparticles and patterned dielectric on InGaN/GaN LEDs: Combining plasmonic and light extraction enhancement," *International Conference on Light-Emitting Devices and Their Industrial Applications*, 2015, Pacifico Yokohama, Japan.
3. Y. Ou, K. Wu, D. Iida, **A. Fadil**, H. Ou, "Luminescence enhancement of green InGaN/GaN nanopillar LEDs," *International Conference on Light-Emitting Devices and Their Industrial Applications*, 2015, Pacifico Yokohama, Japan.

4. W. Lu, Y. Ou, V. Jokubavicius, **A. Fadil**, M. Syväjärvi, P. M. Petersen, H. Ou, "Wavelength-conversion efficiency enhancement in nano-textured fluorescent 6H-SiC passivated by atomic layer deposited titanium oxide," *International Conference on the Physics of Optical Materials and Devices*, 2015, Budva, Montenegro.

5. W. Lu, Y. Ou, V. Jokubavicius, **A. Fadil**, M. Syväjärvi, V. Buschmann, S. Ruttinger, P. M. Petersen, H. Ou, "Photoluminescence enhancement in nano-textured fluorescent SiC passivated by atomic layer deposited Al2O3 films," *International Conference on Silicon Carbide and Related Materials*, 2015, Giardini Naxos, Italy.

6. **A. Fadil**, D. Iida, Y. Ou, H. Ou, "Localized surface plasmon scattering efficiency improvement," *International Conference of Near-field Optics, Nanophotonics and Related Techniques*, 2014, Salt Lake City, US.

7. H. Ou, **A. Fadil**, D. Iida, Y. Chen, M. Iwaya, T. Takeuchi, S. Kamiyama, I. Akasaki, "Plasmon enhanced green GaN light-emitting diodes," *Progress In Electromagnetics Research Symposium*, 2014, Guangzhou, China. [Invited]

8. **A. Fadil**, Y. Ou, X. Zhu, and H. Ou, "Improved light extraction efficiency of InGaN/GaN light-emitting diodes using dielectric coated nanopillars," *Light, Energy and the Environment, Solid-State and Organic Lighting*, 2014, Canberra, Australia.

9. D. Iida, Y. Chen, Y. Ou, A. Fadil, O. Kopylov, M. Iwaya, T. Takeuchi, S. Kamiyama, I. Akasaki, H. Ou, "Enhanced internal quantum efficiency of green emission GaInN/GaN multiple quantum wells by surface plasmon coupling", *JSAP-MRS Joint Symposia*, 2013, Kyoto, Japan.

10. **A. Fadil**, D. Iida, X. Zhu, Y. Ou, Y. Chen, C. Dam-Hansen, P. M. Petersen, and H. Ou, "Resonant Plasmonic Enhancement of InGaN/GaN LED using Periodically Structured Ag Nanodisks," *Asia Communications and Photonics Conference*, 2013, Beijing, China.

11. D. Iida, Y. Chen, Y. Ou, **A. Fadil**, O. Kopylov, M. Iwaya, T. Takeuchi, S. Kamiyama, I. Akasaki, H. Ou, "Characterization of GaInN/GaN quantum wells through surface plasmon coupling", *JSAP Spring Meeting*, 2013, Kanagawa, Japan.

12. N. Kang, **A. Fadil**, M. Pu, H. Ji, H. Hu, E. Palushani, D. Vukovic, J. Seoane, H. Ou, K. Rottwitt, and C. Peucheret, "Experimental Demonstration of Phase Sensitive Parametric Processes in a Nano-Engineered Silicon Waveguide," *Conference on Lasers and Electro-Optics*, 2013, San Jose California, US.

Contents

CHAPTER 1

Introduction

1.1 Motivation

Light-emitting diodes (LEDs) have attracted renewed interest in the past two decades since the appearance of the first efficient blue GaN LED.[1] Compared to the incandescent and fluorescent light sources, LEDs are smaller in size, have a longer lifespan, and higher overall efficiency. Additionally the LED has a better technical functionality for many lighting applications such as image displays, automotive signalling, and traffic lights among others. At the same time, with a proper design, the colour rendering properties can be comparable to that of the incandescent sources, which provides a superior colour rendering over that of fluorescent lamps. One of the major roadblocks for LEDs, however, is the high cost per lumen preventing competitive prices with conventional light sources. Overcoming these challenges requires efficiency improvement and fabrication cost reduction.

The advent of metalorganic vapor-phase epitaxy (MOVPE) growth technology paved the way for rapid development of the AlInGaN semiconductor material system for solid-state lighting. The bandgap of the AlGaN material system allows for UV light emission, while that of InGaN has the potential to cover the entire visible spectrum. Although the InGaN material system covers a broad range of wavelengths, the highest quantum efficiency is nonetheless attained around blue emission wavelengths, and decreases with increasing wavelength. Green, yellow and red emission colours have a significantly lower efficiency in comparison to blue, due to degraded crystal quality from a larger lattice mismatch. There is in fact a lack of efficient solid-state light-emitters at green wavelengths. The AlInGaP material system already provides an efficient platform for orange-red colour LEDs, but unfortunately also suffers with a low efficiency at green-yellow colours.

Employing a single material system to fabricate efficient LEDs with emission colours spanning the entire visible range also has a technological and industrial importance. This is possible with the wide-bandgap InGaN material system. Much effort has therefore been put into improving the InGaN light-emitting efficiency at green colour. Because the limitations are on one of the fundamental properties of the semiconductor, i.e. the internal quantum efficiency (IQE), the main focus for improvement has been on the material growth aspect and the front-end fabrication.

1.2 Thesis structure

This thesis investigates front-end fabrication methods to improve the IQE and light extraction efficiency (LEE) of green InGaN based LEDs. The impact of surface plasmonics on the active light-emitting region is analysed through experimental results and numerical simulations. Various ways of applying surface plasmonic metals to conventional and novel LED designs are also investigated.

Chapter 2 briefly introduces the fundamentals of light-emission from semiconductors and discusses the InGaN material system. The concept of surface plasmonics is also introduced here, as well as how it can improve the carrier recombination rate in the semiconductor active region.

Chapter 3 considers different metallic structures, including thin films and nanoparticles that are used to improve the emission intensity from InGaN light-emitters. Two LED epitaxial structures are considered with different distance between the active region and the semiconductor-air interface. The effect of plasmonic metals in the near-field of the active region is investigated through the photoluminescence (PL). The IQE of the light-emitters is characterized through temperature-dependent measurements, and the improvements due to metallic nanoparticles are analysed.

Chapter 4 investigates how plasmonic nanoparticles can enhance the emission from the light-emitting region, and why they in some cases result in a degradation of light-emission. In this regard, a dielectric intermediate layer is employed between metal and semiconductor to modify the nanoparticle environment, and the impact of this change is analysed. Numerical simulations are hence conducted with metal nanoparticles on different substrates, and the scattering and absorption cross-sections are discussed in connection with the experimental results.

Chapter 5 further expands on the concept of employing a dielectric intermediate layer between plasmonic metals and the semiconductor surface. Two different dielectrics and their passivation capabilities are investigated in relation to the growth defects on the semiconductor surface. Furthermore, nano-patterning is investigated on the thin dielectric layers to improve the LEE, where metal nanoparticles are subsequently applied to provide additional enhancement through the IQE.

Chapter 6 considers a conventional LED epitaxial structure, where nano-patterning is applied through the active region. The result is IQE and LEE improvement through the effects of lattice strain relaxation in the active region. The structure then allows for plasmonic nanoparticles to be deposited in the near-field of the light-emitting region.

Chapter 7 forms the framework for applying plasmonic metals with an electrically driven LED device. Special contact designs and current spreading layers are analysed in relation with epitaxial structures that allows for plasmonic coupling with the active region. Plasmonic nanoparticles are deployed and the optical and electrical properties of the LED devices are investigated.

CHAPTER 2

Nitride-based light-emitting diodes

2.1 Semiconductor light emitters

The phenomenon of electroluminescence was discovered in the early nineteen-hundreds, where certain materials were found to emit light when applying an electrical field. Although not well understood at the time, the first observation of this phenomenon was made in 1907 from a SiC light-emitting diode (LED), which today would be classified as a Schottky diode.[2] Optically active materials based on III-V compound semiconductors emerged in the 1950s and led to the development of III-V arsenide and phosphide LEDs based on binary, ternary and quaternary semiconductor alloys. In late 1980s, metalorganic vapor-phase epitaxy (MOVPE) growth of high quality crystalline GaN on sapphire substrate became a possibility,[3] and soon after successful *p*-type doping and *p*-type conductivity of GaN was realized by Akasaki and co-workers.[1] These developments paved the road for commercialization of high-brightness blue LEDs in 1993.[4]

With the later discovery of electronic levels in atoms and the development of quantum mechanics, a better understanding of light emission from materials could be reached. It was found that the electrons of an atom only can occupy certain discrete energy levels, and jump between these levels by absorption or emission of light. In solid materials with a crystal structure the energy levels of the atoms are modified due to the interactions between the atoms, and consequently bands of energy levels are formed, available for the electrons to occupy. The electrons in the so-called conduction-band energy level are not bound to the atoms and are able to move freely through the crystal lattice, while electrons in the valence-band are bound to their atoms.

Semiconductors are materials in between metals and insulators, and in general have poor conducting properties at room temperature. Compared to an insulator, a semiconductor has a smaller bandgap (see Fig. 2.1(a)), and at room temperature some of the electrons are excited into the conduction-band and therefore allow partial conductivity. When an electron is excited, an empty space is left behind which can in turn also move freely through the lattice with neighbouring electrons filling the vacancy. The vacancy, or "hole", can be considered as a positively charged particle. Electron-hole pairs are then said to be generated when an electron is

excited into the conduction-band.

To improve the conductivity of semiconductors, impurities known as dopants are introduced into the crystal lattice. These impurities act as either electron donors or electron acceptors to the lattice leading to n-type and p-type doping, respectively. The Fermi levels of the materials will be shifted as shown in Fig. 2.1(b).[5] Certain semiconductors are unintentionally doped during growth, examples include GaN and InN which are always n-type with carrier concentrations around $\sim 10^{16}$ cm^{-3} and $> 10^{20}$ cm^{-3}, respectively.[6] GaN n-type doping can be achieved using Si,[7] while p-type doping which is more difficult can be achieved using Mg followed by a thermal annealing Mg-activation process.[1,8]

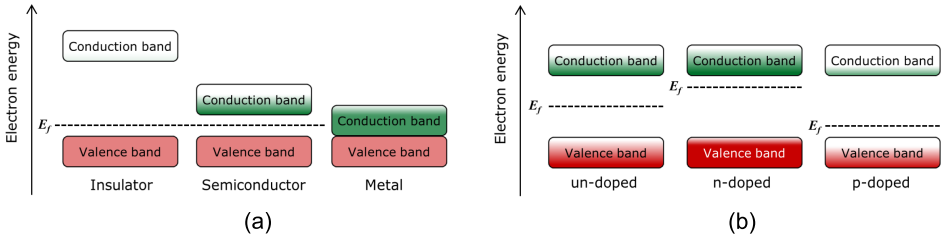

Figure 2.1: (a) Energy band comparisons between insulators, semiconductors and metals. (b) Fermi-levels, E_f, in un-doped, n-type and p-type doped semiconductors.

Electrons in the conduction-band will have a finite life-time, and will eventually decay back into the valence-band by releasing energy, a process known as electron-hole recombination. The recombination process can be categorised as either radiative or non-radiative, where the former means that a photon is emitted with an energy corresponding to the bandgap energy, E_g. The internal quantum efficiency (IQE) is a measure for the probability of radiative recombinations and is defined as

$$\eta_i = \frac{k_{rad}}{k_{rad} + k_{nrad}}, \tag{2.1}$$

where k_{rad} and k_{nrad} are radiative and non-radiative recombinations rates. Examples of non-radiative recombinations include trap-assisted recombinations (Shockley-Read), surface and Auger recombinations.[9]

During the transition from conduction- to valence-band the momentum must be preserved. For direct-bandgap semiconductors the transitions occur between levels of equal momentum vector, $\mathbf{k}$, which is not the case for indirect-bandgap semiconductors. With an indirect-bandgap the conduction-band minimum and valence-band maximum are located at different $\mathbf{k}$-vectors and for the transition to take place (see Fig. 2.2), the electron must undergo a momentum change, e.g. through an interaction with phonons. This process makes indirect-bandgap semiconductors very poor light emitters due to a very slow recombination process. GaN

and InN are examples of direct-bandgap materials while Si is an indirect-bandgap material.

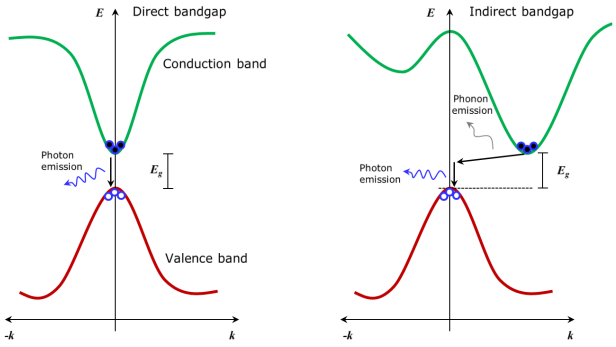

Figure 2.2: Electron-hole recombination processes in direct- and indirect-bandgap semiconductors.

GaN with wurzite crystal structure has a bandgap of about 3.4 eV.[10] The bandgap of InN has been subject to some controversy, where previously[11] it was found to be around 1.9 eV more recent measurement has placed the bandgap around 0.77 eV.[12–15] Fig. 2.3 shows the wide-bandgap capabilities of the III-nitride alloys, according to Ref. [9]. The InGaN material system has therefore the potential to be the basis for UV, visible and IR solid-state LEDs. By forming the ternary alloys of $In_xGa_{1-x}N$, the emission colour can in principle be tuned from about 365 nm to above 1500 nm, covering the entire visible spectrum. Electrically driving GaN/InGaN LED with deep-red emission wavelength at 740 nm has been realized using MOVPE growth.[16]

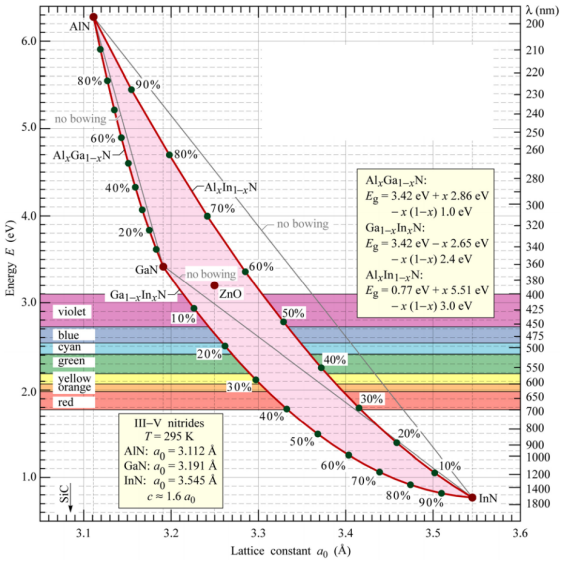

Figure 2.3: Bandgap and lattice constants for AlN, GaN, InN and their alloys. Showing that the ternary alloy combination of InGaN has the potential to cover the entire visible spectral range . From Ref. [9].

2.2 Limitations on efficiency

To have a light emitting device operated by current injection, the charge carriers (electrons and holes) need to be confined to a region where they can recombine and emit light. Heterojunction structures are employed for this purpose, which gives efficient carrier recombination. Typically the heterojunction consists of multiple quantum-wells (MQWs) which help in reducing the amount of carrier overflow[9] and are useful for efficient high-brightness LEDs.[17,18] The active region of blue and green III-nitride LEDs for instance consists of GaN/InGaN barrier-well structures, a typical example of which is shown in Fig. 2.4. The epitaxial layers are usually grown on *c*-plane sapphire substrates, but due to the relatively large lattice mismatch, GaN grown directly on sapphire has a very poor quality.[6] However, it was found by Akasaki and co-workers that good quality crystalline GaN could be grown if a low-temperature AlN buffer layer was grown on sapphire prior to GaN growth.[3] Nakamura showed that by growing a low-temperature GaN buffer layer a better quality of crystalline GaN could be obtained.[19]

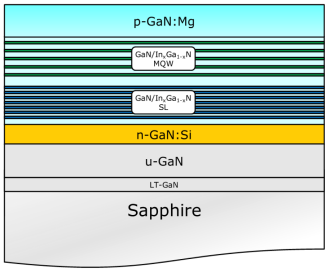

Figure 2.4: Epitaxial structure of an GaN/InGaN MQW LED grown on sapphire substrate.

One problem during III-nitride epitaxial growth is the generation of misfit dislocations at the GaN/InGaN interface.[20] Another problem is threading dislocations (TDs) which are known to degrade device performance by introducing non-radiative decay channels.[21] The super-lattice (SL) structure shown in Fig. 2.4 are grown before the MQWs to prevent TDs from propagating into the MQW active region.[22–24] Due to hole mobility in GaN being much lower than electron mobility,[8,25,26] the carriers from electrical current injection will not recombine at the SL structure and its emission will therefore not be observed except with optical pumping. One difference between the MQW and SL structure is the barrier thickness, with MQW barrier/well thickness being around 15/3 nm and SL barrier/well thickness around 3/3 nm. The InN molar fraction is also lower for the SL structure compared to the MQW to have a better lattice match and thereby achieve a higher quality crystal surface to grow the MQW active region on. As the InN molar fraction is increased the lattice mismatch also increases and it becomes difficult to grow GaN/InGaN MQWs with high InN molar fraction for longer wave-

length emissions, and consequently the IQE of the LED will decrease. This can be explained as being due to an increasing piezoelectric field which induces the quantum-confined Stark effect (QCSE) and thereby limiting the IQE.[27,28]

It is also interesting to note that high efficiency LEDs cannot be obtained using GaN as the active region, however, by incorporating InN molar fractions efficient active regions can be obtained with InGaN.[29] This means that the IQE is improved by adding small amount of In into GaN, however, if the In composition is further increased the IQE starts to degrade due to increasing lattice mismatch and the QCSE. According to the data of Fig. 2.3 the In composition needed for InGaN to achieve blue light emission at 475 nm is about 17 %, and for green emission at 530 nm the composition has to be around 24 %. Currently the external quantum efficiency (EQE) of blue LEDs has reached beyond 80 %.[18,30] The EQE is the probability for a photon being generated and subsequently escaping the LED device package, which by definition will be lower than IQE.
The efficiency of InGaN based LEDs starts to drop at green-yellow wavelengths, and this is in fact a broader problem concerning conventional LEDs known as the "green gap". Recent efficiencies of visible colour LEDs are shown in Fig. 2.5. III-phosphides provide efficient LEDs at the red part of the visible spectrum, but they too suffer the efficiency problem when moving towards the yellow-green colours.[31] This issue has therefore sparked a lot of interest by researchers to improve the efficiency of III-nitride LEDs at green wavelengths and above.

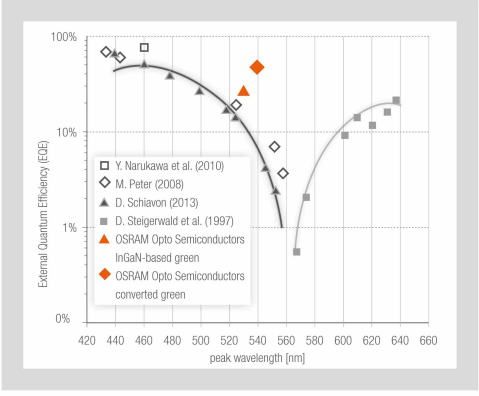

Figure 2.5: Visible colour LED efficiencies. Emission wavelengths below 560 nm are from III-nitrides,[30,32,33] and above 560 nm from III-phosphides.[31] (Source: OSRAM press release 6th June 2014).

2.3 Surface plasmon enhancement of LEDs

One method of improving the low IQE of LEDs involves the application of surface plasmonics on metal-semiconductor interface. This approach can improve the electron-hole recombination rate through the so-called Purcell enhancement effect. The basics of this approach is briefly discussed in this section.

2.3.1 Surface plasmon modes

The interface between a metal and dielectric supports surface waves, where light can be confined to below the diffraction limit. For a planar metal-dielectric interface the dispersion relation (propagation constant) for these so-called surface plasmon polaritons (SPPs) is,[34]

$$\beta = \frac{2\pi}{\lambda_0}\sqrt{\frac{\varepsilon_d\varepsilon_m}{\varepsilon_d+\varepsilon_m}} > k_0\sqrt{\varepsilon_d}, \tag{2.2}$$

where λ_0 is the free-space wavelength, while ε_d and ε_m are the permittivity of the dielectric and metal, respectively. The relation also shows that the SPP propagation constant will always be greater than any value attainable by the dielectric with the permittivity ε_d. This means that an SPP mode in a perfectly planar metal-dielectric interface can never radiate into free-space. This is, however, possible when there are defects on the structure acting as scattering centres. From the expression it is seen that the β-value diverges when $\varepsilon_d + \varepsilon_m = 0$. At this frequency the group velocity approaches zero, which is equivalent of having a non-propagating mode. This is known as a surface plasmon and has an electrostatic character. For a lossy metal, β only reaches a certain maximum, and above the surface plasmon frequency the mode becomes leaky.

The surface plasmon frequency is dependent on the specific metal. For GaN/Ag interface, this frequency is $\hbar\omega_{sp} = 2.92$ eV (about 425 nm). In comparison the frequency for Au and Al is about 2.2 eV (560 nm) and 5 eV (250 nm), respectively.[35,36] Thus for wavelengths below 550 nm the use of Au to excite surface plasmons is not beneficial. Similarly for Al, as the resonance in this case is too far into the ultraviolet regime, and this metal is therefore not very useful at blue and green wavelengths.

Another type of surface excitation is the localized surface plasmon (LSP), which are non-propagating modes. These modes exist in metallic nanostructures, and are a result of the resonant oscillations of electrons. In contrast to the SPP, these modes can be directly excited by light. We will loosely use the term surface plasmon (SP) when generally referring to either of the modes. We will in the following consider how energy can be coupled into SPP and LSP modes from a light-emitter.

2.3.2 Coupling with light-emitters

The amplitude of the SPP mode decays exponentially away from the metal surface, and lies in the near-field of the surface. Hence there is a penetration depth of the surface mode into the semiconductor (and to a lesser degree into the metal). This penetration length into the semiconductor is estimated by,[34]

$$d_z = \frac{\lambda_0}{2\pi}\sqrt{\frac{\varepsilon_d + \varepsilon_m}{-\varepsilon_d^2}}. \tag{2.3}$$

This means that in order to achieve a near-field coupling to the SPP mode, a source has to be at a length within this order of magnitude away from the metal surface.

In Section 2.1 it was seen how an electron-hole pair (exciton) can recombine either radiatively or non-radiatively. If this exciton is within the near-field region of an SPP/LSP mode from a metal surface, the energy of the exciton can be directly coupled into the SPP/LSP mode. This coupling will be a non-radiative excitonic decay. The rate can be estimated from Fermi's golden rule as,[37]

$$k_{SP}(\nu) = \frac{2\pi}{\hbar}\left\langle \mathbf{d}\cdot\mathbf{E}\right\rangle^2 \rho(h\nu), \tag{2.4}$$

where $\rho(h\nu)$ is the SPP/LSP density of states (DOS), $\mathbf{d}$ the exciton dipole moment and $\mathbf{E}$ is the plasmon electric field. The plasmon DOS is calculated as in solid-state physics,

$$\rho(h\nu) = \frac{L^2}{4\pi}\frac{\mathrm{d}(\beta^2)}{\mathrm{d}(h\nu)}, \tag{2.5}$$

where L^2 is the in-plane quantization area. The interesting point to denote here is the slope of the dispersion curve which the DOS is proportional to. From Eq. (2.2) it was seen how the propagation constant would rapidly increase near the surface plasmon frequency, ω_{SP}, implying a very large slope. This in turn means that the plasmon DOS is very high near this resonance, which in turn means a large decay-rate. It has been experimentally demonstrated that the decay-rate into plasmonic modes can be much larger than the rate into other non-radiative channels.[37–39]

Denoting the decay-rate into the SP mode (either SPP or LSP) by k_{SP}, the IQE given in Eq. (2.1) will be modified to

$$\eta_i' = \frac{k_{rad} + \eta_r k_{SP}}{k_{rad} + k_{nrad} + k_{SP}}, \tag{2.6}$$

where η_r is the efficiency of coupling between SPP/LSP and free-space radiation modes.

CHAPTER 3

Surface plasmon coupling with InGaN quantum-wells

To improve light-emitting diode (LED) efficiency using surface plasmon (SP) coupling, the conventional *pn*-junction LED epi-structure has to be modified. The distance between the plasmonic metals and the active light-emitting region has to be within certain bounds to achieve efficient enhancements. In this chapter we consider two fundamental types of epi-structures, a conventional LED structure and a thin *p*-GaN LED structure, and investigate different front-end fabrication designs for achieving SP coupling.

3.1 Conventional thick *p*-GaN LED

For an efficient *pn*-junction LED the required thicknesses of the *p*- and *n*-doped layers have to be larger than the depletion widths in the respective layers to avoid complete depletion by the build-in electric-field.[9] A conservative estimate of the depletion region thickness in *p*-GaN has been given by Kwon *et al.*[40] to be around 76 nm, and by Zhang *et al.*[41] to around 65 nm, however, *p*-GaN is expected to have a smaller depletion width which we later return to.[42] Commercial blue and green LEDs employ a *p*-GaN thickness of about 150 nm, which is needed for efficient current spreading and reduced parasitic series resistance. For SP applications this presents an obstacle for SP-mode coupling with the quantum-wells (QWs), which constitutes the active region of conventional LEDs, as the distance is much larger than the spatial extent of the SP-mode. Without any modifications, SP-metals on the *p*-GaN surface would only interact with the emitted light from the QWs, but not the stored energy in the electron-hole pairs before recombination.

We will in this section consider conventional LED epi-structures and employ nano-fabrication techniques to deposit SP-metal in the near-field of the multiple quantum-well (MQW) active region, and benchmark the results with that of having SP-metal on the unprocessed epi-structure *p*-GaN surface.

3.1.1 SP-LED designs

One possibility of having SP-metals closer to the active region is to partially etch the *p*-GaN, and deposit the metal in the etched region as shown in Fig. 3.1(a). Nanohole photonic crystral (PhC) structure in *p*-GaN was investigated by Lu *et al.*[43] using Ag as SP-metal in the nanoholes with an 80 % enhancement of photoluminescence (PL) at 507 nm emission wavelength due to localized surface plasmon (LSP)-QW coupling, although the total enhancement was more than a factor of 2. Recently, Jiang *et al.* also investigated LSP-QW coupling using Ag nanoparticles (NPs) embedded in nanoholes, showing that under given circumstances such a design can also suppress the PL intensity,[44] hence the dimensions of the pattern and the Ag NPs must be designed with care. More advanced patterns on *p*-GaN have been investigated by Zhang *et al.*[45] using multilayer thin film coating on nano-patterned *p*-GaN surface, where the multilayer consist of dielectric-metal-dielectric and the *p*-GaN pattern works to reduce the distance between metal and the QWs. PL enhancement of more than a factor of 4 was obtained due to the patterning while including Ag thin film in the multilayer design further added an enhancement by roughly a factor of 2.6, resulting in a total PL enhancement by a factor of 11.

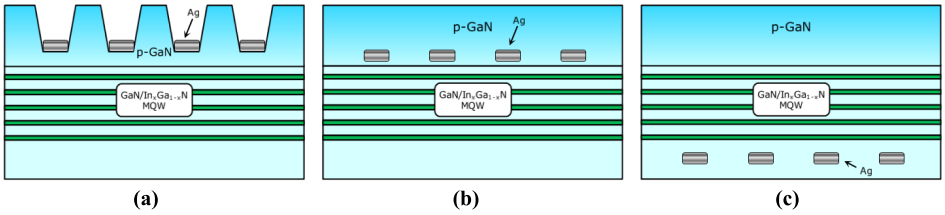

Figure 3.1: Designs for depositing SP-metal closer to the MQWs while maintaining a thick *p*-GaN layer: **(a)** Partially etching the *p*-GaN and depositing metal in the holes/trenches. **(b)** Interrupting the growth process and depositing metal before the completion of the *p*-GaN layer. **(c)** Depositing metal before the MQWs growth and subsequently completing the epitaxial growth.

Other approaches of reducing the distance between SP-metals while maintaining a thick *p*-GaN layer involves an interruption of the epitaxial growth process, where metals can be deposited either after or before the MQW growth as shown in Fig. 3.1(b) and (c), respectively. Cho *et al.*[46] demonstrated this concept by forming Ag NPs on a 30 nm thick *p*-GaN before completing the growth to a 150 nm *p*-GaN, and an integrated PL enhancement (IPLE) by a factor of 2.86 was obtained around 448 nm blue emission. Additionally, they also fabricated electrically driven device, although it only showed a 38 % of optical output power (EL) enhancement at 20 mA driving current. The same group had later improved the EL enhancement to 72 % using SiO_2 nano-disks on top of Ag NPs compared to a 49 %

enhancement without SiO_2.[47] Earlier, Kwon *et al.*[40] had realized the design shown in Fig. 3.1(c) by growing the active MQW region on top of a surface coated by Ag NPs with a resulting EL enhancement of 32 % at blue emission wavelength. Jang *et al.*[48] had taken this step even further by depositing Ag NPs on nano-patterned *n*-GaN surface and subsequently growing the active region, with an achieved EL enhancement factor at 20 mA of about 2.4. The advantage of this approach over the *p*-GaN etch is absence of a dry-etching process to form nano-patterns which has a side-effect of damaging the MQW and degrading the electrical and optical performance of the LED.[49,50] However, the disadvantage with the methods involving an interruption of the epitaxial growth, is the chamber contamination from the SP-metals.

3.1.2 Nanohole array in *p*-GaN

We investigated the design of Fig. 3.1(a) using an LED epi-structure with a 130 nm thick *p*-GaN. As SP-metal we chose to work with Ag due to its promising enhancement potential at green wavelengths. For the process we used nanoimprint lithography (NIL) to form nanohole patterns, where the stamp had pillars with 200 nm diameter and 460 nm period. An overview of the process flow is shown in Fig. 3.2, where the first step was to spin-coat nanoimprint resist followed by hard-baking and then applying the stamp with 3 MPa pressure at 155 °C. To remove the residual resist layer, O_2 plasma was applied. The *p*-GaN was etched using inductively-coupled plasma (ICP) reactive-ion etching (RIE) with Cl_2/Ar plasma chemistry and 60/20 W coil/platen RF power. After the ICP dry-etching, Ag was deposited and a lift-off was performed to reach the final structure shown in Fig. 3.2.

The lift-off process was not without difficulties due to resist attachment to the *p*-GaN surface. Resist removal and lift-off was performed by immersing the sample in a decahydronaphthalene (decalin) solution at 140 °C, i.e. above the glass transition temperature of the resist. One problem was the residual resist layer in certain parts of the surface as shown in Fig. 3.3. To mitigate this problem we prolonged the lift-off duration and increased the solvent temperature to 155 °C, which helped in removing the residual resist layer, although traces of resist could still be observed as seen on the *p*-GaN surface. The remaining traces could only be removed by O_2 plasma cleaning, but this option was excluded since it would also expose the Ag to the plasma.

After the lift-off, the Ag NPs formed in the holes did not have a uniform shape. This is illustrated on a flat *p*-GaN surface as shown in Fig. 3.4(a). A 15 min thermal annealing process at 200 °C did improve the shapes of the NPs, though slightly degrading the periodicity (Fig. 3.4(b)).

Considering that the *p*-GaN cannot be cleaned by O_2 plasma after the lift-off process, an alternative process is desired, where the surface can be cleaned without exposing the Ag NPs, and to this end we consider a maskless deposition technique.

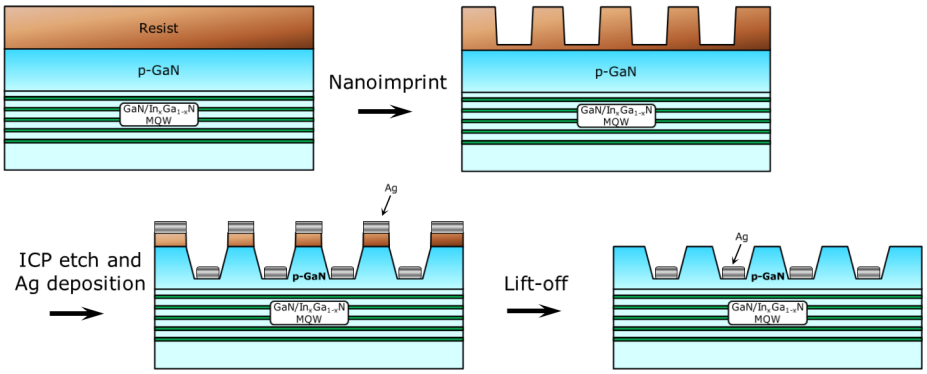

Figure 3.2: Process flow using using NIL to form nano-pattern on p-GaN and depositing Ag in the near-field of the QWs.

In this process, the resist was removed using decalin after the ICP etching of p-GaN. Since no Ag was deposited at this point, an O_2 plasma cleaning could be performed to completely remove the residual resist layer. Since the surface can be oxidized, hydrofluoric acid (HF) cleaning step can be applied at this point if device fabrication is desired later on. On the patterned p-GaN, a 30 nm Ag thin film (TF) was then deposited. A thermal annealing step at this stage could realize a diffusion of Ag into the holes with the right annealing condition and Ag TF thickness. If the Ag thickness is too thin particle-sizes will be too small and some will not be able to diffuse into the holes, and if too thick the holes will be filled leaving some of the particles outside the holes (similar to that shown in Fig. 3.5(a)). The annealing condition was also important, where annealing in vacuum resulted in a better particle diffusion compared N_2 ambient which left particles on the top surface as shown in Fig. 3.5(a).

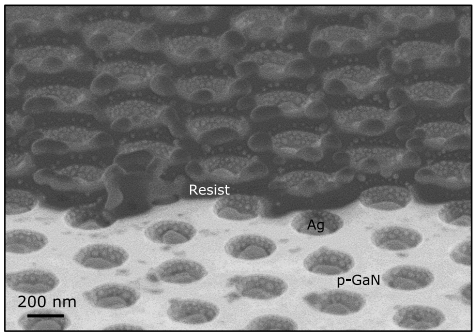

Figure 3.3: Deposition of 30 nm Ag followed by lift-off using decalin. The dark regions are the surface of residual resist layer due to unsuccessful lift-off.

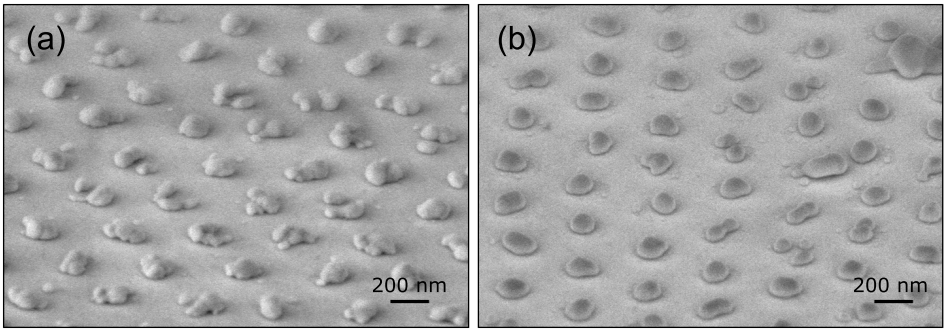

Figure 3.4: **(a)** Bird-eye view of the NPs formed after lift-off and **(b)** the effect of the annealing after lift-off, shown on a flat *p*-GaN surface.

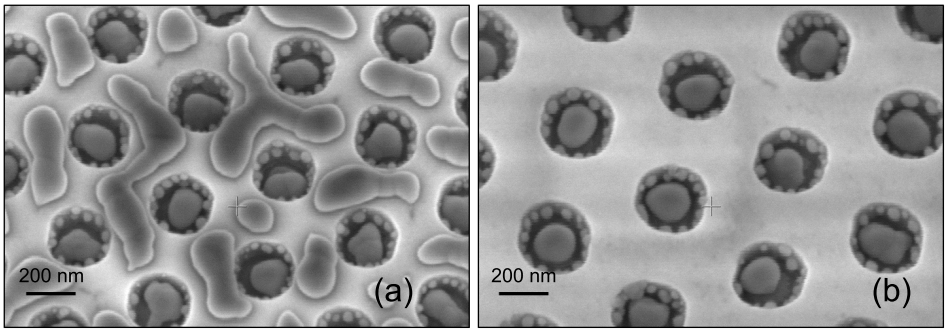

Figure 3.5: **(a)** Formation of Ag NPs on patterned *p*-GaN after annealing a 30 nm Ag TF at 350 °C in N_2 ambient and **(b)** vacuum.

3.1.2.1 Characterizations

In the following we will analyse the effectiveness of SP coupling with QWs and how it compares with simply having an AgTF reflector. We also consider how the distance between Ag NPs and QWs affects the coupling. To this purpose we fabricated four different samples from the same epitaxial wafer (Fig. 3.6), where sample A and D consist of a 150 nm Ag TF coated on the as-grown and 100 nm etched structure, respectively. Sample B and C have nanohole depths of 50 nm and 100 nm, respectively, with a 30 nm Ag deposition followed by lift-off. The purpose of sample A is to estimate the maximum enhancement from a total reflection when excitation and detection is done from the sapphire-side. Sample B and C have different separations between Ag NPs and QWs to examine if a shorter distance results in a larger enhancement. Whether the reflector properties can be combined with SP coupling effects is investigated using sample D.

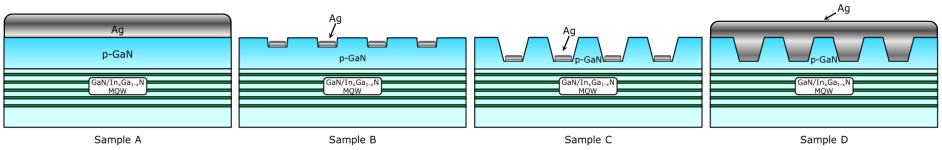

Figure 3.6: Different patterns investigated, where sample A consists of the as-grown sample with 150 nm Ag TF, sample B has 50 nm etched *p*-GaN with Ag NPs, sample C has 100 nm etched *p*-GaN with Ag NPs, and sample D have 100 nm etched *p*-GaN with 150 nm Ag TF.

PL measurements are conducted using a 405 nm excitation laser, with excitation and detection from the polished sapphire-side of the samples, and the spectra are recorded using an Instrument System spectrometer. Normalization of the PL spectra is done for each sample to a given reference denoted "pre-Ag ref.", which is a sample with similar nano-structure pattern without Ag, i.e the reference for sample A is the as-grown structure, while the reference for C and D is the 100 nm etched structure. The PL spectra of samples A-D are shown in Fig. 3.7(a). The peak intensity of sample A is increased by almost a factor of 3 compared to the as-grown sample, though the IPLE factor is about 2.51. The results of 50 and 100 nm nanoholes (NH) with embedded Ag NPs appear opposite of each other with one giving enhancement and the other suppression of PL, respectively. Sample D has a slightly higher enhancement than B (integrated enhancement of 1.85 and 1.57, respectively).

The results of sample B and C are contrary to expectations, since the NPs in C are closer to the QWs than in B and the SP-QW coupling should be stronger. The observed PL suppression in C can hardly be attributed to anything besides the presence of Ag, meaning that effects such as ICP induced damage in the active region, which is higher in the case of C, can be excluded. One possible reason for this behaviour could be the creation of surface states from the metals in the vicinity of the QWs which would degrade the PL intensity due to non-radiative recombinations. This would require a surface passivation step before Ag deposition, by for instance dielectric coating although the process would be more complicated. Another explanation could be that the radiative properties of the Ag NPs and the SP-mode is different between the 50 and 100 nm etched structure, to such a degree that one configuration gives rise to enhancement while the other to suppression due to increased metal dissipation as discussed by Jiang *et al.*[44] The suppression is not seen in the case of sample D which has a similar etch structure, but the enhancement is significantly less than that of sample A, indicating that the coating does not function as a simple reflector. If surface states are inducing non-radiative decay channels, they would also have an effect on the structure of sample D, implying a degraded PL intensity.

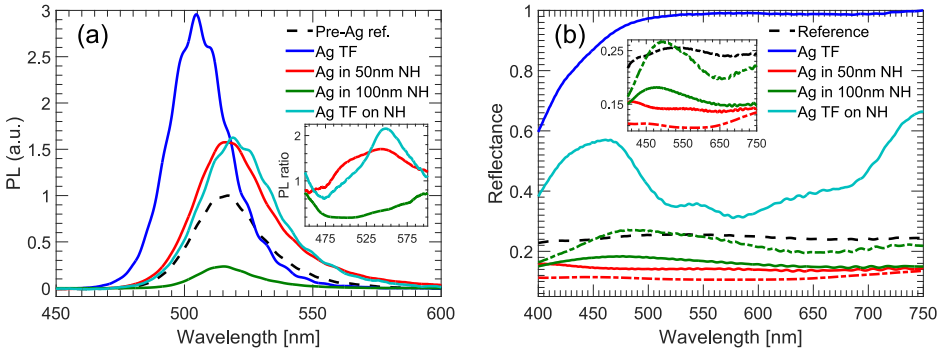

Figure 3.7: **(a)** PL spectra of samples A-D, where normalization is done relative to the peak intensity of each samples uncoated counterpart. Inset shows the PL ratios relative to pre-Ag reference. **(b)** Reflectance spectra of samples A-D (solid curves) compared to their uncoated counterparts (dashed curves of corresponding colour). The inset is a zoomed view of sample B and C reflectance. Corresponding spectra without Ag are also shown (dashed lines).

To better understand the properties of included Ag TF and NPs on the samples, reflectance spectra are measured for all the samples using a white-light source with near normal incidence from the sapphire-side. The spectra are shown in Fig. 3.7(b), where sample A shows 98 % reflectance at the emission wavelength (517 nm), which is an increase by a factor of 3.8 compared to the as-grown sample. The decrease in reflectance below 500 nm is due to absorption from the SL and MQW structure. Considering sample B, the reflectance has increased from 11 % to 14 % due to Ag NP coating, while for sample C the reflectance is decreased from 26 % to 18 %. As a comparison the as-grown sample reflectance at the emission wavelength is 25 %. These values could explain why PL of sample B is enhanced while that of C is suppressed. A degraded reflectance indicates an increased absorption due to Ag NPs which in turn degrades the emission from the QWs. The increased reflectance of sample B alludes to a better scattering from the NPs. The transmittance of sample B (not shown), is also larger than that of sample C, which at the emission wavelength is 58 % for B and 47 % for C, which further supports the notion that the increased reflectance of B is due to better scattering from the NPs in all directions.

Sample D reflectance shows a rather distinctive feature with three reflectance dips at 525, 577 and 683 nm, and a local maxima at 547 nm. The local reflectance maxima coincides with the PL ratio peak at the same position as shown in the inset of Fig. 3.7(a). The reflectance is, however, largely suppressed compared to the TF reflector case of sample A. It should also be noted that transmittance and reflectance spectra are measured on samples with an active region, so the

observed features are not exclusively related to the Ag nano-structures, but rather the combined effect of active region and nano-structures. As such it is not straight forward to relate the PL ratios and the transmittance/reflectance spectra.

The design of sample C was repeated using the maskless deposition process described earlier. The PL results are shown in Fig. 3.8(a), where an improvement is observed by using the maskless process, though the PL is still degraded due to the presence of Ag NPs. The transmittance spectrum now shows a noticeable dip around 690 nm as seen from Fig. 3.8(b), and its level is also significantly lower compared to the lift-off process case.

We attribute the dip to dipolar resonances of Ag NPs. The difference between the lift-off and maskless deposition method is that the latter allows for a larger volume of Ag to remain on the sample as opposed to a lift-off which removes a certain fraction of the Ag, a larger extinction is therefore expected, which is observed through the reduced transmittance. Considering the reflectance, the value has increased from 18 to 29 % at emission wavelength, indicating a larger scattering from the NPs which can explain the improved PL due to the maskless method.

One possibility for PL suppression can be related to the formation of small sized Ag NPs (around 10-50 nm in size) which is visible in Fig. 3.5 inside the nanoholes. As shall be discussed in much more details later on, small sized NPs significantly suppresses the PL due to their large absorption, and their LSP-mode spatial-extent is smaller than the larger ones. These NPs are closer to the active region in a 100 nm etched hole compared to 50 nm, so this can explain why sample C is experiencing PL suppression while B is not.

To further support the claim that small nanoparticles are degrading the PL in 100 nm etch sample, we investigate another sample with a 100 nm p-GaN etch,

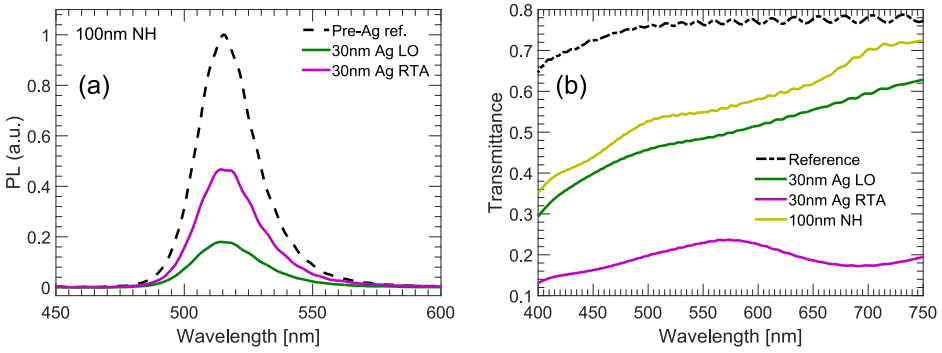

Figure 3.8: **(a)** The PL spectra of the 100 nm etched sample with Ag NPs formed using a lift-off process (Ag LO) and the maskless deposition approach with thermal annealing (Ag RTA), and **(b)** their transmittance spectra, where reference here corresponds to as-grown sample transmittance.

but in this case the holes are on the micro-scale. The fabrication process is done using photolithography with a square array to form holes with 6 μm pitch and 3.8 μm diameter. By a lift-off process, 30 nm Ag TF is deposited inside the holes. As opposed to the sample with 100 nm nanoholes (n-hole), this sample (μ-hole) shows an enhanced PL intensity as shown in Fig. 3.9, with an IPLE factor of 2.6. This is similar to the case with Ag TF covering the 100 nm etched nanoholes which improved the PL instead of suppressing it. In both of these cases, small Ag NPs are not present in the near-field of the QWs.

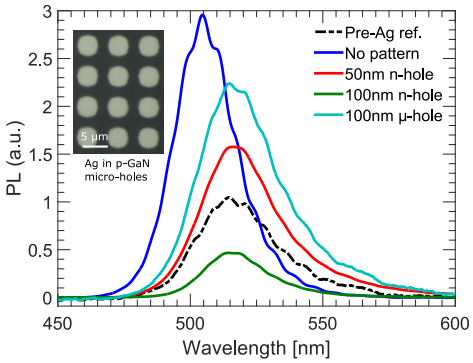

Figure 3.9: The result of Ag coating on samples with various *p*-GaN pattern, comparing between 150 nm Ag TF on as-grown sample (no pattern) as well as nano- and micro-hole pattern of given depths.

3.1.3 Conclusions

We have been able to demonstrate PL intensity enhancement of green LEDs using Ag as SP-metal and as nanoparticles and thin films. However, the purpose of fabricating nanoholes with two different depths was to validate a possible SP-QW coupling through the different enhancement strengths. A stronger enhancement was expected with Ag NPs being closer to the active region. But the results were opposite to these expectations, where the deep etched sample showed a degraded PL while the shallow etched showed enhanced PL due to Ag NPs. Combing the grating structure with a top reflector likewise did not show an improved performance compared to a bare reflector coating using Ag TF.

Care should be taken regarding surface passivation schemes to avoid introducing non-radiative surface states from having metallic nanoparticles in the near-field of the active region, and further investigations are needed.

3.2 SPP coupling in thin *p*-GaN LEDs

The depletion width in *p*-GaN has been estimated[40,41] to be around 70 nm based on a hole concentration of 10^{17} cm^{-3}. However, studies have shown that it is the density of uncompensated Mg acceptors rather than the hole concentration that determines the depletion layer width, and its density is two orders of magnitude larger than the hole density.[51,52] The depletion width is therefore expected to be an order of magnitude lower than estimated.[42] This is a useful property for InGaN based LEDs if surface plasmonics have to be incorporated into the design. Having a *p*-GaN thickness around 30-70 nm can enable the whole or part of the MQW active region to couple with SP-modes of metals on the *p*-GaN surface.

We consider epi-structures where the distance between the GaN-air interface and the top-most QW is 30 nm, and coat the surface with thin films of three different SP-metal to investigate enhancements from surface plasmon polariton (SPP)-QW coupling. The effects will be isolated from the increased reflectance at the GaN-metal interface by inserting a thick dielectric layer between the GaN and the SP-metal.

3.2.1 Recent developments

Coupling between Ag SPP mode and a single InGaN QW located only 12 nm beneath the metal film was demonstrated by Gontijo *et al.*,[37] where a Purcell enhancement of the decay rate was observed. Due to their above-90 % IQE, the Ag TF layer had resulted in a PL suppression. It was later shown through time-resolved PL measurements,[38] that an estimated Purcell enhancement factor of 92 could be obtained using this configuration. It was therefore established that the energy stored by electron-hole pairs could be transferred through a non-radiative decay process (coupling) to SPP modes of a metal in the near-field zone. The non-radiative decay into SPP modes is expected to be very fast due to the large density of states (DOS) of surface plasmons.[37] The DOS accounts for the available number of modes per frequency. If one could somehow design the metal film such that it would re-emit the stored energy as photons, a secondary radiative decay channel would be introduced into the system. For a perfectly flat interface between metal and dielectric, SPP modes cannot couple with free-space radiation, but will be confined to the interface and dissipate. Nonetheless, real practical devices have a finite surface roughness, which can act as scattering centres for SPP mode and enable coupling into free-space radiation. Strong PL intensity enhancement was obtained from an InGaN QW light-emitter by Okamoto *et al.*[39,53] using 50 nm Ag TF at a 10 nm distance from the QW. It was argued that the enhancement was due to the fast process of SPP-QW coupling and the subsequent re-emission of light from the SPP mode, and that the PL increase due to pump-light reflection at the metallic reflector would be small in comparison. The IQE of their QW emitter was 6 %, and they showed that the Ag TF coating increased the IQE to 41 %. The relation between emitter IQE and enhancement capabilities of surface

plasmons will be discussed in the following section. Single QW LED enhanced by plasmonic metals and operated by current injection was demonstrated by Yeh *et al.*,[54] where they had specially designed a current spreading grid to allow for an Ag TF to be deposited between the grids and couple with the QW. With a 70 nm *p*-GaN thickness they obtained up to 50 % EL enhancement using a 50 nm Ag TF on a 10 nm SiN dielectric layer to separate the Ag from the *p*-contact metal.

3.2.2 Metallic thin films for SPP coupling

In the following we will consider LED epi-structures where the distance between the GaN-air interface and the top-most QW is 30 nm. The structure consists of 5 periods of 12 nm/2 nm GaN/InGaN QW active region covered with 5 nm GaN capping layer, a 20 nm *p*-GaN:Mg, and a 5 nm thick p^+-GaN:Mg *p*-contact layer. We will investigate the effects of plasmonic metal coating on *p*-GaN, and separate the effects of SPP coupling and reflection enhancement. Furthermore we test three different metals, including silver, gold and aluminium, which have plasmon energies at about 410, 560 and 250 nm on GaN substrate, respectively.[39] SPP modes are therefore expected to exist above those wavelengths, which also imply that Au should not be able to provide SPP coupling at green wavelengths. Another point to emphasize is the coupling strength variation to the different QWs in the MQW LED, where the top-most QW will experience the strongest coupling.

Metal deposition was achieved by e-beam evaporation, and all metals were deposited with a 50 nm thickness. The PL spectra were measured on each sample before and after metallic coating for optimal evaluation of the SPP effects, and to avoid the intensity and wavelength variations which exist in typical epitaxial wafers. The effects of having Ag, Au and Al coating are shown through the PL spectra in Fig. 3.10(a). We obtain a similar trend as that by Okamoto *et al.* using a single QW structure,[39] where Ag TF gave the strongest PL followed by Al TF coating. The IPLE factor for Ag and Al are 4.0 and 2.6, respectively. With Au coating the PL is degraded. We also measured the reflectance of the samples from the sapphire-side which is shown in Fig. 3.10(b). It is noted that the reflectance levels with Ag and Al coating has increased considerably, though not as much as that obtained for 150 nm coating previously. In the case of Au, the reflectance sharply drops around 500 nm, and at the same time shows a weak transmission window as seen by the inset transmittance spectrum at 512 nm. In comparison, the PL ratio for Au shows a minimum at 512 nm. The absorption cannot be related to the bound SPP modes (with large DOS) of Au, as the wavelength is located below the surface plasmon wavelength of Au ($\approx$ 560 nm). Though it can be related to the quasi-bound leaky SPP modes which exist above the surface plasmon frequency for lossy metals.[34]

To isolate the reflector effects of the metal coating from those of SPP coupling and radiative decay rate improvement, we consider another batch of samples (from

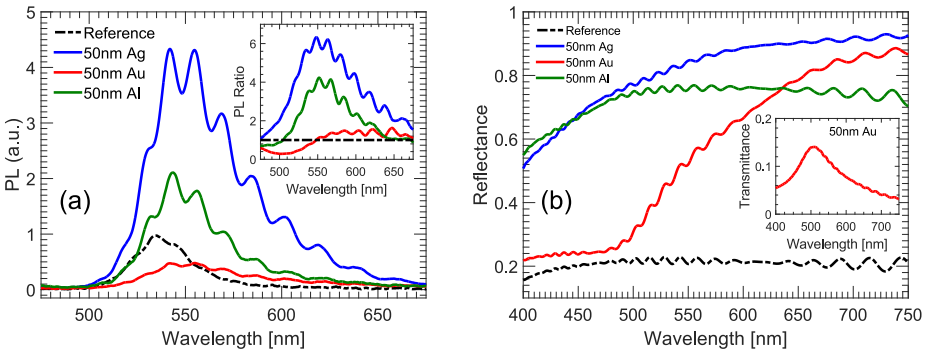

Figure 3.10: **(a)** PL spectra after coating with Ag, Au and Al TF on 30 nm thin *p*-GaN samples. All the spectra are normalized to the peak of the reference. The inset shows the PL ratio. **(b)** Reflectance spectra measured from the sapphire-side of the metal coated samples compared to the uncoated sample (reference). Inset show the peculiar transmittance spectrum of Au coating.

the same wafer) where we increase the distance between the metal and the QWs. This we achieved by introducing a 120 nm thick SiN dielectric intermediate layer between the metal and *p*-GaN. The deposition was done using plasma-enhanced chemical vapour deposition (PECVD). The PL were once again measured before and after metal coating, and the spectra are shown in Fig. 3.11. As before, the strongest enhancement is obtained with Ag TF followed by Al TF coating, with 3.1 and 2.6 of IPLE, respectively. In the case of Au TF coating, however, the PL intensity is not suppressed – rather it is enhanced by a factor of 1.8, which

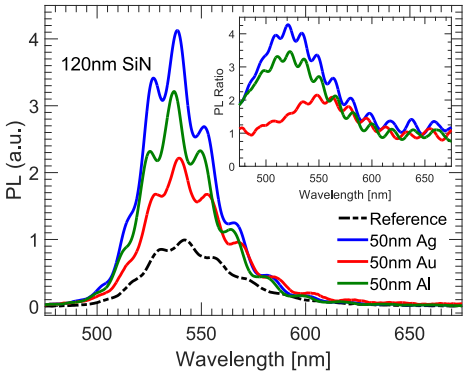

Figure 3.11: PL spectra after introducing a 120 nm SiN dielectric intermediate layer between metal and *p*-GaN. The inset shows the PL ratio.

indicates that the PL suppression could be due to a coupling between the QWs and SPP modes above the surface plasmon frequency. The enhancement from Al TF is almost similar to the previous case without SiN, indicating that it might be the result of having a reflector rather than SPP coupling.

To exclude the effects of reflectance enhancement which is clearly visible from the reflectance spectra, we first determine the reflectance ratios between the metal coated samples and the respective references, $r_{\mathrm{enh}} = R_{\mathrm{Ag}}(\lambda)/R(\lambda)$. Then the PL ratios are divided by r_{enh}. The modified PL ratios are shown in Fig. 3.12. As expected, the enhancements observed when including a 120 nm SiN layer are almost entirely due to reflector properties, as the PL ratio is reduced to around unity when dividing by the reflectance ratio. Without the SiN layer, an enhancement ratio of about 1.5 beyond the reflector properties is observed for Ag TF, but not for the Al TF case. This excess factor of enhancement can be related to SPP-QW coupling with Ag TF.

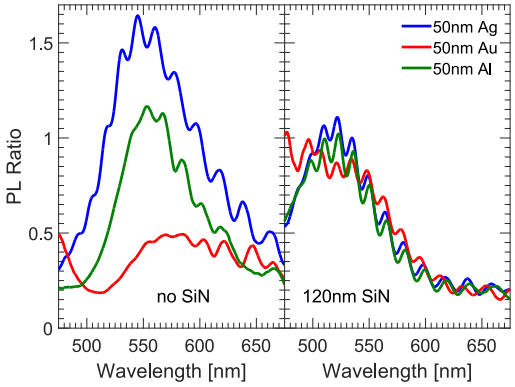

Figure 3.12: Modified PL ratios for metal coating on (left) bare *p*-GaN (no SiN) and (right) on 120 nm SiN on *p*-GaN, excluding reflectance enhancement effects.

3.2.3 Conclusions

Observing a PL enhancement by coating the *p*-GaN surface with a plasmonic metal does not necessarily imply a SPP coupling which improves the decay rate and IQE. Measuring the reflectance spectrum is an important first step to determine how much of the enhancement is due to the metallic reflector coating. We have been able to isolate the effects of SPP enhancement using Ag TF coating, which is estimated to be around a factor of 1.5. Enhancements related to SPP-QW coupling could not be observed from Au or Al TF coatings.

The observed effects are weak compared to what can be expected from SPP coupling.[39,54] Nonetheless, it should be noted that in our structure only the top-most QWs can be strongly enhanced by SPP coupling, hence the effect of enhancing one or two out of five QWs would overall have a less pronounced effect compared to enhancing a structure with a single QW. In other words, if only the top-most QW is enhanced for an MQW structure, it roughly corresponds to enhancing only 20 % of the active region. This also implies that when considering a PL ratio with an MQW structure, the SP features can only be faintly observed.

3.3 LSP coupling using Ag nanoparticles

Using a thin film metal the active QW region can only couple to SPP modes, and although it is possible to modify the SPP properties and tailor the decay-rate-enhancement wavelengths by using multiple dielectric-metal layers,[55,56] there will be no emission from the p-GaN surface. This design is not an obstacle for high power flip-chip LEDs employing light emission from sapphire or n-GaN side, however, the radiative properties of SPP modes, i.e. coupling with free-space radiation, is a limiting factor which will require surface roughness, grating or plasmonic antenna structures for coupling out the light.[34,57] Metallic nanoparticles on the other hand, support non-propagating localized surface plasmon modes which can be excited by an oscillation electromagnetic field with no requirement on phase-matching as needed for SPP modes. This also means that a metallic NP can radiate the stored energy of an LSP mode without phase-matching, though the detrimental aspect for this radiation is the absorption and scattering properties of the NP.

In this section we investigate Ag NPs formed on a thin p-GaN MQW LED similar to that described earlier. The coupling effects between the active region and the NPs will be analysed through PL and IQE measurements, and resonance properties of the NPs are analysed through reflectance and transmittance measurements. We will demonstrate the impact of NP size on the coupling and emission enhancement.

3.3.1 Recent developments

A simple way of obtaining metal NPs is by thermally annealing a thin film metal, which can transform the thin film into islands or clusters of nano-structures depending on the film thickness prior to annealing. This method was applied to InGaN QW emitters by Yeh *et al.*[58,59] where they demonstrated that by using Ag NPs, a better result could be obtained in terms of PL and EL enhancement compared to Ag TF. It was also shown that the efficiency droop in LEDs could be mitigated[60] and that the modulation bandwidth for visible light communication could be improved.[61,62] Decay rates were also shown to be improved by using Ag NPs. The LSP-QW coupling mechanism is expected to be similar to that of SPP-QW coupling, where the exciton energy is transferred to the LSP mode through a non-radiative decay process. This channel has a very fast decay rate compared to other non-radiative channels, and a decay rate enhancement can therefore be observed through time-resolved PL (TRPL) measurements. Transferring the energy into the LSP mode does not ensure a higher internal quantum efficiency (IQE), it is rather determined by the radiative efficiency, η_r, of the LSP mode.[63] The coupling and decay mechanisms are illustrated in Fig. 3.13, where an additional radiative decay channel is introduced by the NP.

Fabricating metal NPs by using a thermal annealing approach does not lead to a uniform particle size, shape or spacing. A distribution and spread in LSP reso-

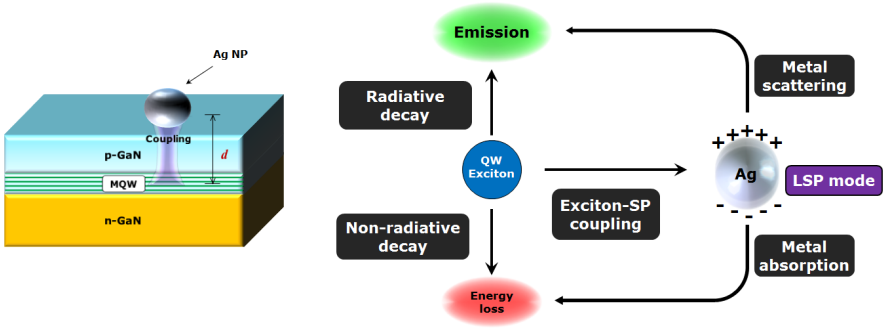

Figure 3.13: The decay channels of an exciton in the near-field of a metallic (Ag) nanoparticle. The LSP mode has two decay channels, with one of them contributing to light emission.

nances will hence be formed in such a system. The size distribution can be varied by modifying the initial metal film thickness, where thicker layers produce larger particles after annealing.[58] Without using expensive fabrication methods such as electron-beam or nanoimprint lithography, synthesized metallic NPs can be used with relatively uniform particle sizes that can be coated on the surface.[64–66] Synthetic metal NPs are commercially available where it is also possible to have dielectric coated metal NPs to prevent oxidation, though the PL and IQE enhancement capabilities so far have been low.[66] Another way to create uniform sized NPs with partial control over the size is by using polymer nanospheres as mask template with metal deposition on top followed by lift-off – a process known as nanosphere lithography (NSL).[67–70] Huang *et al.*[71] employed a type of NSL where Ag NP size could be controlled through the polymer nanosphere size, which is useful for tuning localized surface plasmon resonance (LSPR) wavelength through the particle size.

By controlling the spacing between the NPs in addition to the size, lattice properties, such as coupling, directionality and wavelength selectivity can be exploited. Henson *et al.*[72,73] investigated the LSP coupling using a periodic array of Ag NPs on MQW structure with 5 nm top capping layer to minimize the distance between QWs and Ag. The strong lattice resonances and scattering efficiency are expected to assist the out-coupling of light from the LSP modes. Indeed Henson *et al.* showed that a strong PL enhancement, up to about a factor of 5, could be obtained by carefully tuning lattice parameters such as periodicity and NP size. The best result was obtained with a lattice period matching the emission wavelength in the GaN material, indicating the important role of lattice resonances.

It has also been suggested that metal NPs can improve the light extraction efficiency (LEE) by coupling with light modes that are trapped from total internal reflection (TIR), a so-called LSP-TIR coupling. LEE improvement was demonstrated by Sung *et al.*,[74] where by depositing metal NPs on 60 nm ITO covering

a 140 nm thick p-GaN they could observe a 126 % of EL enhancement. Due to the large distance to the active region the enhancement could not be attributed to LSP-QW coupling, and from angle resolved measurements, reflectance values well below unity was obtained beyond the critical angle.

3.3.2 Fabrication and characterization of Ag NPs

We fabricated Ag NPs based on the self-assembly method by thermally annealing a thin film Ag layer. Various thicknesses of Ag TFs were deposited on top of the p-GaN surface of an MQW LED with 30 nm p-GaN (samples A, B and C), and a barrier/well thickness of 12/2 nm. The samples were annealed at 200 °C for 30 min in N_2 atmosphere. The Ag TFs were transformed into random sized and spaced NPs during thermal annealing process, which is shown in the scanning electron microscope (SEM) images of Fig. 3.14. As the TF thickness increases, the size of Ag NPs also becomes larger, while the density decreases. The NPs show a tendency of becoming more irregular-shaped with increasing size variation as the thickness increases. Average particle sizes are approximately 50 nm, 120 nm and 185 nm for samples A, B and C, respectively.

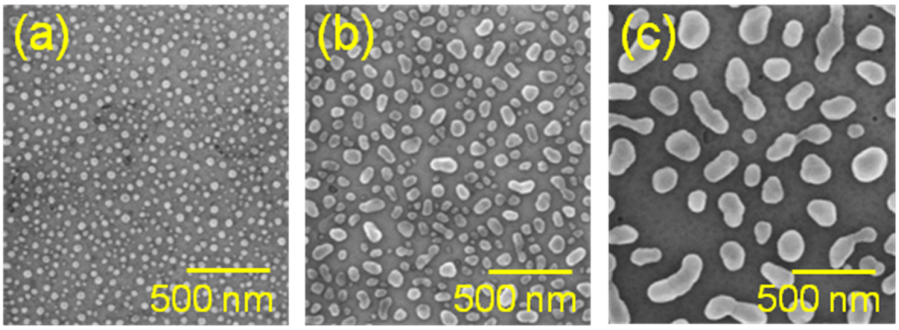

Figure 3.14: Formation of Ag NPs after thermal annealing at 200 °C for 30 min in N_2 atmosphere using **(a)** 4 nm (sample A), **(b)** 9.5 nm (sample B), and **(c)** 17 nm Ag TF (sample C).

To determine resonance properties of the NPs we conducted reflectance and transmittance measurements using a white-light, incident from the polished sapphire-side. The reflectance is an important property to measure in order to determine possible reflectance enhancement effects. The reflectance spectra are shown in Fig. 3.15(a), where none of the Ag NP coated samples show a reflectance higher than the reference. Considering sample A, the dip seen at 482 nm can be attributed to LSPR, while the other at around 390 nm could be due to LED material as it is also present for the as-grown reference. Sample B appears to have a peak, however, this is due to the dip at 390 nm, and another at around 660 nm which can be attributed to dipolar resonances, giving the impression of a peak. Sample C

shows two characteristic dips – at 442 nm and 775 nm. The dip at 442 nm can be related to higher order LSP modes.[72,73]

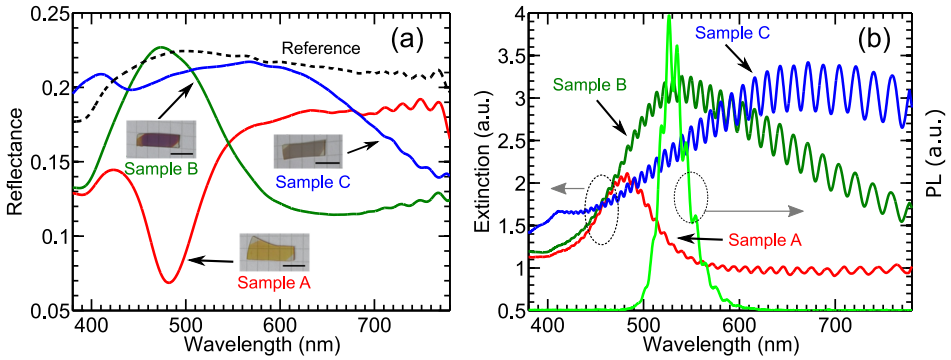

Figure 3.15: **(a)** Reflectance spectra for the samples with Ag NP coating compared with a reference sample without Ag NPs. The inset pictures show the samples with Ag NPs. Scale bars are 1 nm. **(b)** The normalized extinction spectra and the PL spectrum of the reference for comparison.

Also measured are the extinction spectra ($1-Transmittance$), which are shown in Fig. 3.15(b). An interesting feature to note is the blue-shift of the peaks relative to the reflectance dips. The main extinction peaks for samples B and C are located at 540 nm and 672 nm, respectively. This is similar to the known phenomena of energy difference between maximum near-field enhancement and the maximum of the corresponding far-field spectrum, where a red-shift of the near-field quantity is observed relative to the far-field quantity.[75] In our situation the reflectance spectra are giving information about the near-field quantities of the LSP modes, although to be more accurate the absorption spectra ($1 - T - R$) would be quantity to extract this information from. The main absorption peaks for samples A-C are located at 482 nm, 545 nm and 708 nm, respectively, and this is to be compared with the extinction peaks located at 482 nm, 540 nm and 672 nm.

It is seen that the extinction peak red-shifts with increasing average particle size. This is consistent with the behaviour of dipolar resonance which red-shifts with increasing particle size in the dipole approximation.[76] These self-assembled Ag NPs have different sizes and spacing, and this will in principle give rise to an inhomogeneous broadening of the LSPRs from the distribution of the particle sizes, and the result is an increase in the full width at half maximum (FWHM). Sample A has the most regular shaped NPs with a small spread in size distribution, and is in effect showing a resonance peak with the smallest FWHM. Resonance peak of sample C, located at 672 nm, has a large FWHM in contrast, the tail of which is covering the MQW emission spectrum. Sample B LSPR had a better spectral overlap with the MQW emission than the remaining Ag NP structures as shown

in Fig. 3.15(b). It can therefore be expected that LSP coupling with the QWs of sample B can be the most pronounced. The NP details are summarized in Table 3.1.

Table 3.1: The correlation between Ag thickness, the NP size and the density for samples A, B and C as well as LSPR positions.

Sample	Ag TF [nm]	Size [nm]	Density [10^9 cm^{-2}]	LSPR [nm]
A	4	20 – 50	29	482
B	9.5	25 – 120	8.9	540
C	17	55 – 185	1.5	672

3.3.3 IQE enhancement

We investigated PL enhancement of the GaN/InGaN QWs with various Ag NP sizes. For PL measurements the sample excitation and detection were done from the polished sapphire-side, and the spectra measured at room temperature (RT) are shown in Fig. 3.16. It is seen that the PL intensity of sample A has remained nearly unchanged compared to the bare LED emission, while PL enhancements are observed for sample B and C. Increasing the Ag thickness, hence also the average particle size, results in an increase in PL enhancement. The IPLE of samples A-C relative the reference sample are 1.25, 2.59 and 6.02, respectively.

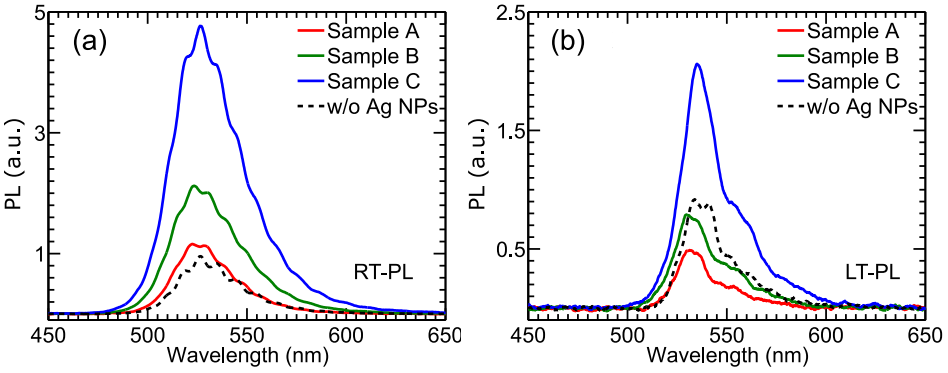

Figure 3.16: **(a)** Room temperature PL sptra of InGaN/GaN MQWs with Ag NPs on top. Excitation power density is 756 W/cm^2, and emission peak is around 530 nm. **(b)** PL spectra measured at 20 K.

Other mechanisms could exist behind the PL enhancement in addition to LSP-QW coupling. One is an enhanced reflection from the top p-GaN surface of either the excitation laser signal, and/or the emission from the QWs, both of which would

give an enhanced signal at the detector. As shown by the reflectance spectra in Fig. 3.15(a) the Ag NPs formed on the p-GaN surface do not result in an increased reflection compared to the as-grown surface at the MQW emission wavelength. At the excitation wavelength the reflection is enhanced by 10 %, which results in an insignificant enhancement factor[73] that is already taken into account in Fig. 3.16.

Under the assumption that non-radiative recombinations are inactivated at cryogenic temperatures, one can retrieve the IQE from the temperature dependence of integrated PL intensity, I.[77] The IQE is defined by normalizing the integrated PL intensity to 1 at 20 K, i.e., assuming the IQE to be 100 %. Thus, the IQE at room temperature will be defined as $IQE = I_{295K}/I_{20K}$. As the temperature increases, PL intensity degrades due to activation of non-radiative recombination processes. The IQE for the 530 nm emission was found to be 19.3 % for the reference sample. The PL spectra at low temperature (LT) are shown in Fig. 3.16(b). It is noticed that the PL of sample A is significantly lower than the reference, while that of sample B is approximately the same. In the opposite end we have sample C which at low temperature shows an IPLE of about 2.33. These results suggest that the observed RT-PL enhancements of sample C are not entirely due to LSP-QW coupling, as no enhancements should be observed at low temperature.[53,63,71] The PL intensity variations at low temperature can be attributed to LEE modification through LSP-TIR coupling.[74,78] Due to the strong absorption of the small NPs in sample A, the NPs are suspected of degrading the PL intensity at low temperature, not through LSP-QW coupling, but by interacting with and absorbing the emitted light. It has been shown experimentally that surface plasmonic coupling with QWs has a similar mechanism as the exciton-phonon coupling of non-radiative decays where the coupling diminishes at low temperatures.[53,79]

We proceed to study the improvement of IQE based on the LT-PL measurements. We analysed the IQE of the LEDs with various Ag NPs by measuring PL intensity versus temperature, as shown in Fig. 3.17(a). Regarding the Ag NP coated samples, the expression for the IQE, η_i', will be modified due to LSP-coupling as given in Eq. (2.6). However, as discussed above, the LSP-QW coupling at low temperature can be neglected and therefore the IQE can still be approximated as 100 % for the Ag NP coated samples. We can then estimate the IQE of samples A-C the same way as the reference, and obtain 26.1 %, 26.4 % and 44.2 %, for samples A, B and C, respectively, with 756 W/cm^2 of excitation power density. Table 3.2 summarizes the IQE enhancement factors.

We note that the IQE of sample A is almost equal to that of sample B, and higher than the reference sample IQE, contrary to what was observed in the PL measurements of Fig. 3.16 where sample B had a considerably higher PL intensity. The integrated PL intensity is proportional to the external quantum efficiency (EQE), and as such it includes the effects of both IQE and LEE, $EQE = IQE \times LEE$. The observed difference between the integrated PL and IQE enhancement factor suggests a modified LEE for samples A-C. The IQE enhancement of sample

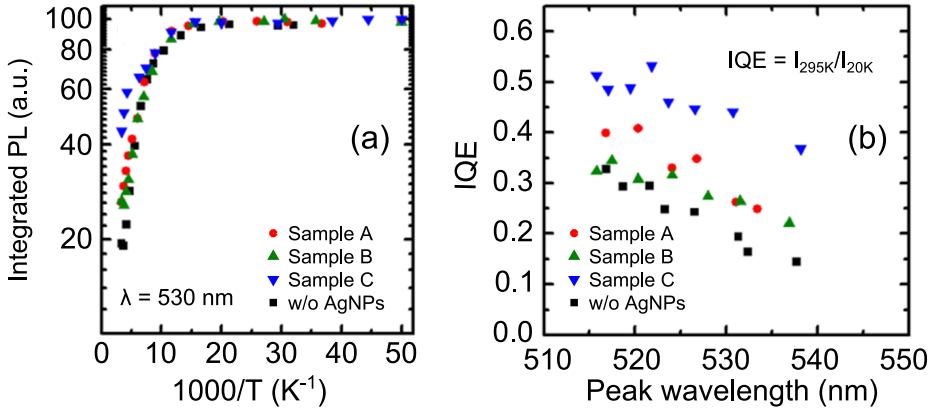

Figure 3.17: **(a)** Temperature dependence of integrated PL for estimating IQE. PL intensity has been normalized to 100 at the 20 K value. **(b)** The IQE as a function of emission peak wavelength at 295 K. Excitation power density is 756 W/cm^2.

A is higher than its IPLE which indicates a degraded LEE. As for samples B and C it is seen that the integrated PL intensity has a higher enhancement than the IQE. Assuming the integrated PL intensity is proportional to the EQE, the LEE enhancement can then be estimated through the ratio between IPLE and IQE enhancement. This follows since the IPLE can be written as

$$\frac{I_{\mathrm{Ag}}}{I_{\mathrm{ref}}} = \frac{LEE_{\mathrm{Ag}}}{LEE_{\mathrm{ref}}} \times \frac{IQE_{\mathrm{Ag}}}{IQE_{\mathrm{ref}}}. \tag{3.1}$$

The LEE ratios for samples A-C are listed in Table 3.2, where sample B and C show an enhancement factor of 1.9 and 2.6, respectively, while sample A shows a reduced LEE based on these estimations. The improved LEE due to Ag NPs is observed from sapphire-side emission, and is expected to be coming from the scattering of Ag NPs acting on the QW emission, and the LSP-TIR coupling. In the following we will direct our attention to the IQE enhancement caused by the Ag NPs.

From the epitaxial growth, the InN molar fraction had a variation across the wafer, with circular contours of equal peak wavelength and intensity. The reference and samples A-C all had equal distribution of peak wavelengths and intensity. By varying the position of the excitation laser spot on the samples, the peak wavelength of the PL spectrum could be varied accordingly. The variation was roughly from 516 to 538 nm. This would enable a measurement of Ag NP enhancement at different peak wavelengths. Using this fact, the IQE was measured at various peak emission wavelengths as shown in Fig. 3.17(b). For the reference sample, the IQE is seen to drop with increasing wavelength, as expected due to increasing indium composition in the sample.

Table 3.2: Summary of enhancement parameters due to Ag NP coating.

Sample	Avg. size [nm]	Integrated PL enhancement[1]	Deduced LEE enhancement	High power IQE enhancement[2]	Low power IQE enhancement[2]
A	50	1.25	0.93	1.35	1.10
B	120	2.59	1.90	1.36	1.71
C	185	6.02	2.63	2.29	8.12

[1] At 295 K, and 756 W/cm^2 excitation power.
[2] High power: 756 W/cm^2, Low power: 1 W/cm^2.

Fig. 3.18(a) shows the IQE enhancement variation with peak wavelength. A general trend for all the samples with Ag NPs is the increase in IQE enhancement factor with increasing peak wavelength. From 516 to 538 nm, the enhancement for sample A and B goes from a factor of 1.2 to 1.5, and 1.0 to 1.5, respectively. While for sample C it increases from 1.5 to 2.6. This is in agreement with the expectation that the lower the as-grown IQE is, the higher the enhancement factor can be due to LSP coupling.[63] The trend is most clear for sample C which has the highest enhancement, as well as an increase with wavelength. A better illustration is given in Fig. 3.18 (b) which shows the enhancement variation with original (i.e. reference sample) IQE.

To understand the observed trends, we consider the IQE enhancement factor, K, for isolated nanoparticles,[63]

$$K = \frac{\eta_i'}{\eta_i} = \frac{1 + F_p \eta_r}{1 + F_p \eta_i}, \tag{3.2}$$

where $F_p = k_{SP}/k_{rad}$ is the Purcell enhancement factor, η_r is the radiative efficiency of the LSP mode and η_i is the original IQE. This relation also implies that the requirement for IQE enhancement, i.e. $K > 1$, is that the LSP mode

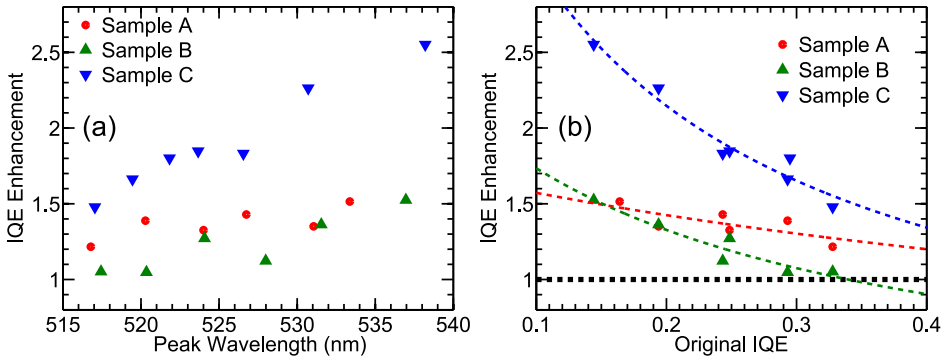

Figure 3.18: **(a)** IQE enhancement factor as a function of peak emission wavelength and **(b)** as a function of the original IQE (i.e. reference sample IQE). Dashed lines are fitting based on Eq. (3.2) .

radiative efficiency has to be larger than the original IQE, $\eta_r > \eta_i$. By using this relation to fit the data in Fig. 3.18 (b) we obtain both the Purcell factor and the radiative efficiency of the Ag NPs. From these measurements, we estimate a Purcell enhancement factor of 7.5 and an LSP radiative efficiency of 58 % for the Ag NPs of sample C. The results are summarized in Table 3.3. The extracted Purcell factors support the observations from the PL enhancements. However, the fitting for sample A is not accurate from these measurements as indicated by the small R^2 fitting parameter, hence it is not possible to make firm conclusions regarding sample A. Following discussions will further support the results of samples B and C.

Table 3.3: Fitting parameters for IQE enhancement variation with original IQE, when considering the data from IQE variation by wavelength, and when considering the total data from IQE variation by wavelength and power density. Fitting quality is given in terms of R^2-value.

	Wavelength variation			Wavelength & power variation		
Sample	η_r	F_p	R^2	η_r	F_p	R^2
A	0.65	1.2	0.56	-	-	-
B	0.34	4.4	0.91	0.38	2.4	0.77
C	0.58	7.5	0.96	0.45	26.5	0.95

3.3.4 Excitation power density dependence

In this section we investigate the excitation power density dependence of IQE, which further supports the conclusion of improved IQE due to plasmonic coupling from temperature dependent PL measurement. In Fig. 3.19(a) we obtain the IQE at various excitation power densities for the emission point with 530 nm peak wavelength at 756 W/cm^2. We first note the increasing IQE of the reference sample with increasing power density. This effect is attributed to coulomb screening of the quantum-confined Stark effect (QCSE) by the increasing carrier density.[80] Fig. 3.19(b) shows the IQE enhancements with varying excitation power density. The trend for sample B and C is a decreasing enhancement with power density, while for sample A the opposite trend is observed, although weak. It is also noticed that the enhancements factors for sample A and B approach each other at high power density.

To understand the decrease in IQE enhancement, we need to keep in mind the increase in original IQE with increasing power density. As seen from Fig. 3.19(b) this effect resulted in a decrease in enhancement. In Fig. 3.20 we have the IQE enhancement factors of Fig. 3.19(b) as a function of the original IQE, as well as the enhancement factors from peak wavelength variation as given in Fig. 3.18(b). The measurements for samples B and C using the two approaches appear to be

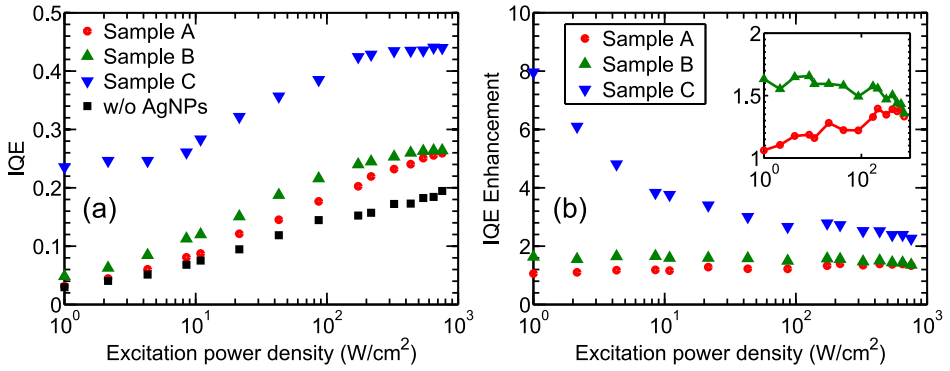

Figure 3.19: **(a)** The measured IQE and **(b)** IQE enhancement factor as a function of excitation power density at 295 K. Inset is the zoom for sample A and B.

consistent. As for sample A, opposite trends are seen between the two measurement techniques. The dashed lines are the result of fitting the total data to Eq. (3.2). This time, however, the calculated Purcell enhancement factor, F_p, for sample C is 26.5, while it is 2.4 for sample B. Results are summarized in Table 3.3. The different Purcell factors obtained when compared to earlier is due to the fact

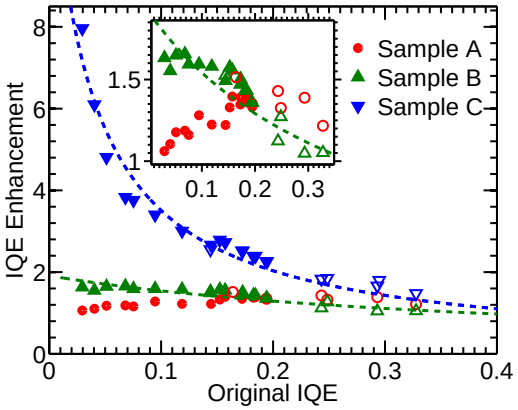

Figure 3.20: IQE enhancement factor with original IQE variation. The filled markers are calculated from the measurements of excitation power density variation (from Fig. 3.19(b)), while the non-filled markers are the same data given in Fig. 3.18(b) as calculated from the peak wavelength variation. Dashed lines are fitting based on Eq. (3.2). Inset is the zoom of IQE enhancement factor for sample A and B.

that the results of Fig. 3.18(b) was restricted to a limited range of original IQE from 0.15 to 0.32. The Purcell factor estimates from Fig. 3.20 are therefore more accurate.

As seen from the extinction spectra the LSPR of sample A is blue-shifted relative to the emission peak, while those of B and C are red-shifted. When increasing the excitation power density, in addition to the increase in IQE, the GaN/InGaN MQW peak emission wavelength is blue-shifted due to the screening piezoelectric field by free-carriers.[81,82] For the reference sample the emission peak around 528 nm is red-shifted to 537 nm when the excitation power is decreased to 1 mW/cm^2. Such a red-shift with decreasing excitation power is also present for samples A-C. For sample A this implies an emission peak shift towards the LSPR. As such, two competing mechanisms are present in the case of sample A when increasing the excitation power density – the first is the emission peak blue-shift, resulting in a better overlap with the LSP mode, and the second is an increase in original IQE from the increased carrier density, resulting in a reduced IQE enhancement factor from LSP coupling. The increasing enhancement factor of sample A (see inset of Fig. 3.20) can therefore be expected to be the result of increasingly better spectral overlap between the MQW emission spectrum and the LSP mode. In addition, this implies that a portion of the enhancement factor reduction of sample B and C with increasing carrier density may be attributed to the emission blue-shift away from the LSPR.

We also note that despite having the best spectral overlap between sample B resonance and the emission wavelength, the sample does not have the highest PL enhancement. This can be understood by considering the absorption and scattering properties of the Ag NPs. In the following chapter we will investigate these effects, and show that the scattering to absorption ratio is an important parameter when determining whether Ag NPs can provide efficiency enhancement. The absorption in the NP is the loss channel for the LSP mode, and reducing these losses relative to the scattering can ensure a higher LSP mode radiative efficiency. Despite the extinction or resonance peak of sample B matching the emission wavelength, sample C is expected to have a higher scattering capacity at the emission wavelength due to its larger average Ag NP sizes relative to sample B.[83] As such sample C is scattering dominated and sample A is absorption dominated, while sample B is in between these limits. As the emission is channeled into the LSP mode, the scattering efficiency of the NP is crucial when energy is to be re-emitted into free-space radiation.

3.3.5 Conclusions

We investigated the LSP-QW coupling and the resulting IQE enhancement of GaN/InGaN MQW LEDs with self-assembled Ag NPs. It was found that the strong PL enhancement was partly due to LSP-QW coupling, and partly due to LEE enhancement, and separating these effects we noted an IQE improvement due to LSP-QW coupling at 530 nm emission from 19 % to 44 % using large sized Ag NPs (sample C) at 756 W/cm^2.

It was also found that the IQE enhancement is strongly dependent on excitation power density, yielding highest enhancement factors at low free carrier densities. Where an IQE enhancement by a factor of 2.3 was observed at 756 W/cm^2, an enhancement factor of 8.1 was observed at 1 W/cm^2. Our results confirm the inverse relation between the aforementioned quantities, and implicate that it is imperative to take the excitation power density into account when conducting PL measurements to investigate the enhancement due to LSP coupling. We therefore establish quantitative enhancement factors depending on original IQE, and further confirm the fact that the lower the IQE of a light-emitting structure is, the higher the enhancement factor will be due to surface plasmons from Ag NPs.

CHAPTER 4

Radiative properties of localized surface plasmon modes

Coating the surface of a thin p-GaN LED with Ag nanoparticles (NPs) can significantly improve the photoluminescence (PL) intensity, but is not guaranteed. In most works where metal NPs are used to improve the emitter efficiency through localized surface plasmon (LSP) coupling, focus has been on matching the emission wavelength with the localized surface plasmon resonance (LSPR) of NPs. The objective being that at resonance wavelength the coupling will be strongest. Since the LSPR depends on metal NP size, much effort has been put into controlling the NP size to match the resonance wavelength with that of the emission.[34,59,83] The resonance is either estimated through the transmittance, reflectance or extinction spectrum. These measurement techniques do however include the contribution from the absorption inside the NPs, from which it is difficult to interpret whether the resonance is absorption or scattering dominated. It is therefore seen in some reported cases that PL enhancement is weakened[72] or even suppressed[83] when the resonance wavelength is near the emission wavelength. The important task of metallic NPs is to capture the emission from the active layer, and subsequently redirect the stored energy in the LSP mode into freely propagating photons, a figure of merit known as the LSP radiative efficiency, η_r, which was discussed in the previous chapter. Certain fraction of the energy will be dissipated inside the metal as heating losses, which is related to the absorption cross-section of the NP in the context of light scattering. On the other hand, the scattering cross-section will be an estimation of the particles efficiency in radiating the stored energy, which is required to maximize to achieve a better light extraction.

4.1 Scattering and E-field enhancement from Ag nanoparticles

In this section we study the scattering and LSP coupling dynamics of Ag NPs on GaN/InGaN multiple quantum-well (MQW) structures, and the mechanisms

behind PL suppression and enhancement using experimental and simulated results. As before, there is a 30 nm distance between the top-most quantum-well (QW) and the surface, and a total of 5 QWs with 12/2 nm barrier/well thickness. This time however, the epitaxial layers of the samples were un-doped, which is sufficient for PL characterization. Randomly self-assembled Ag NPs are fabricated and a dielectric layer of SiN between Ag and GaN surface is employed to modify the LSP mode for the investigations. PL and absorption spectra are obtained to characterize the samples. 3D finite-different time-domain (FDTD) simulations are implemented to calculate cross-sections and field enhancement factors of a single Ag NP on GaN/SiN substrate. The effects of particle diameter and SiN thickness variation are studied. By comparing the simulated and experimental results, we manage to give a detailed description of LSP-QW coupling and LSP radiation mechanism of Ag NPs on GaN/InGaN MQW structures.

4.1.1 Ag nanoparticle on dielectric-coated GaN

To modify the LSPR, a thin dielectric layer of SiN was deposited on some of the samples using plasma-enhanced chemical vapour deposition (PECVD), with a deposition thickness of 15 and 120 nm. To fabricate Ag NPs, a thin layer of Ag was e-beam evaporated on the samples followed by a 15 min rapid thermal annealing (RTA) process at 350 °C in vacuum. The different Ag film thicknesses used were 5, 10 and 15 nm, and the sizes of Ag NPs depended on this pre-annealed film thickness as shown in Fig. 4.1. There was no significant difference between the NP formation on SiN (GaN/SiN) compared to the bare GaN surface. The three different Ag NP distributions are denoted as A, B and C, referring to 5, 10 and 15 nm pre-annealed Ag thin film (TF), respectively. Each distribution is fabricated on samples with 0, 15 and 120 nm SiN layer, constituting nine samples in total (A1-3, B1-3 and C1-3). The average particle diameter of sample A, B and C is approximately 50, 110 and 160 nm, respectively.

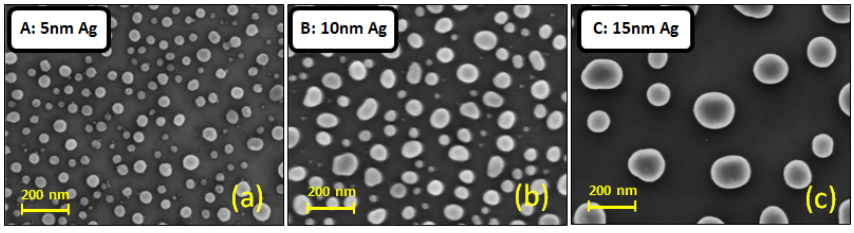

Figure 4.1: SEM images of self-assembled Ag NPs, with pre-annealed Ag film thickness of **(a)** 5 nm, **(b)** 10 nm and **(c)** 15 nm.

To obtain further insight on the LSPR of Ag NPs, the normalized absorption spectra, $A_{\mathrm{Ag}}/A_{\mathrm{ref}}$, were obtained from transmittance, T, and reflectance spectra, R, as shown in Fig. 4.2 for samples without SiN and with 15 nm SiN, by assuming

$A = 1 - T - R$. It is clearly noticed for samples A1-2 and B1-2, that the LSP absorption peaks blue-shift as the SiN is included. A strong and well-defined absorption peak was not visible for C1 and C2.

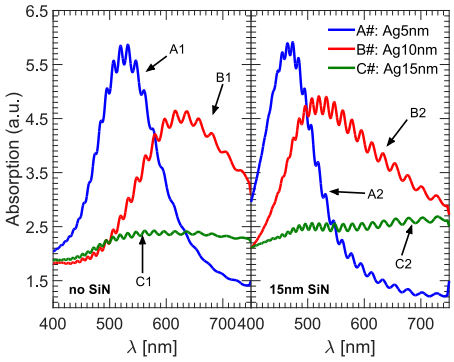

Figure 4.2: Normalized absorption spectra for samples without and with 15 nm SiN between GaN and Ag NPs.

4.1.2 PL characterizations

For PL measurements, the excitation and detection was done from the polished sapphire side. The PL spectra are plotted in Fig. 4.3. For each three cases of different SiN thickness, the reference has the same SiN thickness but does not have Ag NPs. This is to exclude the PL enhancement from the dielectric layer itself. The PL spectra with Ag NPs are normalized to the peak value of its corresponding reference. For samples without SiN we observe an integrated PL enhancement (IPLE) of a factor 2.4 with sample C1, while sample B1 shows an almost unchanged PL spectrum. Sample A1 which has the smallest Ag NP size distribution shows PL suppression.

The metal NPs can induce an increased back reflection of both the excitation laser and the MQW emission at the substrate-metal interface, which will cause an additional PL enhancement unrelated to LSP-QW coupling. However, it has been confirmed through internal quantum efficiency (IQE) as in the previous chapter, time-resolved PL (TRPL), and electroluminescence (EL) measurements, that a PL enhancement due to metal NPs based on the current excitation and detection scheme can indeed be attributed to LSP-QW coupling.[39,46,53,54,59,71–73] Nonetheless, it is still required to exclude the contribution from the enhanced reflection of the excitation source due to Ag NPs as done by Henson *et al.*,[72] as well as the enhanced reflection at the emission wavelength. The inset of Fig. 4.3 shows the reflectance spectra, where it is seen that samples B1 and C1 have an enhanced reflectance of nearly a factor of 1.5. The reflectance spectra of the remaining samples, A2-3, B2-3 and C2-3 show a similar trend as A1, B1 and C1. The ab-

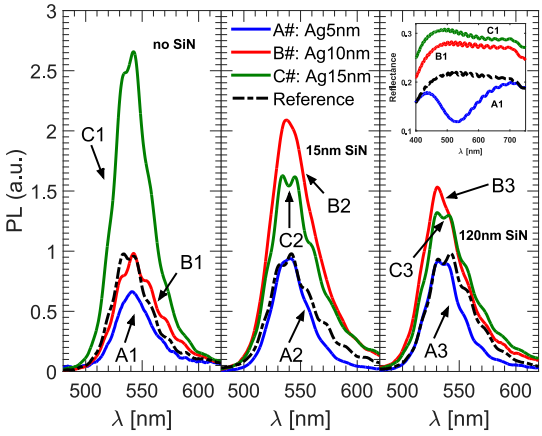

Figure 4.3: Reflectance corrected PL spectra of the nine samples with Ag NPs and three references without Ag NPs. Inset shows the reflectance spectra of A1, B1 and C1.

sorbed excitation intensity in the QWs is roughly assumed to be proportional to the incident plus the reflected intensity at excitation wavelength, i.e. $1 + R$. If the inclusion of Ag NPs increases the reflectance from R to R_{Ag}, the absorption will be increased by a factor $f_{\mathrm{refl}} = (1 + R_{\mathrm{Ag}})/(1 + R)$. To exclude reflectance enhancement effects the PL spectra of B1-3 and C1-3 has been divided by a factor of $K = f_{\mathrm{refl}} r_{\mathrm{enh}}$, where $r_{\mathrm{enh}} = R_{\mathrm{Ag}}/R$ is the enhancement at emission wavelength and R is the reflectance before Ag NP coating. In Fig. 4.3 the PL correction factor K has already been taken into account and the observed PL enhancements can therefore be attributed to LSP coupling.

Interestingly, the situation is drastically affected by the inclusion of a SiN layer. We observe that with 15 nm SiN the IPLE of sample C2 is reduced to 1.8. This is in agreement with the expectation that coupling strength is reduced with increasing distance between QWs and Ag NPs.[39] However, the opposite trend is seen for sample B2, which displays an IPLE of a factor of 2.1. The situation of sample A2 also shows improvement, in the sense that the PL is not suppressed as it was for A1, although the PL of A2 is still not enhanced relative to the reference. We also observe that with a 120 nm SiN layer Ag NPs still manage to result in a PL enhancement, even though the distance between NPs and QW active region is greatly increased. The IPLE factors of samples B3 and C3 are 1.6 and 1.5, respectively. This is nonetheless related to light extraction efficiency (LEE) enhancement effects.

When designing for surface plasmon (SP) enhancement using metal NPs, the usual strategy is to compare and match the LSP resonance peak with the emission wavelength, where the LSPR is estimated through a dip in the reflectance

or transmittance spectrum.[46,59,60,71–73,84] It is expected that SP enhancement of GaN/InGaN QWs is optimized by matching the resonance and emission wavelengths. We are, however, observing a situation where a strong PL enhancement is obtained for sample C1 despite the absence of a well-defined absorption peak. Although samples A1 and B1 have well-defined resonance peaks near the emission wavelength, no PL enhancement is obtained. To clarify these ambiguities in our experiments, as well as previous observations, we need to quantify the two competing factors, i.e. light scattering (or re-emission) and absorption in the excitation of LSP modes. A measurement of the reflectance and transmittance spectra reveals information about the absorption of NPs, and this is subtly related to the LSPR and LSP-QW coupling. Essentially, it is the competing effect between scattering and absorption that ultimately determines the optimal efficiency of plasmon mediated light-emitting devices. This scattering, which is related to the radiative efficiency of LSP modes, determines the SP enhancement properties of metal NPs. By only considering the absorption spectrum it is not convincible to conclude that an absorption peak spectrally aligned with the emission wavelength can result in an enhancement through LSP-QW coupling.

4.1.3 Absorption and scattering cross-sections

To understand the observed measurements, we conducted 3D FDTD simulations to investigate the absorption and scattering properties of Ag NPs on GaN/SiN substrate. As seen from Fig. 4.1 the particle size distribution and inter-particle spacing are randomly distributed around an average value, and simulating a large ensemble of randomly distributed NPs with an acceptable accuracy would require relatively large computational resources. However, if we assume that the interaction between the Ag NPs is weak and neglectable when interacting with light, it will be sufficient to simulate a single Ag NP. By modelling a single NP we can obtain the properties of an ensemble of non-interacting NPs. The results will help us gain a qualitative understanding of the observed measurements. We have not simulated a periodical arrangement of NPs to avoid grating effects and resonances which are not present in a random distribution.[85] In the simulations the NPs are assumed to have the shape of a spherical dome. The size variations seen in the SEM images of Fig. 4.1 are simulated through separate instances by a diameter sweep. The variation of the optical properties with diameter will give us an understanding of how such an ensemble of non-interacting particles with varying sizes respond to light illumination. The Ag NP height is set to $H = \alpha D/2$, where D is the NP diameter, and $\alpha = 1.8$ is a fixed aspect ratio.

Fig. 4.4(a) shows the absorption cross-sections σ_{abs} for particle diameters of $D = 50$, 110 and 160 nm (D50, D110 and D160), without and with 15 nm SiN layer, where comparisons are to be made with samples A1-2, B1-2 and C1-2, respectively. In agreement with experimental measurements, we observe a blue-shift of the absorption peak when including SiN for D50 and D110. The observed peak is

the LSP mode which is confined at the substrate-metal interface. Another feature consistent with the measurements is the fact that for D50 and D110 the spectrum shows a well-defined absorption peak as is the case for the Ag NPs of samples A1-2 and B1-2. The simulations of D160 also reveal that the absorption spectra of large NPs do not show a well-defined peak, which is consistent with the absorption measurement of the Ag NPs on samples C1-2. There is an apparent disagreement when considering the absorption strengths, where the strongest absorption occurs for samples A1-2, which for the simulations corresponds to D50. However, it should be noted that the particle density (particles per unit area) increases with decreasing particle size, such that samples A1-2 has the highest density, and C1-2 has the lowest density as seen in Fig. 4.1. With a larger number of particles, the absorption would correspondingly be higher. Therefore even though the single particle absorption strength of samples A1-2 according to simulations should be lower than B1-2 and C1-2, the larger density of particles on sample A1-2 would in total result in larger absorption than B1-2 and C1-2.

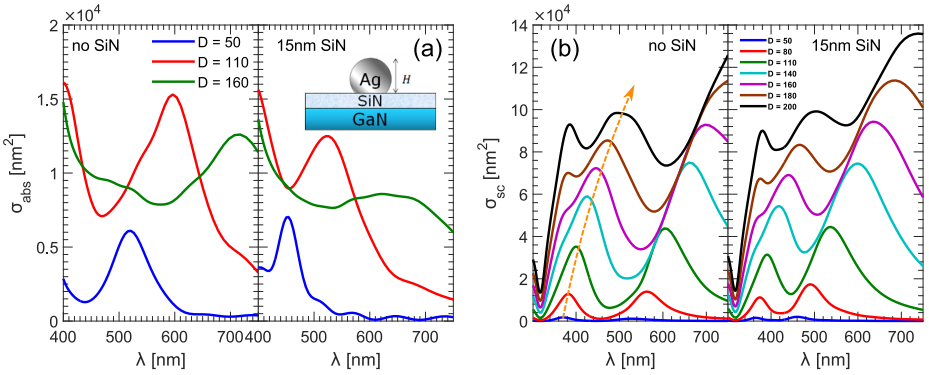

Figure 4.4: Simulation results of a single Ag NP on GaN/SiN substrate. **(a)** Absorption cross-sections at three diameters. **(b)** Scattering cross-section spectra for different NP diameters. The arrow shows the direction of increasing diameter D and position of the metal-air LSP mode.

Fig. 4.4(b) shows the scattering cross-sections σ_{sc} for particles of various diameters. As mentioned, scattering is the significant parameter when considering SP enhancement of GaN/InGaN QWs through LSP-QW coupling, and here we see that increasing the particle size, D, increases the scattering, which is a well-known result in the dipole approximation.[34] The simulations also reveal a red-shift of the resonance peak with increasing diameter. For diameters larger than $D = 160$ nm a higher-order scattering mode is seen to emerge below 400 nm. The peak indicated by the arrow is the metal-air LSP mode, which is seen to red-shift with

increasing size. The metal-air mode for largest particle is located around 500 nm, which is below the emission wavelength. Another point to note is the fact that a well-defined scattering resonance peak exists despite its absence in the absorption cross-section spectrum, as is the case for D160 with 15 nm SiN.

Considering the increasing scattering cross-section with increasing particle size, we can partially understand how a PL enhancement can be obtained in the case of samples C1-3. The absence of a resonance peak at the emission wavelength is not equivalent to the absence of LSP scattering. This is evident from Fig. 4.4(b), where if we consider the sample of diameter $D = 160$ nm, we notice that its scattering cross-section values throughout the whole wavelength range from 400 to 750 nm, even in the valleys, exceed the peak scattering value of the sample with $D = 110$ nm for the 15 nm SiN case. This means that even at off-resonance conditions large Ag NPs have strong scattering capabilities, which is a requirement for SP enhancement.

From the PL measurements in Fig. 4.3, it was noticed that the PL suppression in case of sample A1 was neutralized by the inclusion of SiN. This can be understood when considering the fact that the absorption peak is blue-shifted away from the emission peak. In Fig. 4.5(a) we have the simulation result of absorption cross-section variation with particle diameter on different substrates. The absorption peak around $D = 80$ nm is seen to be shifted towards $D = 110$ nm by including SiN, resulting in a reduced absorption below 80 nm. This can explain why the inclusion of SiN neutralized the PL suppression for sample A1 with average Ag NP size around 50 nm, as seen for A2-3.

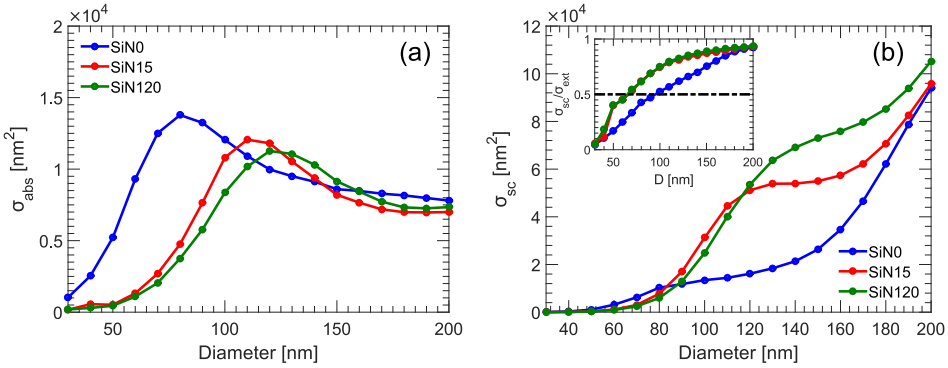

Figure 4.5: **(a)** Absorption and **(b)** scattering cross-section variation with particle diameter at $\lambda = 538$ nm. The inset shows the scattering to extinction ratio. The substrates are GaN (SiN0), 15 nm and 120 nm SiN on GaN (SiN15 and SiN120).

To understand the behavior of samples B1-3 and C1-3 when going from a GaN to GaN/SiN substrate, we consider the scattering cross-section variation with diameter in Fig. 4.5(b). The essential feature to notice here is the increased scattering from around 90 to 180 nm diameter when a 15 nm thick SiN slab is included, resulting in an increase of the scattering by a factor of 3.1 and 1.6 at $D = 110$ and 160 nm, respectively. To also take into account the effects of absorption we consider the scattering-to-extinction ratio (SER) $\sigma_{\mathrm{sc}}/\sigma_{\mathrm{ext}}$, where $\sigma_{\mathrm{ext}} = \sigma_{\mathrm{abs}} + \sigma_{\mathrm{sc}}$. This parameter qualitatively reveals if a NP of a given size is scattering ($> 1/2$) or absorption dominated ($< 1/2$) in itself. This is shown in the inset of Fig. 4.5(b), where the dashed horizontal line at 0.5 is the value at which the absorption and scattering are equal. Without SiN the SER at $D = 110$ nm is 0.56, implying a relatively large dissipation compared to the scattering by Ag NPs of the given size. With a SiN layer the ratio is increased by 40 % for $D = 110$ nm. While the SER for the sphere $D = 160$ nm increases moderately, i.e. by 9.8 % with inclusion of SiN slab. Considering the PL measurements of samples B1-2, we therefore believe that the increased scattering is the mechanism behind the increased PL intensity from B1 to B2 when the SiN layer is introduced. The SER also reveals that for $D = 50$ nm, the value is below 0.5 regardless of SiN layer, which implies an absorption dominated operation for such small NPs. The SiN does however increase the ratio from 0.17 to 0.40, implying a decreased dissipation relative to the scattering. This explains how there can be an improvement in the PL intensity when going from A1 to A2 relative to the reference, when including the SiN layer, although no PL enhancement is observed.

4.1.4 Field intensity enhancement in the QW plane

The scattering results in Fig. 4.5(b) can explain why sample B1-2 has an improved PL intensity with 15 nm SiN, but does not explain why the PL enhancement of sample C2 is reduced compared to C1, and exceeded by sample B2. The scattering and absorption cross-sections of Ag NP reveal information about the radiative efficiency of the LSP mode, but it does not tell us anything about the energy transfer or coupling between LSP-QW. To investigate this coupling, we will consider the field intensity enhancement $|E|^2$ in the plane of the QWs due to the Ag NP. This parameter will correspond to the decay rate enhancement of optical emitters positioned in the near-field of a metal NP.[86] In the simulations with a single Ag NP we calculate the average field intensity enhancement over an area of $1.5D \times 1.5D$ at the plane of the top-most QW below the NP. The results are shown in Fig. 4.6(a), where the intensity enhancement spectra of three different sized particles are shown on three different substrates. As a comparison we have Fig. 4.6(b) which shows the PL ratio between the samples with Ag NPs and the reference from the experimental results of Fig. 4.3.

The situation without SiN of Fig. 4.6(a) shows that the field enhancement factor for an Ag NP of diameter $D = 160$ nm exceeds that of a diameter $D = 110$ nm in a range from about 460 to 560 nm. With 15 nm SiN the D110 particle has a higher field enhancement factor than D160 in the range from 510 to 610 nm. The field enhancement spectrum is related to the scattering cross-section and hence also affected by the blue-shift of the peak scattering due to SiN. Although the peak enhancement of D110 is reduced, it is nonetheless shifted towards the emission peak of the QWs. It is also noticed that for wavelengths above 610 nm, the enhancement of D160 starts to exceed that of D110 with 15 nm SiN. This appears to be closely related to the scattering peak being located near 635 nm for D160, though the peak enhancement is located at about 680 nm. When considering the 120 nm SiN layer, the distance between the Ag NP and the QW region is 150 nm, and yet there is still a small field enhancement up to a factor of 1.5 remaining for D110 and D160. Around the emission peak the enhancement is once more higher for D110 than for D160.

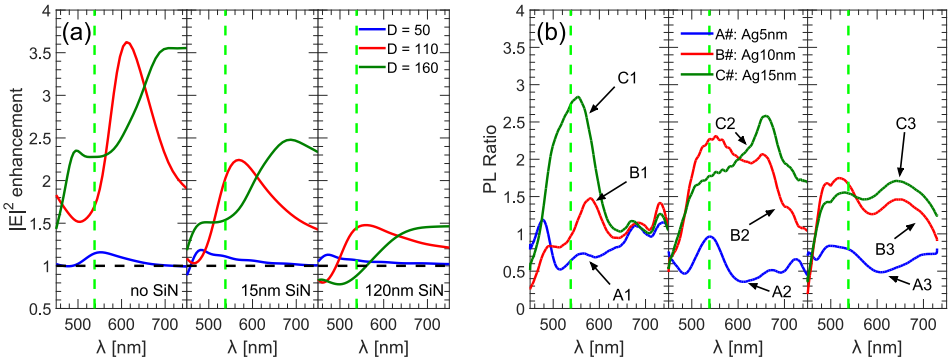

Figure 4.6: **(a)** Intensity enhancement spectrum by Ag NP on GaN/SiN substrate. **(b)** PL ratio of the measurements in Fig. 4.3. The vertical lines show the position of the emission peak at 538 nm.

Comparing now with the experimental results in Fig. 4.6(b), we observe a similar trend with the PL ratios, where the PL enhancement of sample B2 exceeds that of sample C2 close to the emission peak, when using 15 nm SiN. The peak of sample C2 PL ratio is likely to have originated from a Fabry-Perot oscillation feature in the PL signals. Nonetheless, for wavelengths above 600 nm the PL enhancement of C2 is higher than that of B2, which is a similar situation to that seen from the simulations in Fig. 4.6(a) with 15 nm SiN. For the samples with 120 nm SiN a relatively large enhancement factor of nearly 1.5 is present for B3 and C3. The feature which is roughly captured by simulations is the stronger PL enhancement of sample B3 relative to sample C3 for wavelengths near and below the emission peak, while the PL enhancement of sample C3 dominates at longer wavelengths.

It should be noted here that only the top-most QW in the samples can experience the level of intensity field modification predicted by the simulations. QWs with increasing distance to the surface will experience a decreasing field strength, and the field enhancement factors will therefore only account for a fraction of the enhancements seen from the PL ratios. As we demonstrated in the previous chapter, the Ag NPs will lead to an improved LEE, e.g. through LSP-TIR coupling, hence part of the improvement can be attributed to LEE.

To summarize the above results, we consider the intensity enhancements at the emission wavelength, 538 nm, and its variation with particle diameter as shown in Fig. 4.7. With only a GaN substrate (SiN0), the peak enhancement is located around $D = 180$ nm. By including the SiN layer the peak is shifted to around $D = 100$ nm, irrespective of the SiN thickness. The point which is reiterated is that particles with D around 110 nm have an improved field intensity enhancement with a thin SiN layer (SiN15) compared to bare GaN substrate (SiN0), while particles with D around 160 nm have a degraded enhancement.

It is now possible to understand the PL results of Fig. 4.3, where sample C1 has the strongest enhancement without SiN, while sample B2 dominates with SiN and sample C2 is degraded relative C1. Even though we only considered a single Ag NP, the simulations nonetheless qualitatively explained the measurements. The validity of this estimation holds if we neglect the interactions between the different Ag NPs on our samples. The accuracy of this approximation is further improved by the fact that the Ag NPs have random variation in size and position, which means that we do not have any grating effects, such as strong particle interactions and grating modes. We believe that the single NP model does well in explaining the observed trends in our measurements qualitatively. Using this simple model we have managed to understand how the PL enhancement of the samples (B1-3)

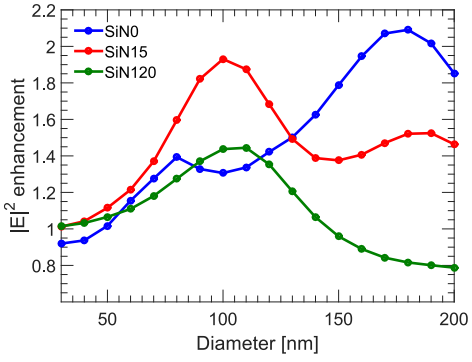

Figure 4.7: Intensity enhancement variation with Ag NP diameter at 538 nm wavelength on different substrates.

with average Ag NP size around 110 nm can be improved by including a SiN layer when considering scattering and absorption cross-sections of Ag NPs of a similar size. Through the results of Fig. 4.5 and Fig. 4.7 we have managed to obtain consistent explanations and conclusions about our measured results.

4.1.5 Conclusions

We have investigated the effects of SP enhancement using different sized Ag NPs on different substrates. By including a 15 nm SiN layer, we found an improvement of the PL intensity for samples with small sized NPs. This could be explained by an improved scattering and LSPR blue-shift of the NPs when the substrate was modified. We have found that what is important to consider when working with metal NPs for SP enhancement, is not only the absorption dip in the transmittance or reflectance spectra, but rather the combined effects of absorption, scattering, scattering-to-extinction ratio, and field enhancement. It is relatively easy to obtain metal NPs with resonances matching the emission wavelength, but it does not ensure SP enhancement of the optical emitter if the NPs cannot scatter the stored energy efficiently. Using a simplified modelling of Ag NPs we could reasonably explain the observed measurements, and we found that in order to improve the efficiency of the QW structure through LSP coupling the metal NPs should have a large SER. This could be achieved by either increasing the NP size or by modifying the environment of the NPs, i.e. including a SiN layer on GaN.

4.2 LSP coupling using Au nanoparticles

In the previous chapter we investigated thin films for surface plasmon polariton (SPP) enhancement using different metals, and found that Au TF had a negative effect on PL intensity due to its absorption, similar to what was reported by Okamoto *et al.* using a single QW structure.[39] In this section, we will investigate how Au NPs affect GaN/InGaN QW emitters, and for comparison with the discussions of Ag NPs, the same epitaxial structures will be investigated, where the distance between the top-most QW and the GaN surface is 30 nm. We use the same simulation formalism as in the previous section to understand the results of PL measurements. Our findings show that Au NPs in the near-field of GaN/InGaN QWs only quenches the PL intensity, irrespective of the LSPR position and the particle size.

4.2.1 Recent developments using Au nanoparticles

It has been reported by various groups that using Au NPs in the near-field of a light-emitter can modify the emitter decay rate, although a fluorescence enhancement is not always the case. In general, metals are known to quench emitter radiation in their near-field, and for Au NPs, this was demonstrated by Dulkeith *et al.*[87] using dye molecules in a solution containing Au NP. Using TRPL, they showed that PL quenching was the result of a drastic increase in the non-radiative decay rate. Kulakovich *et al.*[88] showed, using Au colloids in the near-field of CdSe QD emitters, that the PL suppression or enhancement due to coupling with LSP modes, are range dependent effects; that at short emitter-NP range the PL could be quenched, and enhanced at longer ranges. The emitters in the mentioned studies had emissions around red wavelengths, however, using ZnO nanowires with a wide-band emission spectrum covering the blue-green-red region, Chen *et al.*[89] showed that Au NPs could enhance the orange-red part of the spectrum, while quenching the blue-green part. This is an important property of Au NPs, as they exhibit LSP mode resonance around the red wavelength regions.

One group has recently investigated the use of Au NPs on green GaN/InGaN MQW LEDs. They demonstrated PL and EL enhancement by depositing Au NPs on a 20 nm thin *p*-GaN, followed by a 150 nm thick *p*-GaN growth on top of the NPs;[90] an LED design corresponding to that discussed earlier and shown in Fig. 3.1(b). The NPs were formed by annealing Au TF with a thickness of 0.2 nm at 800 °C for 3 min. Although they measured the TRPL of samples with and without Au NPs, the measurements were done at 10 K, and they showed that the PL life-time was decreased from 51 ns to 30 ns. However, LSP coupling is a process which has been demonstrated to be temperature dependent, and to decrease with temperature in a same manner as non-radiative recombination processes.[53,79] Considering this important fact regarding LSP coupling mechanisms, it is difficult to draw the conclusion that LSP coupling due to Au NPs are responsible for the observed PL and EL emission enhancement. Later on, another demonstration of

PL enhancement was achieved through the formation of Au NPs inside the n-GaN layer as shown in Fig. 3.1(c), by the same group,[91] this time also showing IQE improvement. Although it might be difficult to determine whether the improvement was due to LSP coupling or improved MQW crystal quality, as the substrate conditions for the QWs were different between the test and reference samples.

4.2.2 Au NP coating and PL characterizations

We fabricated self-assembled Au NPs of various sizes by thermally annealing Au TF of different thicknesses. The annealing was done at 650 °C for 5 min in vacuum. The result of annealing for four different samples (A-D) are shown in the SEM images of Fig. 4.8, with Au TF thickness of 3, 6, 9 and 12 nm. The particle sizes are seen to increase more rapidly with TF thickness compared to the situation of Ag. The average particle sizes are approximately 30 nm, 170 nm, 350 nm and 950 nm.

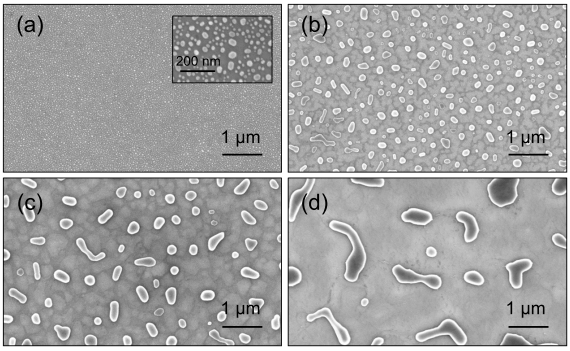

Figure 4.8: SEM images of Au NP, formed after annealing **(a)** 3 nm, **(b)** 6 nm, **(c)** 9 nm and **(d)** 12 nm Au thin film.

As before, we conducted PL measurements such that each sample is compared with its pre-coated PL spectrum. Previously, we only considered the emission from the sapphire side, however, in this experiment we also measured the emission from the top GaN surface as shown in Fig. 4.9(a). The PL spectra of the Au NP coated samples are shown in Fig. 4.9(b), where the emission peaks are located around 527 nm. As it can be seen, the PL is strongly quenched for all the sizes of Au NPs. The emissions from the sapphire side appear to be more degraded compared to the GaN side emissions. The red-shift of sample D compared to the others is due to as-grown sample emission spectrum. Samples A and B with the smallest NP sizes demonstrate the strongest PL suppression.

To observe any possible LSP coupling features we also show the PL ratios relative to the pre-Au coated samples in Fig. 4.10(a). A weak trend of decreasing PL quenching is observed with increasing NP size, which is clearer from the GaN-side emission. For all the samples the PL quenching is red-shifted relative to the

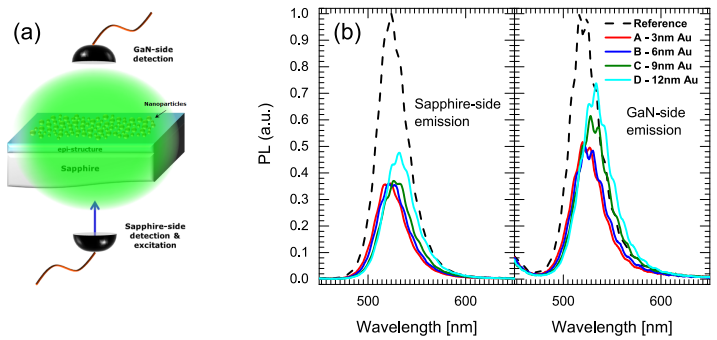

Figure 4.9: **(a)** The PL experimental setup, with the sapphire and GaN detection schemes. Excitation is from sapphire side. **(b)** The PL intensity spectra of the samples after Au NP coating from sapphire and GaN side.

emission peak. From transmittance measurements in Fig. 4.10(b) the absorption and hence LSPR locations are visible through the dips in the spectra. Only samples A and B display well-defined resonance locations around 576 nm and 715 nm, respectively. Samples C and D each have a flat transmittance curves, although with a reduced transmission compared to the reference.

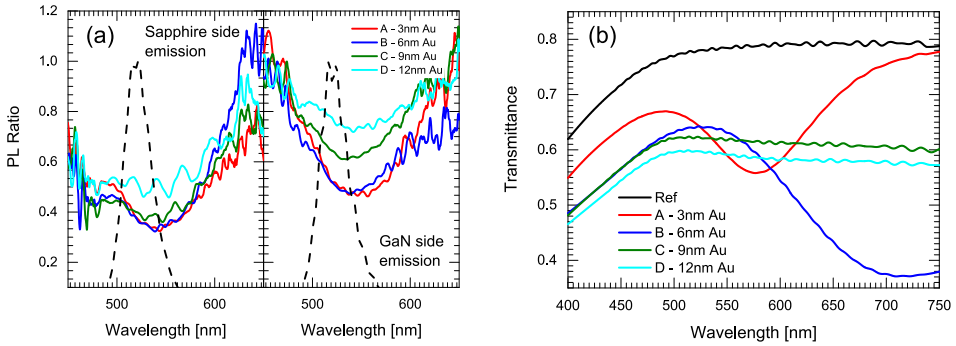

Figure 4.10: **(a)** PL ratios for Au NP coating relative to the reference. The black dashed curve is the emission spectrum for comparison. **(b)** The transmittance spectra using a Xe white-light source, with transmission from sapphire to GaN side.

4.2.3 Scattering and field intensity enhancement

We will in this section employ the simulation models used in the previous section to describe the behaviour of Ag NPs. We will give a qualitative explanation of

the observed results with PL suppressions and the Au NP size dependence. For comparison purposes with the Ag NP simulations earlier, the Au NP geometry will be similar, i.e. with aspect ratio $\alpha = 1.8$, and particle height, $H = \alpha D/2$.

The scattering cross-section for different diameters are shown in Fig. 4.11(a). The trend of increasing scattering with NP size is similar to that of Ag NP. However, the LSPR positions are located at longer wavelengths, and by increasing the NP size, the peak located at the longer wavelengths (metal-substrate mode) is red-shifted more significantly than the one located at shorter wavelengths (metal-air mode). Taking the absorption cross-section into consideration we calculate the SER spectra, shown in Fig. 4.11(b). It is noticed that the SER mainly remain below or around the critical factor of 0.5, indicating an absorption dominated operation at the 527 nm emission wavelength of the QWs.

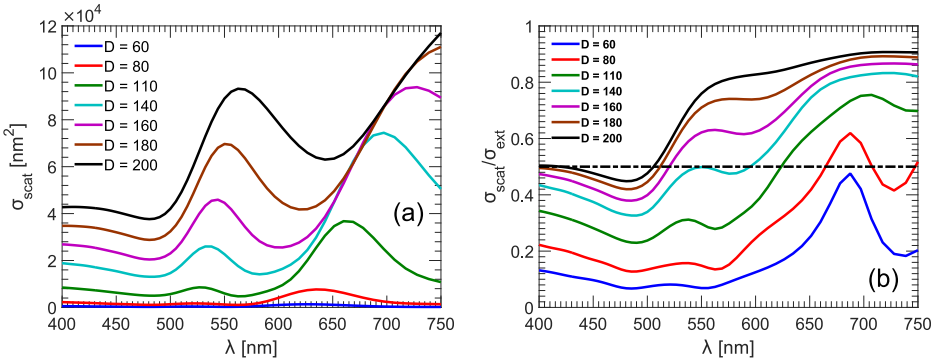

Figure 4.11: **(a)** Simulated scattering cross-section for Au NPs of different diameters on GaN substrate, and **(b)** the scattering-to-extinction ratio as a function of wavelength.

Even though the SER reaches above 0.5 for larger Au NPs, the LSP mode around this wavelength is a metal-air mode as shown in Fig. 4.12(a), which is both weaker and further away from the top-most QW than the metal-substrate mode illustrated Fig. 4.12(b). This mode is therefore not expected to provide efficient LSP-QW coupling. Nevertheless, the mode profiles do provide some explanation regarding the difference in PL suppression when considering the emission from sapphire and GaN side. Samples A-D showed a less degree of PL suppression from the GaN side, and considering the mode profile and wavelength of the metal-air mode (as shown in Fig. 4.12(a)), it is not surprising that more light is emitted from the top GaN side at the 527 nm emission wavelength compared to the sapphire side.

The fact that the metal-substrate LSPR is located far away from the MQW emission peak is not enough to conclude PL quenching, since we saw earlier that the large Ag NPs could provide strong PL enhancement despite having metal-

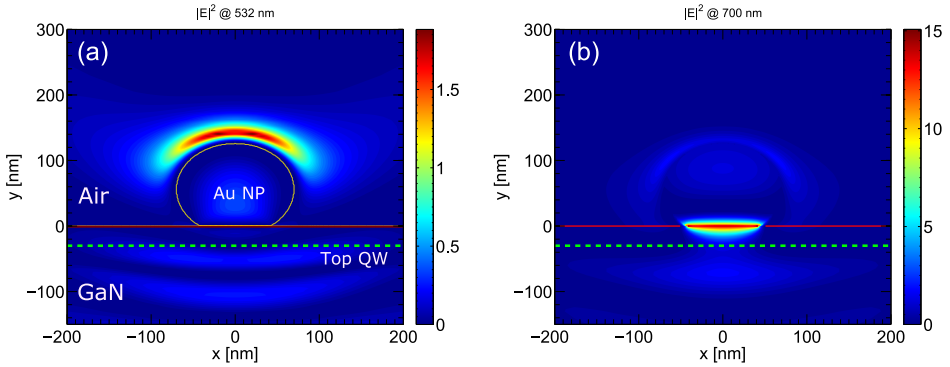

Figure 4.12: Scattered field intensity profiles from substrate excitation of an Au NP LSP mode, with a NP diameter of $D = 140$ nm at **(a)** 532 nm and **(b)** 700 nm wavelength. The dashed line shows the position of the top-most QW.

substrate LSPR located above 600 nm. As such we investigate the field intensity enhancement at the plane of the top-most QW, the spectra of which are shown in Fig. 4.13(a). The field is seen to be significantly enhanced at wavelengths above 550 nm. Below this wavelength, the enhancement factor is barely affected by the NP size variation, which is more clearly illustrated by the diameter variation in Fig. 4.13(b). At the 527 nm emission wavelength of the considered samples (A-D), the field intensity remains largely unchanged even with the presence of Au NP. Moderate enhancements can be obtained with large Au NPs above 550 nm emission wavelengths, which should be useful for yellow-red colour LED devices, considering the relatively large values of SER.

4.2.4 Conclusions

Despite the reports of PL enhancements using Au NPs in the near-field of light-emitters, we have not been able to observe this effect around green emission wavelengths. Our results have shown that Au NPs placed on the GaN surface and located 30 nm from the top-most QW result in a PL suppression independent of NP size. This could be explained as being due to the weak field intensity enhancement and the fact that only the metal-air LSPR was located near the green emission wavelengths of the samples used.

An important difference between our setup and those designed by S.J. Park *et al.*,[90,91] is the Au NP environment, where the NPs in their experiments are embedded inside GaN, while in our case the NPs are positioned on a GaN substrate surrounded by air. Despite our efforts to recreate their environment by coating the Au NPs of samples A-D with 130 nm TiO_2 layer using atomic layer deposition,

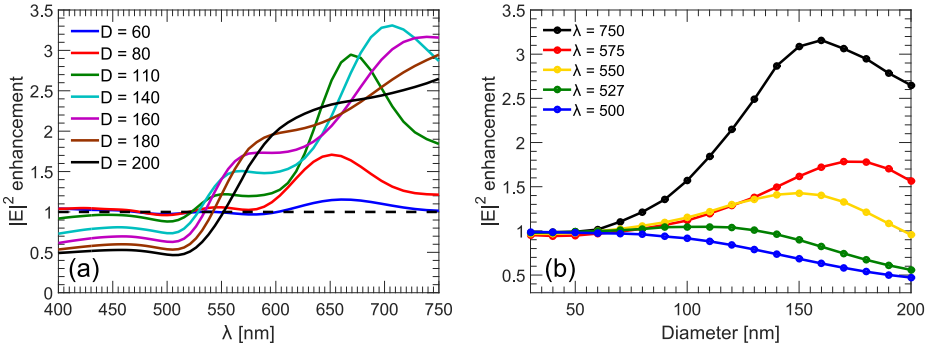

Figure 4.13: **(a)** Field intensity enhancement spectra in the plane of the QWs due to an Au NP, and **(b)** and its size dependence.

the results were the same – PL quenching for all the tested Au NP sizes. The refractive index of TiO_2 at the emission wavelength is 2.67, which is close to the 2.43 of GaN, thus it was expected that the Au NPs would have an environment similar to those embedded inside GaN.

In conclusion, Au NPs are not an ideal choice of SP-metal for PL enhancement when considering green emission GaN/InGaN QW emitters. Reports have suggested that they might be of interest for yellow-red emission colours, but due to the lack of InGaN based QW emitters at these wavelengths, we have not been able to make the necessary investigations.

CHAPTER 5

Surface plasmonics on patterned dielectric

In the previous chapter we investigated the effects of modifying the Ag nanoparticle (NP) substrate by including a dielectric intermediate layer, and how the environment could change the surface plasmon coupling and radiative efficiency of the nanoparticles. The effects due to the dielectric coating alone were not analysed. The thin silicon nitride coating has in fact demonstrated to increase the photoluminescence (PL) intensity of the investigated samples, but this was not shown in Section 4.1. We will in this chapter investigate different types of dielectric coating on similar multiple quantum-well (MQW) samples as considered in the last chapter, and furthermore consider Ag NP formation through the self-assembly approach using thermal annealing. Both a conventional thin film (TF) and a novel nano-patterned dielectric coating are considered.

5.1 The effect of dielectric thin films

The effects of dielectric coating on Ag NP formation, PL intensity and localized surface plasmon (LSP) coupling are investigated in this section. We consider two types of dielectrics – silicon nitride and silicon oxide deposited using plasma-enhanced chemical vapour deposition (PECVD).

The nitride glass deposition is done using silane (SiH_4), ammonia (NH_3) and nitrogen (N_2) with flowrates of 30, 20 and 1000 sccm, respectively, while process temperature, pressure and RF power were 300 °C, 500 mTorr and 80 W, respectively. The dielectric stoichiometry is $Si_xN_yH_z$, though we will shortly denote this as SiN. The refractive index at 633 nm wavelength is measured to be around 1.9-2.0 using an ellipsometer. For silicon oxide deposition, SiH_4 and N_2O are used at 12 and 710 sccm, respectively, with a process pressure of 700 mTorr and RF power of 150 W. The stoichiometry is $Si_xO_yH_z$, and the refractive index is between 1.45-1.48, which we will simply denote as SiO_2.

The dielectrics are deposited on similar GaN/InGaN MQW green emitters as previously considered, with emission peak wavelength around 530 nm, and where the distance between the top-most quantum-well (QW) and the GaN surface is 30 nm. The SiN and SiO_2 coatings considered in this chapter all have a 20 nm thickness. The reason for choosing 20 nm is due to the relatively large deposition

rate of PECVD SiO_2 which was measured to around 1.57 nm/sec. The plasma will not be stable below 10 sec of operation, and it is therefore difficult to ensure a 15 nm thick SiO_2 film.

5.1.1 Nanoparticle self-assembly on different substrates

We form Ag NPs through the same process as described earlier, i.e. rapid thermal annealing (RTA) at 350 °C for 15 min in vacuum. However, due to the different surface conditions between the bare GaN and the dielectric coated on GaN, the self-assembly of the NPs will be different on each surface. A comparison is shown between the particle size distributions on GaN and SiN surface in Fig. 5.1. These self-assembled NPs are formed by thermally annealing a 7.5 nm Ag TF under the same condition for both surfaces. The particle size, D, is defined as $D = 2\sqrt{A/\pi}$, where A is the cross-sectional area of a NP. Hence D corresponds to the diameter of an equivalent particle with circular cross-section. On GaN surface the average particle size is about 88 nm with a 29 nm standard deviation, and as seen in the inset of Fig. 5.1(a), the particles have irregular shapes. On the other hand, Ag NPs formed on SiN surface have an average size of 63 nm and a size standard deviation of 19 nm, and the particles are less irregular as shown in the inset of Fig. 5.1(b). Self-assembled NPs from 7.5 nm Ag TF, formed on a 20 nm SiO_2 surface result in an average particle size of 77 nm.

The different sizes obtained can be explained as being due to the different surface roughness between the samples, where the epitaxially grown GaN surface has least roughness. The surface roughness of the as-grown GaN surface and the SiN coated surface is shown by the atomic-force microscope (AFM) images in

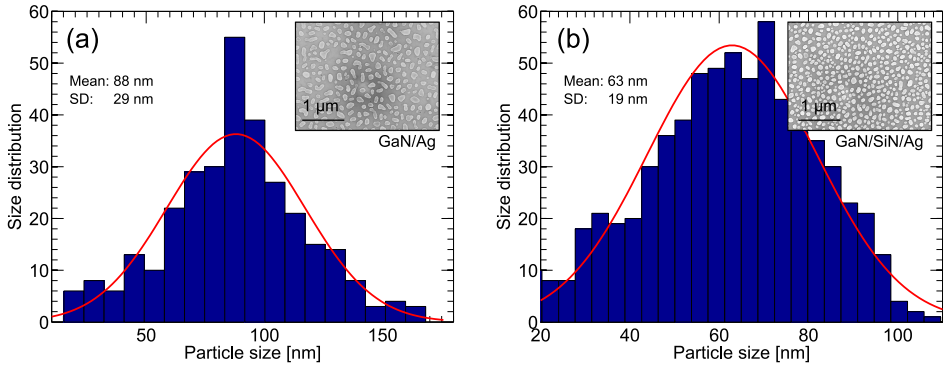

Figure 5.1: Approximate size distribution of self-assembled Ag NPs after thermally annealing a 7.5 nm Ag TF deposited on **(a)** bare GaN surface and **(b)** a 20 nm SiN coating on GaN surface. The insets show SEM images of the Ag NPs from the top.

Fig. 5.2. The root-mean-square (RMS) of the GaN surface, without including the pit and trench defects, is around 0.23 nm with peak-to-valley height variations in the range of 1.4 nm. The SiN coating increases the RMS to 0.68 nm and the peak-to-valley height variations to around 6.5 nm.

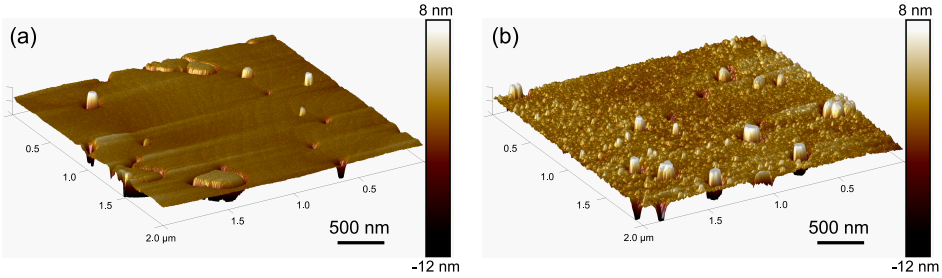

Figure 5.2: AFM images of the MQW epi-structure, showing **(a)** the bare GaN surface, and **(b)** the GaN/SiN surface with 20 nm PECVD SiN TF thickness.

The particle size difference on GaN and SiN was not considered in Section 4.1, during the study of Ag NPs on SiN surfaces, due to its insignificance. As will be seen in Section 5.2 with patterned dielectric, Ag NPs formed on rough surfaces tend to have smaller sizes. The Ag NP size variation with the TF thickness is shown in Fig. 5.3(a) for particle formation on GaN, SiO_2 and SiN. The Ag TF thicknesses investigated were 5.0, 7.5, 10.0, 12.5 and 15.0 nm for all the surfaces. For every thickness, larger particle sizes are observed on GaN surface compared to the dielectric case. Below 10 nm Ag TF, the particle size variation is also smaller on the dielectric surfaces.

In parallel with the smaller particle sizes, the density of Ag NPs is higher on dielectric surface compared to bare GaN, as shown in Fig. 5.3(b). The density difference is most notable for small sized Ag NPs. This is a desirable feature in surface plasmonic applications using self-assembled NPs, as a larger number of metal NPs can participate in the LSP coupling and thereby have a larger potential for internal quantum efficiency (IQE) improvement. Naturally the density of NPs decreases with increasing size, however, the disadvantage of the self-assembly approach is the relatively large increase in the inter-particle spacing which significantly decreases the density with increasing size. As seen from the SEM images of large Ag NPs in the previous chapters, i.e. Fig. 3.14 and Fig. 4.1, a large percentage of the surface is not covered by metal NPs. The area coverage by the metal NPs on the surface is shown in the inset of Fig. 5.3(b), where it is seen to decrease on dielectric surfaces with increasing particle size. As demonstrated in the previous chapters, large NP sizes are required to obtain strong PL enhancement, and with this technique it is difficult to decrease the inter-particle spacing to achieve a higher density.

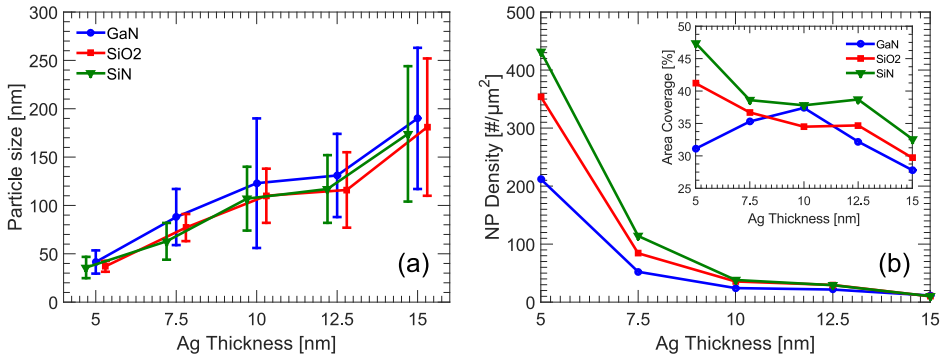

Figure 5.3: **(a)** Average Ag NP sizes on different surfaces by annealing Ag TF of various thickness. The error bars show the particle size variation. The Ag TF thicknesses (5.0, 7.5, 10.0, 12.5 and 15.0 nm) are equal for GaN, SiO_2 and SiN. The horizontal axis of the SiO_2 and SiN data are shifted by the +0.5 and −0.5 nm, respectively, for visual purposes. **(b)** The Ag NP density variation with Ag TF thickness, measured in number of particles per unit area. Inset shows the metal area coverage relative to the surface area.

Using transmittance measurements, the localized surface plasmon resonance (LSPR) locations of the Ag NPs from Fig. 5.3 can be determined. The resonance positions are shown in Fig. 5.4, where a red-shift is observed with increasing particle size for all the samples. When considering the LSPR of the GaN sample with 10 nm Ag TF RTA and the affiliated anomalous behaviour, the large spread in particle size seen in Fig. 5.3(a) should be kept in mind.

The refractive index of GaN is 2.43, while that of SiO_2 and SiN are 1.45 and 1.9, respectively. Hence Ag NPs formed on the lower index substrates are expected to display LSP modes with shorter resonance wavelength. This is indeed seen to be the case, where a blue-shift is noticed from GaN to SiN, and from SiN to SiO_2 surface for corresponding sizes. The usefulness of the blue-shift comes from the fact that the LSPR of large particles will shift closer to the typical emission wavelengths of green MQW light-emitters, and with respect to surface plasmonic coupling, this is a desired feature to enhance emitter IQE using particles with large scattering cross-section.

5.1.2 Coating dependent PL enhancement

The light-emitting GaN/InGaN MQW structures we have used do not have the optimal crystal quality that can be achieved, and as such pits and trenches exist on the surface as shown in Fig. 5.5(a). Pit defects are the result of threading dislocations originating from the QWs, which suggests the exposed nature of the

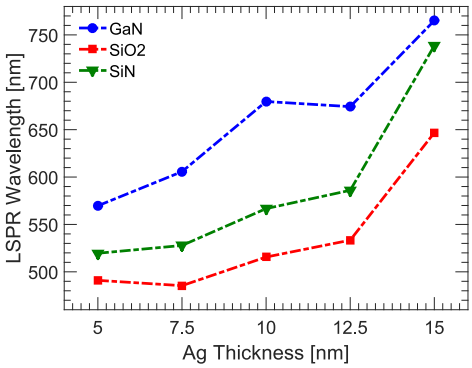

Figure 5.4: Wavelength positions of the main LSPR for Ag NPs on GaN and dielectric surfaces, determined by transmittance measurements.

active MQW region to air.[92–94] Trench defects are observable on our samples due to the thin capping layer on top of the InGaN QWs, which would otherwise have been buried by an overgrowth of thick (*p*-doped) GaN cap layer.[95,96] Trench defects can be traced to stacking faults during the epitaxial growth of the QWs.[96,97] By thermally annealing Ag TF on such a surface, small NPs are accumulated inside the defects, which is illustrated in Fig. 5.5(b,c) for small and large Ag NPs. With a thin Ag layer, more NPs are likely to diffuse inside the defects during the annealing process, compared to a thick layer as seen from annealing 8 nm and 16 nm Ag TF, where the pits in the latter mentioned are devoid of NPs.

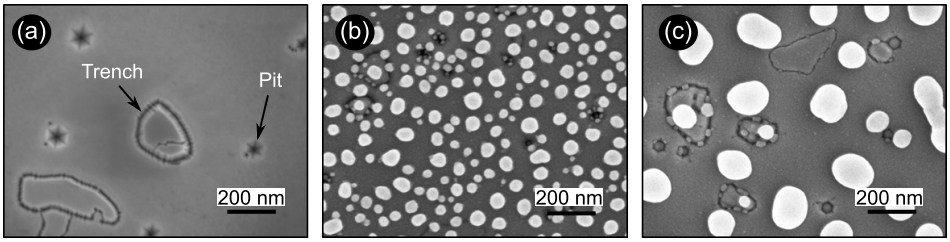

Figure 5.5: **(a)** SEM image of the top GaN surface of an GaN/InGaN MQW epitaxial structure revealing pit and trench defects. Self-assembled Ag NPs formed on the GaN surface after annealing **(b)** 8 nm and **(c)** 16 nm Ag TF.

Given that the QWs have exposed surfaces inside the pit and trench defects, surface states will exist at the interface which will degrade the luminescence efficiency due to surface recombinations. The surface recombination velocity can be reduced by using chemical treatments such as aqueous solutions of inorganic sulphides.[98,99] In our case, coating the MQW samples with SiN has shown to improve the integrated PL intensity by a factor of 2.3, and the peak-to-peak enhancement by a factor of 2.9. The PL spectrum after coating with 20 nm SiN (SiN-TF) is

shown in Fig. 5.6, where the emission is measured from the sapphire-side. Also shown in the figure is the result of 20 nm SiO_2 coating with a smaller PL enhancement (peak-to-peak around 1.4). We attribute this improvement to passivation of surface states by SiN. Although a flat SiN-TF cannot provide light extraction improvement with the given thickness, its rough surface from PECVD is expected to contribute to the improvement. The same argument can be applied for the PECVD SiO_2 layer, although the much lower PL improvement can be related to a poor passivation ability.

For surface plasmonic application we deposited 12 nm Ag TF on the samples with dielectric coating, followed by RTA process at 350 °C for 15 min in vacuum to obtain self-assembled Ag NPs. For comparison we also considered a sample without dielectric coating (i.e. as-grown sample), and deposited 15 nm Ag TF followed the same RTA process. The thicknesses were chosen according to the results obtained in Section 4.1 where the large Ag NPs had the strongest enhancement for the as-grown sample, while smaller sizes had the strongest enhancement when formed on a SiN coated GaN surface. The PL spectra after NP formation are shown in Fig. 5.6. It is seen that the SiN coating alone has improved the emission intensity more than Ag NP coating on as-grown GaN surface. The latter has an integrated PL enhancement (IPLE) factor of 1.9, while Ag NPs coating on SiO_2 and SiN surface show an enhancement factor of 2.6 and 3.0, respectively, relative to the corresponding PL with dielectric coating. As such, the total enhancement factor relative to the as-grown sample is 3.7 and 6.7 for Ag NP on SiO_2 and SiN, respectively.

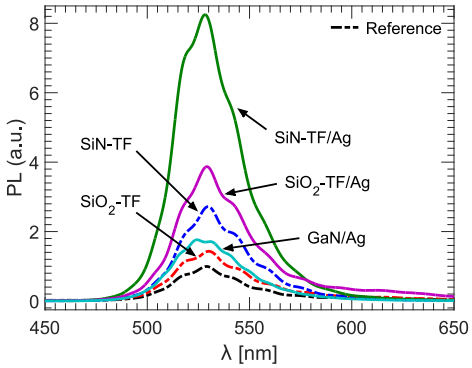

Figure 5.6: Measured PL spectra showing the effects of dielectric coating (SiN-TF and SiO_2-TF) and the inclusion of Ag NPs on top (SiN-TF/Ag and SiO_2/Ag), using a 12 nm Ag TF RTA. PL spectra from Ag NPs on GaN surface without dielectric is shown for comparison (GaN/Ag). All the spectra are normalized to the peak value of the as-grown reference.

Considering the result of Ag NPs on as-grown sample (GaN/Ag), the surface plasmonic enhancement is seen be lower than what was obtained in an earlier trial (Fig. 4.3), where 15 nm Ag TF was used. The IPLE in the previous investigation was a factor of 2.4, compared to the factor of 1.9 in the current investigation. In contrast, even though the SiN is 20 nm thick in this case, the enhancement with Ag NPs on SiN is larger than before (with 10 nm Ag TF annealed on 15 nm SiN). However, this can be explained by the particle size difference.

The resulting enhancements due to SiO_2 and SiN TF coatings relative to the as-grown sample are shown as PL ratios in Fig. 5.7(a). With SiN coating the enhancement peak is found around 518 nm, and localized near the emission wavelength, in contrast to SiO_2 coating which has a weak enhancement peak at 564 nm.

The PL ratios for the Ag NP coated samples are taken relative to the emission without Ag NPs, i.e. the PL intensity with Ag NPs on SiN-TF is compared to the emission from the sample with SiN-TF coating alone. The spectral shape of the PL ratio for GaN/Ag is also different compared to the previous investigation, which can be related to its different transmittance spectrum shown in Fig. 5.7(b) where a clear absorption dip is located around 760 nm. Two PL enhancement peaks exist for this sample, with one at 632 nm and a second apparent peak at 510 nm, where the largest peak at 632 nm has a value of 3.0. Considering SiO_2-TF/Ag sample, the enhancement from Ag NPs, shows a noticeable peak around 549 nm with a PL ratio factor of 2.8, while another peak can be observed near 638 nm. The strongest enhancement due to Ag NPs, is observed with SiN-TF/Ag, where its PL ratio is the highest amongst the different samples throughout the considered spectral range. The peak value of the PL ratio is 3.4 and located

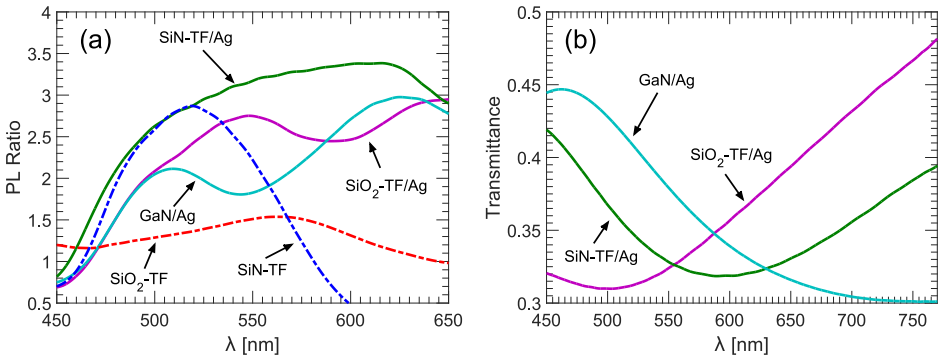

Figure 5.7: **(a)** PL ratios showing the effect of dielectric TF coating relative to the as-grown sample (dashed lines), and the effect of Ag NP coating, from 12 nm Ag TF, relative to the respective surfaces prior to Ag NP coating (solid lines). **(b)** The transmittance spectra for Ag NPs with similar sizes on different substrates.

around 605 nm wavelength, though it is difficult to label it as a well-defined peak. The enhancement values are summarized in Table 5.1.

It is not straightforward to explain the second peak at 638 nm of the PL ratio for SiO_2-TF/Ag, though it should be noted that all the PL ratios due to Ag NPs are approaching a value of approximately 2.9 at 650 nm wavelength as seen in Fig. 5.7(a), and from around 640 nm all the ratios decrease with increasing wavelength. From a theoretical point of view, the main peak is expected to blue-shift when the SiO_2 dielectric intermediate layer is introduced between Ag NPs and the GaN surface, if the enhancements are due to LSP-QW coupling. This was explained in the previous chapter, and will be further discussed later in this chapter. However, due to the limited band-width of the emission spectrum, it is not possible to observe enhancements at longer wavelengths than 650 nm, which would have been useful for the GaN/Ag sample due to its LSPR being located at around 760 nm.

Assuming the main peak of the SiO_2-TF/Ag sample is the one located at 549 nm, the peak enhancement is then seen to blue-shift when the substrate for Ag NPs goes from GaN to SiN, and from SiN to SiO_2. This trend appears to be consistent with the transmittance dips seen in Fig. 5.7(b). As theoretically expected, the lower the refractive index is, the more the dip blue-shifts, i.e. from 632 nm, 605 nm to 549 nm for GaN, SiN and SiO_2, respectively. As before, we attribute these dips to the collective resonances from LSP modes of the Ag NPs. For the SiN-TF/Ag sample, the peak enhancement location does appear close to the 586 nm LSPR wavelength. With SiO_2, the main enhancement peak is red-shifted by 47 nm relative to the LSPR wavelength. Without dielectric, the PL ratio is seen to increase at long wavelengths and apparently approaching a peak value around 632 nm. Though it might have been expected that this peak would have been located at a longer wavelength had the emission band-width been broader, since the LSPR is located around 760 nm.

Nonetheless, the complex light-emitting structure of the samples should be emphasized, where 5 QWs contribute to the emission, and furthermore have unequal InN molar fraction due to uncontrolled variations during the epitaxial growth of each QW layer. In principle, this means that the emission wavelengths from each

Table 5.1: Summary of enhancements parameters due to dielectric TF coating, and Ag NPs formed by annealing a 12 nm Ag TF.

Coating	Ag NP IPLE	Total IPLE	PL ratio peak values	PL ratio λ_{peak} [nm]	LSPR peak λ_{LSP} [nm]
SiO_2-TF	-	1.40	1.5	564	-
SiN-TF	-	2.27	2.9	518	-
GaN/Ag	1.94	1.94	3.0; 2.1	632; 510	760
SiO_2-TF/Ag	2.61	3.66	2.9; 2.8	638; 549	502
SiN-TF/Ag	2.97	6.74	3.4	615	586

of the QWs are different, but in combination constitute the measured emission spectrum. In addition, it is expected that only one or two of the top-most QWs which will experience a strong interaction with LSP modes and have the possibility of IQE enhancement. It is therefore difficult to observe notable features from LSP-QW coupling in the spectrum of the PL ratios and correlate with the LSP mode resonances based on the transmittance dips.

5.1.3 Ag nanoparticle size dependence

Above we considered the effects of Ag NPs from a 12 nm Ag TF formed on as-grown MQW samples and with dielectric TF coating. We will focus our attention on the dielectric TF coated samples and investigate the PL intensity with Ag NP size variation which is achieved by annealing five different Ag TF thicknesses as shown in Fig. 5.8. This is done for SiO_2 and SiN coatings with the equal layer thickness, i.e. 20 nm as before.

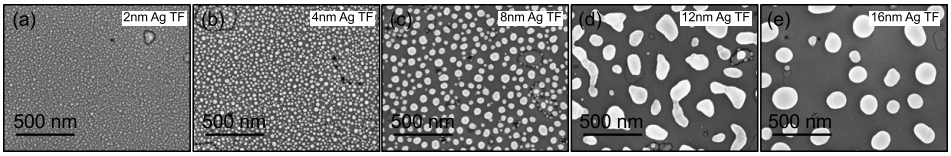

Figure 5.8: Formation of Ag NPs on GaN/SiN-TF surface by thermally annealing 2-16 nm Ag TF.

The transmittance spectra in Fig. 5.9(a) reveal the positions of LSP mode resonances with Ag NPs on SiN-TF, where the LSPR is seen to blue-shift with decreasing particle size except for the 2 nm Ag. The decrease in transmittance for the 16 nm Ag from around 450 nm indicate the existence of higher-order LSP modes below 400 nm wavelength.[72] The 12 nm Ag LSPR appears to be the closest to the MQW emission. It has also the broadest inhomogeneous spreading due to particle size variation and thereby provide a better overlap with the emission wavelength compared to the other size distributions. The LSPR wavelengths for the various Ag NP sizes on dielectric coated MQW samples are shown in Fig. 5.9(b), where large sized NPs on SiO_2-TF surface have the best spectral overlap with the MQW emission spectrum.

Sapphire-side PL intensity spectra after Ag NP formation on SiO_2 and SiN TF coating of the MQW samples are shown in Fig. 5.10. The spectra are compared to the PL intensity of the dielectric coated MQW samples without Ag NPs. Considering the SiO_2 coated sample, the PL intensity is quenched by NPs formed from 2, 4 and 8 nm Ag, and the quenching is larger the smaller the NP size is. On the other hand, the 12 nm Ag results in a higher enhancement than the 16 nm Ag, where the IPLE due to Ag NPs for 12 nm and 16 nm case is 2.61 and 1.57, respectively. With SiN coating, no PL quenching is observed for the small sized

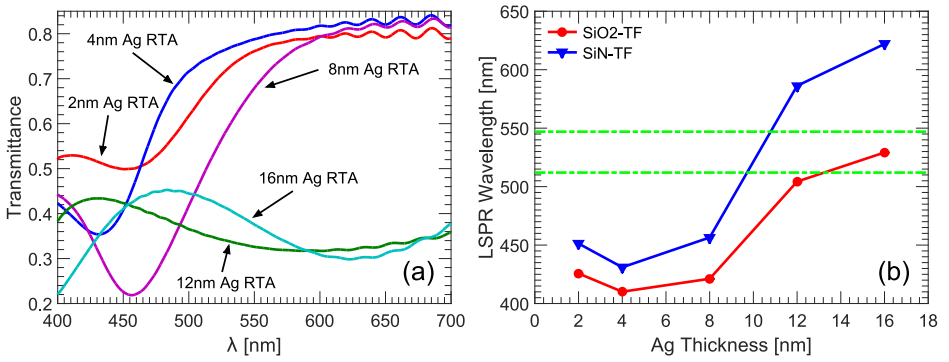

Figure 5.9: **(a)** Transmittance spectra for various sizes of Ag NPs on GaN/SiN-TF samples, measured from the sapphire to GaN side. **(b)** The LSPR locations with Ag NPs on SiO_2-TF and SiN-TF. The horizontal dashed-lines show the MQW emission band.

NPs, and the 8 nm Ag has in this case resulted in a PL enhancement comparable to that from 16 nm Ag as seen in Fig. 5.10(b). The IPLE due to 8 nm Ag and 16 nm Ag TF annealing on SiN-TF is 1.61 and 1.80, respectively, and the 12 nm Ag sample is the aforementioned from Fig. 5.6, with IPLE of 2.97.

Despite there being a better spectral overlap between the MQW emission spectrum and the LSP modes of large sized Ag NPs on SiO_2-TF (see Fig. 5.9(b)),

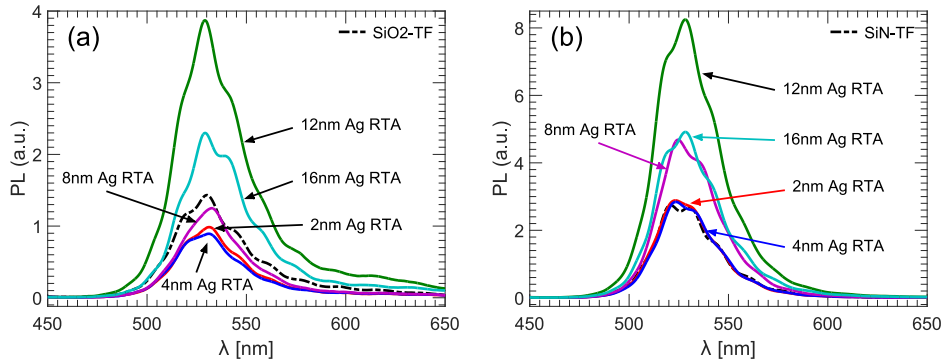

Figure 5.10: Measured PL spectra from the sapphire-side for various sized Ag NPs on **(a)** SiO_2-TF and **(b)** SiN-TF coated MQW samples. All spectra are normalized to the PL intensity peak of the as-grown sample (not shown). The emissions with only dielectric coating also shown (black dashed-lines).

the enhancement is higher with the SiN-TF. From the dielectric coatings alone, we saw that SiN resulted in a higher PL enhancement compared to SiO_2, which we could mainly attribute to a better passivation using SiN. The non-existent PL quenching with Ag NPs on SiN coating was earlier attributed to an improved scattering (using the scattering-to-extinction ratio (SER) figure of merit). This study reveals, however, that the passivation aspects of SiN also might have a role in eliminating PL quenching in addition to the improved SER, since by considering Ag NPs on SiO_2-TF, PL quenching is still observed to some degree. In addition to the strong absorption of small Ag NPs, surface states due to NPs inside trench and pit defects are also expected to quench the PL.

When measuring the PL intensity from the top GaN-side, using the same sapphire-side excitation conditions, a different trend is observed. The GaN-side emission spectra are shown in Fig. 5.11. In this case the strongest emission is observed from the 16 nm Ag samples for both SiO_2 and SiN coating, with an IPLE by a factor of 8.43 and 10.9, respectively. The IPLE factor for the 12 nm Ag with SiO_2 and SiN coating is 1.68 and 2.13, respectively. The SiN-TF with the 8 nm Ag no longer shows an enhancement, and is barely affecting the PL intensity as seen from the inset of Fig. 5.11(b). The remaining smaller sizes show a similar behaviour to that from sapphire-side emission.

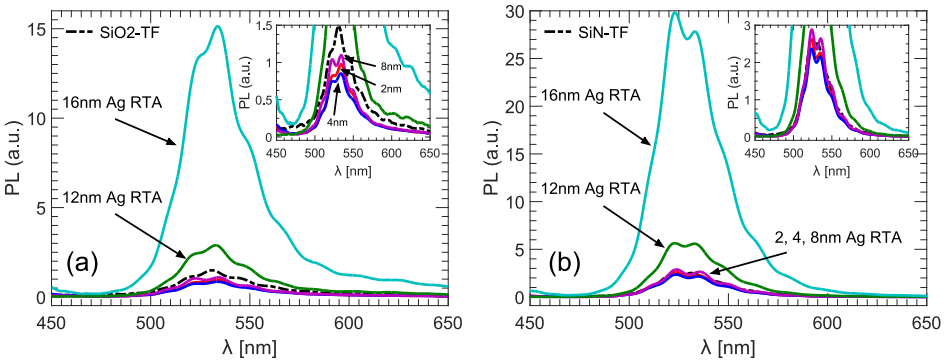

Figure 5.11: Measured PL spectra from the GaN-side on **(a)** SiO_2-TF and **(b)** SiN-TF coated MQW samples. The black-dashed lines are the emissions with only dielectric coating, and the spectra are normalized to the as-grown emission peak (not shown). Insets show a zoomed view.

To better understand the observed difference between sapphire- and GaN-side emissions, we consider the PL ratios for the SiN-TF samples, where the ratios are taken relative to the SiN-TF coated MQW emission. The PL ratios from sapphire-side emissions are shown in Fig. 5.12(a), where it is seen that both the 12 nm and 16 nm Ag have large enhancements at wavelengths longer than the peak emission wavelength, with peak ratios at 615 nm and 626 nm, respectively. The apparent

peak of the 16 nm Ag is more likely related to the decreasing feature in the PL ratio from around 640 nm as observed in all the samples due to weak emission intensity. Nonetheless the 12 nm Ag sample shows a larger PL ratio closer to the emission peak and thereby a blue-shifted PL ratio center-of-mass (CM) relative to the 16 nm Ag. The PL ratio peak of the 8 nm Ag sample is located at 539 nm. The blue-shift of the sapphire-side PL ratio CM appear consistent with the blue-shift of the LSPR wavelengths.

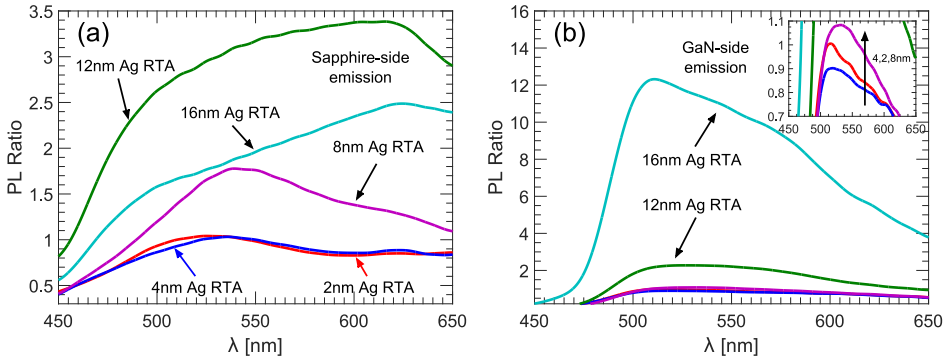

Figure 5.12: PL ratio spectra for the SiN-TF coated MQW samples with various sized Ag NPs, relative to the SiN-TF coated MQW emission without Ag NPs. The PL intensity is recorded from **(a)** sapphire-side and **(b)** GaN-side. The excitation in both cases is from sapphire-side. Inset shows zoomed view PL ratio for small sized NPs.

The PL ratios due to GaN-side emissions are shown in Fig. 5.12(b). We notice from the spectra, that the PL ratio peaks are significantly blue-shifted compared to the case of sapphire-side emission. These enhancements are related to the LSP-QW coupling due to the Ag NPs in the near-field of the QW emitters. As discussed in the previous chapter, the LSP modes can be divided in two categories; a metal-substrate mode and a metal-air mode, denoting which interface the electric field intensity is confined to. The metal-air mode will always be blue-shifted relative to the metal-substrate mode due to the air refractive index, and will red-shift with increasing particle size similar to the metal-substrate mode (see Fig. 4.4(b)). By these considerations, the emission from the sapphire-side is expected to have the contributions from the metal-substrate LSP mode, while the GaN-side emission from the metal-air LSP mode radiating in the up-ward direction, where the latter is blue-shifted relative to the former.

Using the same simulation formalism of Chapter 4 we investigate the light scattered into air (σ_{air}) and into the substrate (σ_{sub}) from the NP on GaN/SiN-TF substrate, and consider the quantities, SER_{air} and SER_{sub}, calculated relative to the total extinction cross-section σ_{ext}. To also take into account the intensity enhancement at the plane of the QWs we consider the product between SER

and $|E|^2$ enhancement spectra. This quantity is shown for the substrate-side in Fig. 5.13(a). The observed peak is from the metal-substrate LSP mode and is seen to red-shift with increasing size NP size. At the 530 nm emission wavelength the product is seen to decrease for large sized Ag NPs. Considering the air-side scattering component in Fig. 5.13(b), the product reveals another peak located at shorter wavelengths which is the attribute of metal-air LSP mode and is also seen to red-shift with increase particle size. For the air-side scattering, however, the product is seen to increase with particle size.

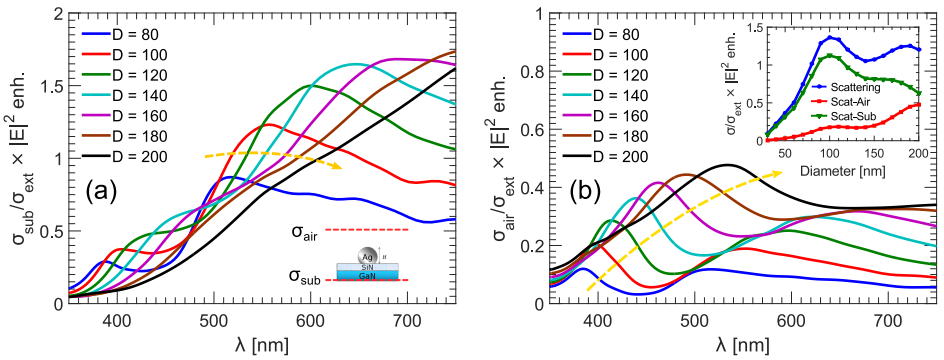

Figure 5.13: The product between the SER and intensity-enhancement spectra for the **(a)** substrate-side, and **(b)** air-side detection. Arrows indicate the direction of increasing diameter, D. The inset shows the variation of the parameters with Ag NP diameter at 530 nm wavelength.

These simulations capture the trends observed from the sapphire- and GaN-side PL measurements, where the highest enhancement from sapphire-side is not observed by the largest particle sizes but rather from the particle of 12 nm Ag. The inset of Fig. 5.13(b) shows that the product of SER and intensity-enhancement for the scattering component into the substrate has an optimum value around $D = 100$ nm after which it decreases with D. At the same time, the scattering component into air increases with the particle size. The latter explains how the highest PL enhancement measurement from GaN-side emission is observed for the largest particles from 16 nm Ag. Additionally, the metal-air LSP mode has a better spectral overlap with the MQW emission spectrum compared to the metal-substrate mode for large NP sizes which can explain the larger enhancement obtained from the GaN-side compared to the sapphire-side emission in the case of large NPs from 16 nm Ag.

Another contribution, however, could be light extraction efficiency (LEE) enhancement from the NP, i.e. through LSP-TIR coupling. Nonetheless, it is difficult to explain the large PL intensity observed from the GaN-side with Ag NPs com-

pared to the sapphire-side emission. The integrated enhancements due to Ag NP coating on SiO_2-TF and SiN-TF are summarized in Fig. 5.14 for both sapphire-side and GaN-side emission.

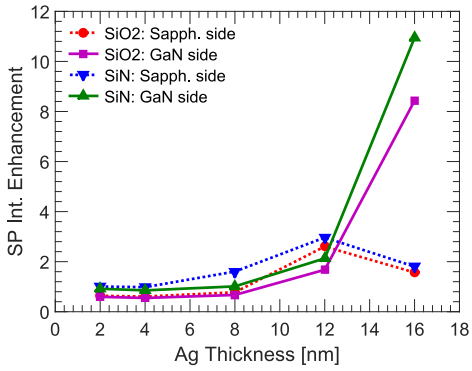

Figure 5.14: The IPLE factor due to Ag NPs from sapphire-side (dashed lines) and GaN-side emission (solid lines). Both SiO_2-TF and SiN-TF coated MQW samples are considered.

5.1.4 Conclusions

For the epitaxial wafers considered in this section, thin dielectric coatings have shown to enhance the emission. We could attribute this enhancement to the passivation aspect of the dielectrics, due to the existence of pit and trench defects on the samples. In this regard, SiN had a better performance than SiO_2 coating. In Section 6.2 we will see that SiN coating of nano-structures where the active region is exposed to air, has a similar effect of emission improvement.

Additionally, Ag NPs formed on the dielectric coated GaN surface, showed a higher improvement compared to the as-grown surface, despite there being a larger separation between the NPs and the QWs due to the inclusion of the dielectric intermediate layer. With the dielectric coatings, the Ag NPs also resulted in PL enhancement for the GaN-side emission, which was not observed without the dielectrics.

With particle size variations it was seen that although the largest sizes of NPs considered gave the highest enhancement from GaN-side emission, it did not yield the highest enhancement for the sapphire-side emission. This could be explained as being due to the difference between the metal-air and metal-substrate LSP modes, where the former mainly contributes to the GaN-side emission, while the latter to the sapphire-side emission

5.2 Nano-patterned dielectric

Large metal nanoparticles have the desirable scattering properties to enhance the emission of QW emitters in their near-field, but suffer from having a poor spectral overlap between their LSP mode resonance and the QW emission spectrum for green wavelengths. Dielectric coatings with a lower refractive index than GaN were applied to blue-shift the LSPR wavelengths towards the emission wavelength, though in the case of SiN dielectric, the wavelength shifts were not enough to overlap with the emission spectrum. To further blue-shift the peak LSPR location, dielectrics of a lower refractive index is needed. We will in this section investigate a method to reduce the effective refractive index of dielectrics on GaN surface, and thereby achieve a further blue-shift of the LSPR of Ag NPs on such a dielectric.

5.2.1 Low-index optical coatings

Amongst conventional optical films, SiO_2 has one of the lowest refractive indices. By using oblique angle deposition of SiO_2 with e-beam evaporation, thin nano-rods (NRs) of SiO_2 can be grown through the effect of self-shadowing. Such an optical film was grown by Xi *et al.*, which showed an effective refractive index of 1.08.[100] Later on this technique was exploited to grow anti-reflection coatings to enhance UV-LED efficiency, and Yan *et al.* showed that by coating the polished sapphire surface with a double layered SiO_2 NRs, the LEE could be enhanced by 8 %.[101] In general, patterned dielectric coatings have been employed to enhance the LEE of LEDs, an example of which is the fabrication of SiN nano-structures on the ITO current spreading layer. Byeon *et al.* demonstrated a 19 % EL enhancement by fabricating SiN photonic crystral (PhC) structure on ITO using nano-imprint.[102] A cost-effective method of producing random SiN nano-structures on ITO was demonstrated by Shei *et al.* who showed an output power increase by 15 %.[103] However, the latter mentioned approach did not provide a uniform nano-structure height.

These methods have two useful aspects for our surface plasmonic applications. The first is the possibility of obtaining a low index TF coating on which Ag NPs would have a blue-shifted LSPR compared to an un-coated GaN surface. The second aspect is the enhancement of LEE from the nano-structured dielectric. For our purpose, obtaining a patterned dielectric coating with a uniform surface and low refractive index is desired, and to achieve this, we will in the following investigate a cost-effective method capable of producing densely spaced nano-structures of equal height.

5.2.2 Fabrication of dielectric nano-rods

We will take advantage of the same PECVD dielectrics as considered before, i.e. SiO_2 and SiN, to fabricate a nano-patterned coating on the GaN surface of MQW

emitters. To form NR structures on the dielectric coating, we use an RIE process with self-assembled Au NPs as mask to etch the dielectric. The process flow is illustrated in Fig. 5.15. In the first step a dielectric thickness of 20 nm is deposited using PECVD, followed by the deposition of 1.5 nm Au TF using e-beam evaporation. Self-assembled Au NPs are formed through an RTA process of Au TF at 650 °C for 5 min. The formed NPs have an average size of 11 nm with a 3 nm of standard deviation, and the surface area coverage is 32 %.

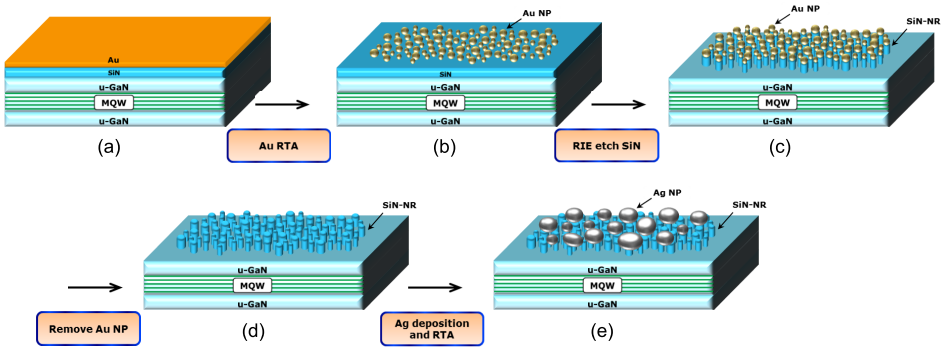

Figure 5.15: Process flow overview on fabrication of dielectric NR structures using Au NPs as etch mask, and formation of Ag NPs on top.

Using Au NPs as mask, the 20 nm SiO_2 and SiN layer were etched using an RIE process with CHF_3/N_2 chemistry, where the flowrates were 8/43 sccm, under a chamber pressure of 38 mTorr and an RF power of 50 W. The etch rate for SiO_2 was between 32-40 nm/min, while SiN had an etch rate between 36-45 nm/min. Although GaN is not etched in this process, the RIE could still damage the active light-emitting region by degrading the IQE, and should therefore be kept to a minimum duration, enough to only etch through the dielectric layer.

After the RIE, an aqua regia solution of 3:1 HCl:HNO_3 was used to etch away the Au NPs on the surface without affecting the dielectric NR-pattern. The etched dielectric structures are shown in Fig. 5.16(a,b). Deposition of Ag TF followed by a thermal annealing process results in the formation of Ag NPs as shown in Fig. 5.16(c,d), where it is seen from the cross-section that the NPs are formed on the top surface of the NR-coating. The annealing condition is similar to that used before, i.e. an RTA at 350 °C for 15 min in vacuum. Formation of Ag NPs inside the trench and pit defects is also visible in Fig. 5.16(c). The example shown is the result of a 12 nm Ag TF annealing on SiN-NR coating.

As mentioned, the RIE process has a critical effect on the active region. This is illustrated by the PL results in Fig. 5.17(a), where the sapphire-side emission is measured for samples with SiO_2-NR structure obtained by three different RIE time durations. Given the SiO_2 etch rates, the 15 and 26 sec RIE is expected to give NR heights of 8-10 nm and 14-17 nm, respectively. With a duration of 38 sec

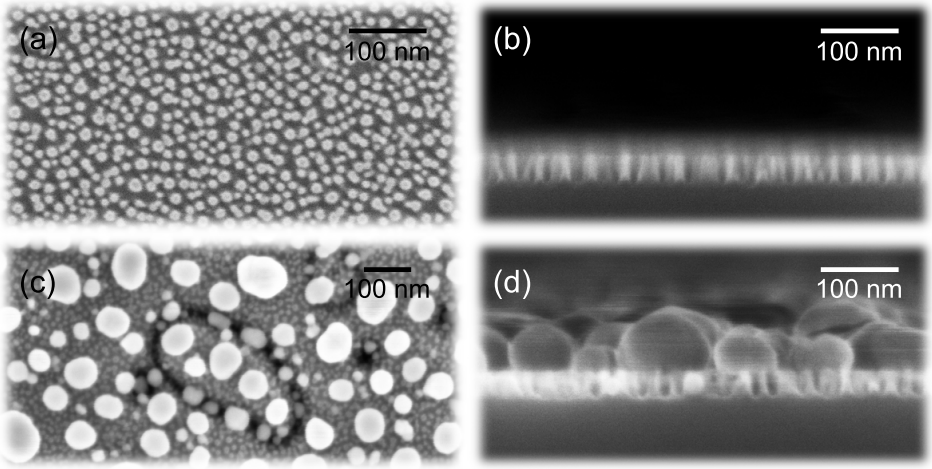

Figure 5.16: **(a)** Top and **(b)** cross-sectional view of the dielectric NR-pattern after removing Au NPs. **(c)** Top and **(d)** cross-sectional view of Ag NP formation on SiN-NR structures after annealing a 12 nm Ag TF.

the exposed areas of the 20 nm SiO_2 is completely etched, as the expected etch depth is 20-25 nm. The first thing to notice is the improved PL intensity when NR-pattern is formed on SiO_2, compared to bare SiO_2-TF coating. With 15 sec etch, the pattern results in an IPLE by a factor of 2.1 relative to the SiO_2-TF coating. Increasing the RIE duration to increase the NR height is seen to degrade the PL intensity. This can be attributed to RIE-induced damage to the active region due to ion-bombardment of the surface.[49,50,104]

5.2.2.1 PL characterizations

Given a certain dielectric thickness, for surface plasmonic applications we require large NR heights to reduce the effective refractive index as much as possible. We therefore etch NR-patterns with an approximate height of 15 nm from a 20 nm dielectric TF thickness, which for SiO_2 implies an RIE duration of 26 sec. This implies a large RIE-induced damage which has to be accounted for. It has been shown that plasma-induced damage can be recovered through thermal annealing,[104] and as such, we investigated the effects of thermal annealing after the RIE process. The annealing conditions were identical to that used for Ag NP formation (i.e. at 350 °C), and the result of annealing is shown in Fig. 5.17(b). The RTA process is seen to significantly improve the PL intensity, where the IPLE factor relative to the SiO_2-TF coating is increased from 1.5 to 3.2.

The PL intensity from SiO_2-NR and SiN-NR coating on GaN after thermal

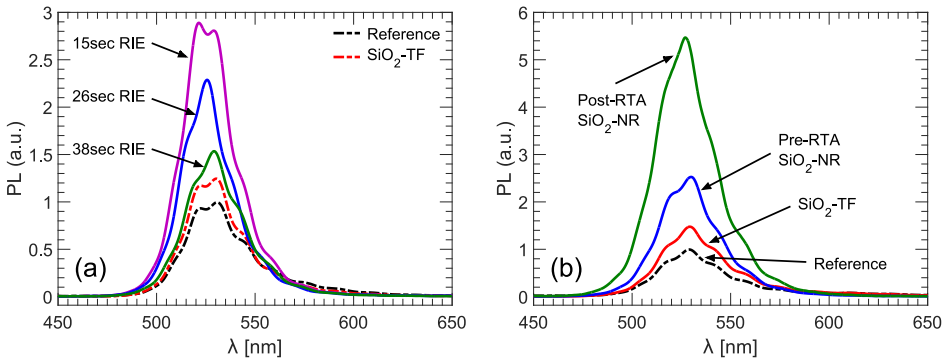

Figure 5.17: **(a)** Measured PL spectra showing the effects of RIE process on the MQW emission. Also shown is the as-grown emission spectrum (dashed black line), and the emission after SiO_2-TF coating (dashed red line). **(b)** PL spectra showing the effects of RIE-induced damage curing by thermal annealing for the SiO_2-NR structures.

treatment is shown in Fig. 5.18. All coatings (TF and NR) have a thickness of 20 nm, and the height of the NRs is approximately 15 nm on both SiO_2 and SiN. The NR coatings show a strong PL intensity enhancement, nearly irrespective of the dielectric. With SiN-NR pattern the IPLE relative to the as-grown sample is a factor of 4.7, while for SiO_2-NR a factor of 4.3 is obtained. These enhancements are attributed to an improved LEE from both sapphire- and GaN-side, as they are observed from both sides (IPLE by a factor of 4.0 from GaN-side emission for both SiO_2 and SiN).

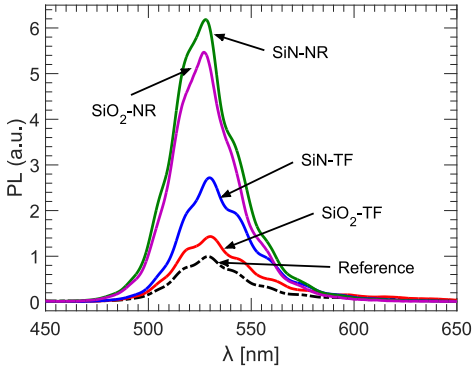

Figure 5.18: PL spectra from sapphire-side emission, comparing the effects between SiO_2-NR and SiN-NR coating on MQW emission.

5.2.2.2 Properties of Ag nanoparticles on patterned dielectric

With LEE improved through a thin dielectric coating, the possibility of employing plasmonic metals in the near-field of the QW emitters to improve the IQE, remains open. Self-assembled Ag NP formation was already demonstrated on dielectric NR-pattern as shown in Fig. 5.16(c,d), which will once again be exploited for LSP-QW coupling combined with the dielectric coating. As shown in the last section, the size of Ag NPs depended on the surface conditions, where the rough surface of PECVD dielectric gave a smaller average NP size compared to the higher quality GaN surface. This is also seen to be the case with dielectric NR-pattern, where the average NP size is even smaller than on the as-deposited (TF) dielectric.

We investigated five different sizes of NP by annealing Ag TF of 4, 8, 12, 16 and 20 nm on SiO_2-NR and SiN-NR coatings, and the result (for SiN-NR) is shown in Fig. 5.19. We estimated that to obtain NPs of similar sizes on both TF and NR dielectric coatings a difference of approximately 4 nm was needed for the Ag TF deposition; hence the reason behind choosing the given dimensions for NR coated samples. The particle distributions of Fig. 5.19 should be compared with those of Fig. 5.8.

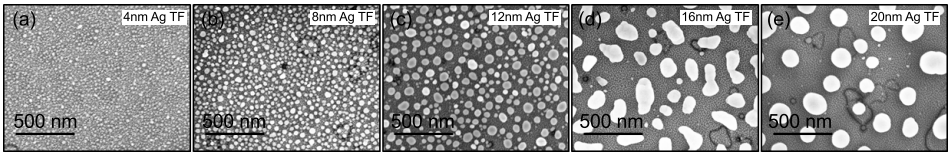

Figure 5.19: Formation of Ag NPs on GaN/SiN-NR surface by thermally annealing 4-20 nm Ag TF.

The NP density for equivalent sizes is, however, comparable when considered on TF and NR surfaces as shown in Fig. 5.20. Also shown in the figure is the average NP size for given Ag TF thickness, where the approximate 4 nm of difference is seen to produce NPs of similar sizes on both dielectric TF and NR coatings. Although a large NP density is desired to have a strong LSP-QW coupling, it is not obtained on the NR coating. Nevertheless, it makes comparisons with Ag NPs on dielectric TF coating justifiable.

The LSP mode resonances on dielectric NR-pattern are analysed through the transmittance spectra and in Fig. 5.21(a) the comparison is made between Ag NPs on dielectric TF and NR coating as well as on GaN. Similar sizes of NPs are considered, i.e. the Ag TF thickness on GaN, dielectric TF and NR is 15, 12, and 16 nm, respectively. It is difficult to observe a clear resonance feature in the spectra for the NR coatings, though a weak feature is visible at approximately 450 nm for SiO_2-NR and more pronounced one at 465 nm for SiN-NR. Nonetheless, it is apparent that the LSPR wavelengths are significantly blue-shifted when the NPs are formed on NR-structures.

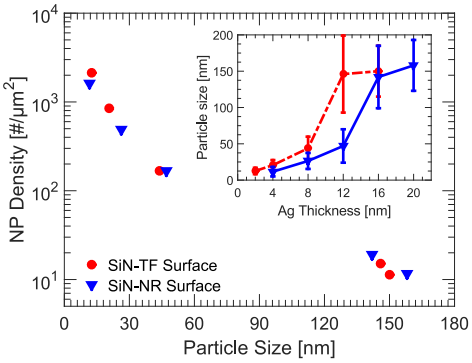

Figure 5.20: The Ag NP density variation with average NP size for SiN-TF and SiN-NR surfaces. The inset shows the average NP size variation with Ag TF thickness.

By considering the transmittance spectra with varying NP size on SiN-NR coating sample as shown in Fig. 5.21(b), it becomes clear that the LSPR from 16 nm and 20 nm Ag RTA extends over a broad range of wavelengths, covering the MQW emission. The LSPR wavelengths of 4-12 nm Ag RTA appear to be located around 400 nm and below.

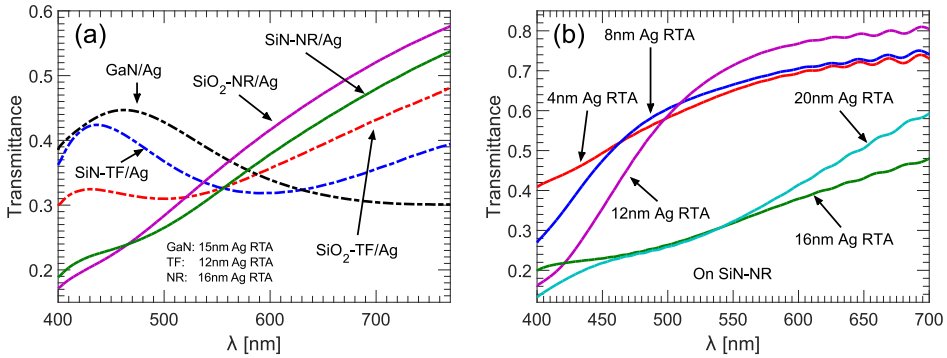

Figure 5.21: **(a)** Transmittance spectra from sapphire to GaN-side, with Ag NPs on the surface. Ag TF thickness was 15 nm on GaN, and 12 nm on SiO_2-TF and SiN-TF, while it was 16 nm on SiO_2-NR and SiN-NR. **(b)** Transmittance for various sized Ag NPs on SiN-NR coating.

5.2.3 Applying surface plasmonics

5.2.3.1 Coating dependence

Having characterized the LSPR of similar sized Ag NPs on different coating types through transmittance measurements, we now investigate the PL measured from the sapphire-side of the MQW samples. The PL spectra of the samples with Ag NPs on GaN and different dielectric coatings are shown in Fig. 5.22. Dielectric NR-structures combined with Ag NPs are indeed seen to have the largest PL intensities, with SiN-NR providing the best enhancement relative to the as-grown reference sample. The IPLE factor relative to the as-grown emission is 13.7 and 11.4 for Ag NPs on SiN-NR and SiO_2-NR coatings, respectively.

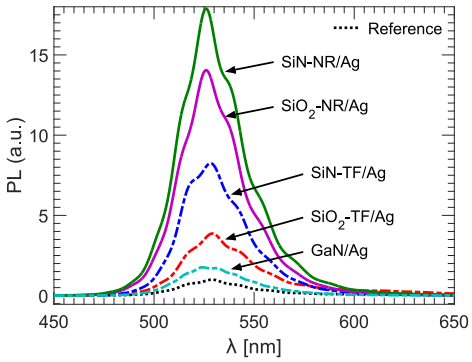

Figure 5.22: Measured PL spectra of the sapphire-side emission after forming Ag NPs on various dielectric coating types. NPs are formed by annealing 15 nm (on GaN), 12 nm (on dielectric TF) and 16 nm Ag TF (on dielectric NR). The as-grown sample emission is shown as the reference point.

The large enhancements observed are from the combined effects of LEE improvement due to surface patterning, and the SP-induced enhancement due to LSP-QW coupling with Ag NPs. To analyse the effects due to Ag NP coating, we consider the PL ratios between the emission with and without Ag NPs on dielectric coated samples. The PL ratio spectra for sapphire-side emission are shown in Fig. 5.23(a), where the previously considered Ag NP coating on bare dielectric surface (SiO_2-TF and SiN-TF) is also shown for comparison. It is seen that around the MQW emission wavelength, the enhancement due to Ag NPs on dielectric NR is not higher than that obtained with dielectric TF. The PL ratio for the NR samples only exceeds the TF case at wavelengths above 550 nm. The PL ratio peak for SiO_2-NR and SiN-NR appear at 587 and 610 nm, respectively. The dip feature in the ratio appear around 510 nm for both dielectric NR coatings.

For the emission from GaN-side, the NR coated samples clearly show a larger enhancement due to Ag NPs as shown in Fig. 5.23(b). Ag NPs on as-grown GaN

surface do not show improvement for the GaN-side emission. Nonetheless, the NR coatings improve the IPLE factor from 1.68 to 3.07, and 2.13 to 3.04 when going from TF to NR coatings of SiO_2 and SiN, respectively. The GaN-side PL ratio once again reveal a blue-shift of the CM relative to the sapphire-side emission. The integrated enhancement parameters for the different dielectric coating types with Ag NPs relative to the as-grown emission are summarized in Table 5.2.

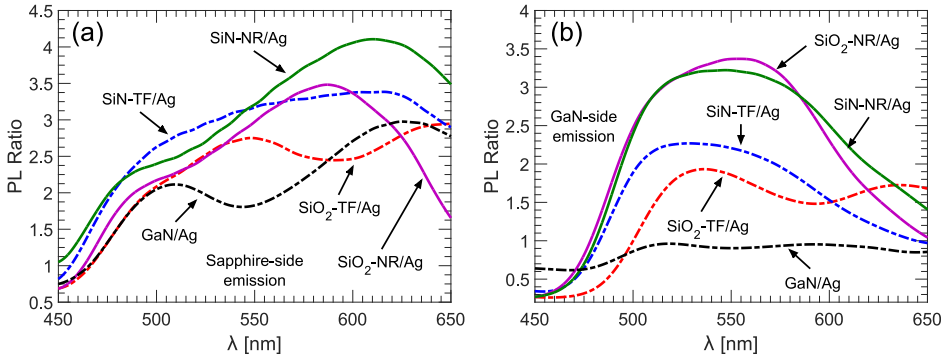

Figure 5.23: PL ratios showing the effects of Ag NP coating on the emission spectra for **(a)** sapphire-side and **(b)** GaN-side emission. Pre-annealed Ag TF thickness was 15 nm on GaN, 12 nm on SiO_2-TF and SiN-TF, and 16 nm on SiO_2-NR and SiN-NR.

The angular dependence of the total integrated enhancement from both Ag NPs and the dielectric coatings are illustrated in Fig. 5.24, where the angle resolved integrated PL intensities also are shown. The enhancement is seen to decrease for oblique emission angles, with the highest enhancement being attained for normal emission.

Table 5.2: Enhancements relative to the as-grown sample emission.

IPLE	Sapphire-side		GaN-side	
Coating	Bare dielectric	w/ Ag NPs	Bare dielectric	w/ Ag NPs
SiO_2-TF	1.40	3.66	1.41	2.40
SiN-TF	2.27	6.74	1.85	3.97
SiO_2-NR	4.31	11.4	4.04	12.3
SiN-NR	4.68	13.7	4.00	12.0

5.2.3.2 Scattering and enhancement properties

From the PL measurements it was seen that with SiN-TF and SiN-NR coatings the enhancements due to Ag NPs were not significantly different when considered

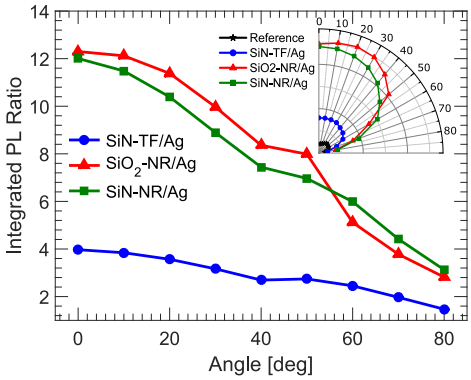

Figure 5.24: Angular emission enhancement of dielectric coated samples with Ag NPs based on the integrated PL intensity from GaN-side emission. Inset shows the emission pattern.

from the sapphire-side. A more pronounced difference was observed from the GaN-side emission (Fig. 5.23). To get an understanding of this behaviour we once again consider the product between the SER and intensity-enhancement for substrate- and air-side scattering. Regarding the simulation of Ag NP on SiN-NR coating, the random distribution of NRs is extracted from the SEM image for the NRs, i.e. from Fig. 5.16(a). This is used in the 3D FDTD simulations of the scattering and absorption cross-sections, as well as intensity ($|E|^2$) enhancement at the plane of the top QW, where the total dielectric height is 20 nm, while the height of the NR is 15 nm.

Fig. 5.25(a) shows the SER-intensity-enhancement product for the substrate-side scattering of an Ag NP with 140 nm diameter. The spectrum for the GaN/Ag system resembles the corresponding PL ratio spectrum seen in Fig. 5.23(a), although its strength is comparable to, and even exceeds, that of the SiN-TF and SiN-NR cases. This is expected due to the smaller distance between the QW plane and the Ag NPs, compared to having a dielectric intermediate layer. The simulations, however, do not capture the difference in the PL ratios between Ag NPs on GaN and GaN/SiN. It is difficult to give a conclusive answer on how Ag NPs on SiN (with increased distance to the QWs), can provide a larger enhancement compared to Ag NPs on bare GaN surface. One explanation could be the passivation aspect of SiN that can prevent PL suppression from the smaller NPs, which is absent is the case of GaN/Ag.

Considering the SiN coating types, a large difference is observed between the TF and NR coatings for the air-side scattering as seen in Fig. 5.25(b). The metal-air LSP mode for the SiN-NR has a larger scattering than that of SiN-TF. These properties appear to agree with the observed PL ratio spectra, where the GaN-side emission for SiN-NR exceeds that of SiN-TF as seen in Fig. 5.23(b).

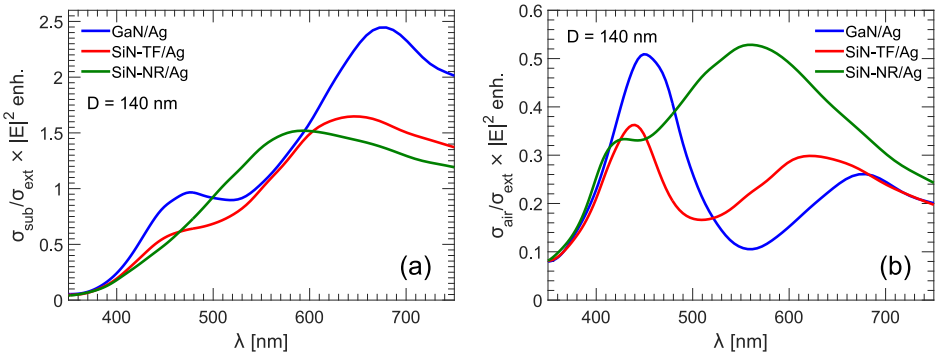

Figure 5.25: The SER and intensity-enhancement product for Ag NP with 140 nm diameter on GaN, GaN/SiN-TF and GaN/SiN-NR substrates. **(a)** Substrate-side and **(b)** air-side scattering component.

The intensity field profiles of the Ag NP on the considered substrates are shown in Fig. 5.26 at the emission wavelength of 530 nm. The largest field intensity is observed for the NP on SiN-NR due to the close overlap between the LSPR and the considered wavelength.

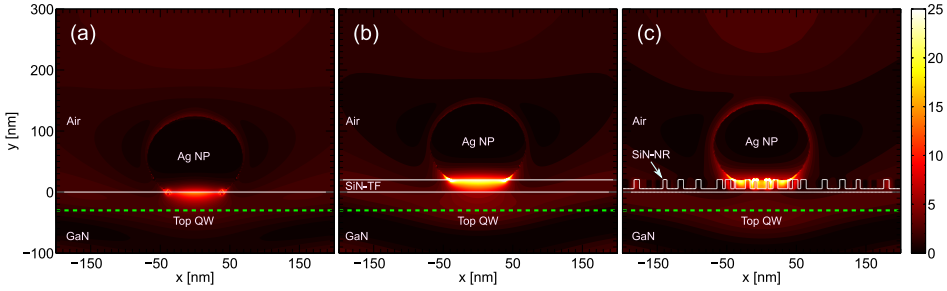

Figure 5.26: E-field intensity profiles, $|E|^2$, at 530 nm wavelength for Ag NP with 140 nm diameter on **(a)** GaN, **(b)** GaN/SiN-TF, and **(c)** GaN/SiN-NR substrates.

5.2.3.3 Ag nanoparticle size dependence

We proceed to consider the Ag NP size dependence of the emissions from dielectric coated samples. Fig. 5.27(a) shows the sapphire-side PL spectra for the samples with Ag NPs on SiN-NR coating. The trends appear similar to those from dielectric TF coating in Fig. 5.10 when considering NPs of equivalent sizes (i.e. 16 nm Ag TF RTA on SiN-NR is compared to 12 nm Ag TF RTA on SiN-TF). The

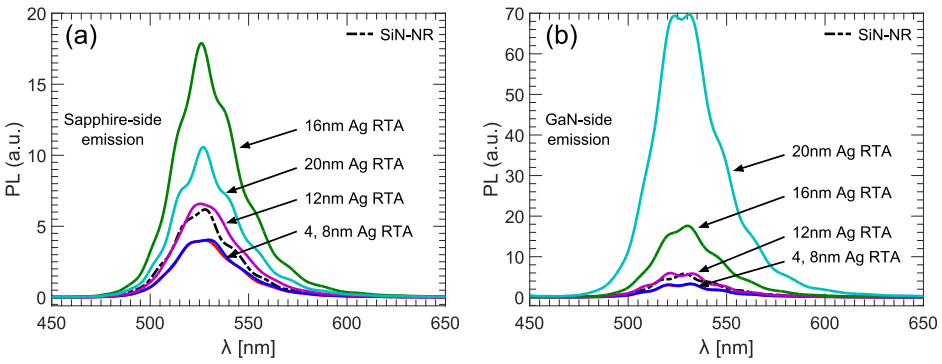

Figure 5.27: Measured PL spectra from **(a)** sapphire-side and **(b)** GaN-side emission for SiN-NR coated samples with different Ag NP sizes. The PL spectra of the SiN-NR coated samples without Ag NPs are also shown for comparison (black dashed lines). All the spectra are normalized relative to the PL intensity peak of the as-grown sample.

16 nm Ag case results in a higher PL enhancement compared to the 20 nm Ag. A noticeable difference is observed for the small sized Ag NPs from 4 nm and 8 nm Ag which now results in PL quenching, similar to the situation previously observed with SiO_2-TF.

In the last chapter we explained PL quenching as being due to the large absorption of the NPs and that it could be mitigated by inserting the SiN dielectric layer. Considering the results in this chapter, however, the explanation could also be related to surface passivation effects as seen from the difference between SiO_2-TF and SiN-TF coatings, where SiO_2 could not eliminate PL quenching as SiN. In the current investigation with SiN-NR, the passivation might have been affected in the etched areas by the RIE process resulting in surface states thereby degraded IQE by small sized NPs. With these considerations, it is difficult to determine whether the PL degradation and its recovery using SiN-TF is due to surface states and passivation or due to the absorption properties of the NPs.

The emissions from the GaN-side are shown in Fig. 5.27(b) for the SiN-NR coating. Once again, the NP coating which showed the strongest enhancement from the sapphire-side (16 nm Ag) is significantly exceeded by the largest NP size distribution (20 nm Ag). The IPLE factor due to the Ag NPs relative to the SiN-NR coating is 12.8 for GaN-side emission of 20 nm Ag. This is higher than the enhancements obtained from Ag NPs on SiN-TF from 20 nm Ag, where the IPLE from GaN-side emission was 10.9. The large enhancement cannot solely be attributed to LSP-QW coupling, but includes the contributions of LEE enhancement from Ag NPs.

The PL ratio spectra for sapphire- and GaN-side emissions relative to the SiN-NR coated sample are shown in Fig. 5.28. From the sapphire-side PL ratios, the 16 nm and 20 nm Ag samples exhibit a dip feature around 515 and 524 nm, respectively. The dip features in the PL ratios appear around the same location as the dips in the transmittance spectra in Fig. 5.21(b). It is also noteworthy that the GaN-side emission enhancement has peak around these wavelengths, and is blue-shifted relative to the peaks observed from the sapphire-side PL ratio. The difference between the metal-air and metal-substrate LSP modes might explain these observations. It is, however, difficult to correlate the transmittance dips with the PL ratio spectra, to draw conclusions about LSP-QW coupling. One reason could be contribution of LEE enhancement, which distorts the features of the LSP-QW coupling enhancement.

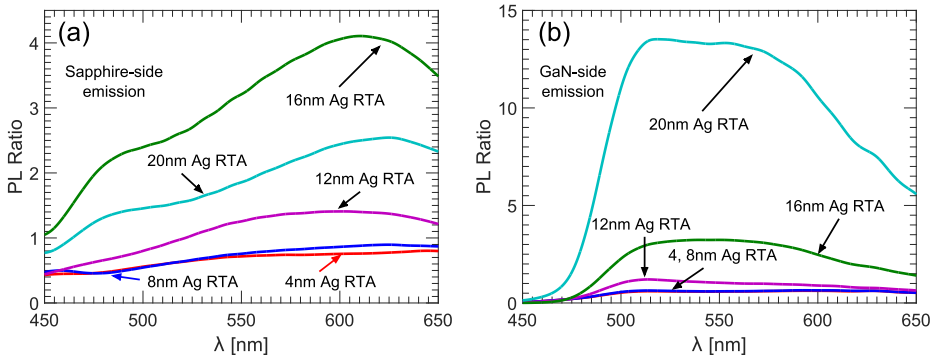

Figure 5.28: PL ratio spectra showing the effects due to Ag NPs relative to the SiN-NR coated samples without Ag NPs for **(a)** sapphire-side and **(b)** GaN-side emission.

Simulation results of the SER and intensity-enhancement product, shown in Fig. 5.29(a), reveal an optimum NP size around a diameter range of 100-140 nm for the substrate-side scattering component at 530 nm. The product is seen to decrease above this range. This is similar to the PL intensity measured from the sapphire-side where the highest enhancement is not obtained from the largest Ag NPs. Considering the air-side scattering component in Fig. 5.29(b) the dependence is seen to be more complicated, where an optimum NP size is present, but the product does not decrease to a similar degree. However, it is seen that the metal-air LSP mode approaches the emission wavelength (white dots) with increasing NP size, which could explain the PL enhancement observed from the GaN-side emission for large Ag NPs.

Apparently the metal-substrate mode significantly contributes to the air-side scattering with this configuration of Ag NP on NR structures. For comparison, the simulation results for the SiN-TF substrate are shown in Fig. 5.29(c,d), where

it is seen that the metal-substrate mode does not have a similar contribution to the air-side scattering as seen for the SiN-NR case in (b).

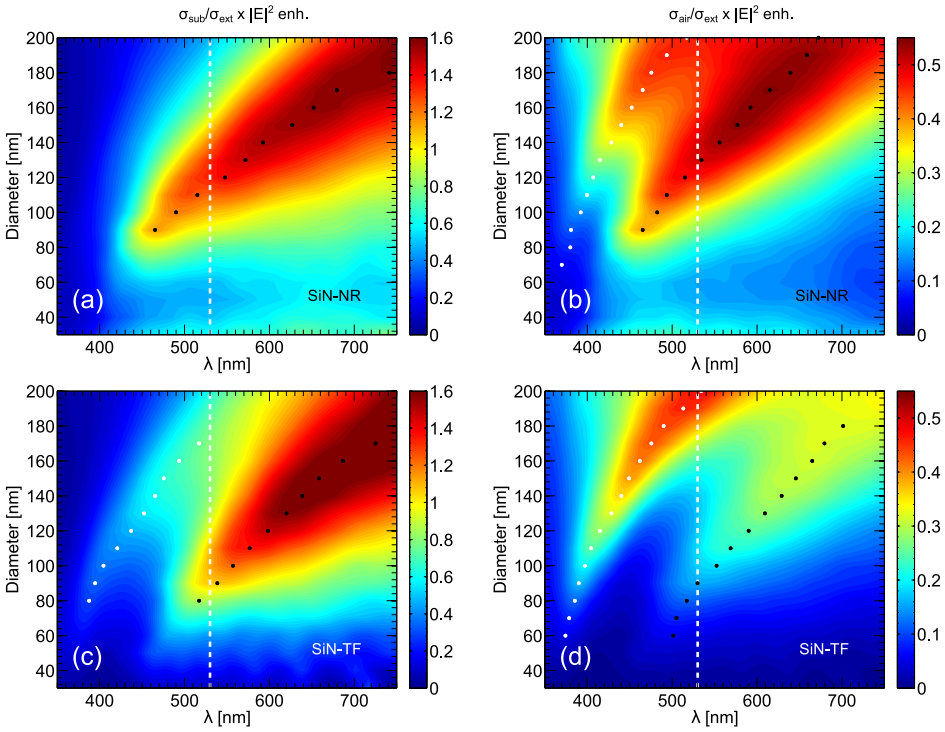

Figure 5.29: Contour plot of the simulated SER and intensity-enhancement product showing the wavelength and size dependence for. **(a)** Substrate-side and **(b)** air-side scattering component for Ag NP on GaN/SiN-NR. **(c)** Substrate-side and **(d)** air-side scattering component for Ag NP on GaN/SiN-TF. The emission peak at 530 nm is marked by the vertical dashed-line. The peak locations of the metal-substrate (black dots) and metal-air (white dots) LSP modes are also shown.

To summarize the experimental results, the total integrated enhancements, including the sapphire- and GaN-side emissions, relative to the as-grown sample emission are illustrated in Fig. 5.30 for all the dielectric coating types considered. Similar trend is observed for all the samples, where the enhancement factor is seen to increase with Ag NP size. The largest enhancements are obtained from the SiN-NR coating, with a total IPLE reaching beyond a factor of 31. SiO_2-NR and SiN-TF coatings also demonstrate very large enhancements. The inset of the figure shows the enhancements attributed to the Ag NPs relative to the

dielectric coatings alone. From the 8 nm thickness of the pre-annealed Ag TF, the enhancement is seen to increase exponentially with NP size. This is mainly attributed to the large improvements from GaN-side emission.

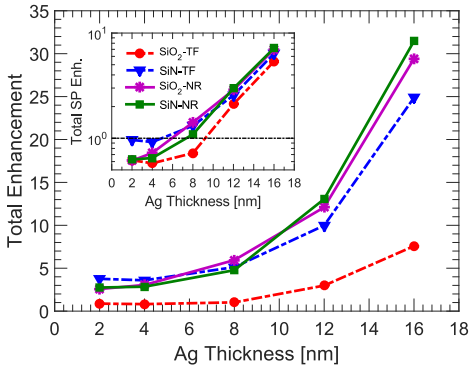

Figure 5.30: Total integrated enhancement from both sapphire- and GaN-side emission for samples with Ag NPs on dielectric coatings relative to the as-grown sample emission. The inset shows the enhancement due to Ag NPs.

5.2.4 Conclusions

The aim of fabricating a low-index optical coating between Ag NPs and the GaN surface was achieved by densely spaced NR-pattern of SiN and SiO_2 with uniform structure heights, where the etch-mask to form the NR-pattern consisted of self-assembled Au NPs. Compared to dielectric coatings without nano-pattern, the NR-pattern improved the PL intensity which could be attributed to LEE enhancement.

Given that the NR heights were 20 nm, forming Ag NPs on the surface would allow for LSP-QW coupling to improve the IQE. Indeed the Ag NPs on NR coatings resulted in a similar degree of enhancement as seen from Ag NPs on TF coatings. However, due to the improved LEE from the NRs, the total enhancement relative to the as-grown sample was higher than those with Ag NPs on TF coatings.

CHAPTER 6

Surface plasmon compatible nanopillar structures

Until now, we have mainly considered thin p-GaN layer structures to enable plasmonic coupling with the active region from metal nanoparticles. Conventional LED structures with thick p-GaN layer were briefly discussed where it was shown that a partially etched p-GaN could allow nanoparticle deposition in the near-field of the light-emitting region. In this chapter we analyse the fabrication of nanopillars on conventional LED structures using a cost-effective nano-lithography technique based on polymer nanosphere templates. The nanopillar structures allow for an alternative way of obtaining plasmonic coupling with the active region, i.e. by embedding metal nanoparticles between the pillar structures. Additionally, by etching through the active region it is possible to improve both the light extraction efficiency (LEE) and internal quantum efficiency (IQE), the latter being through the effects of lattice-strain relaxation.

Nanopillars of different sizes are fabricated and analysed using Raman spectroscopy. We have shown that nanopillar LEDs can be significantly improved by applying a combination of ion-damage curing techniques, including thermal and acidic treatment, and have analysed their effects using x-ray photoelectron spectroscopy (XPS).

6.1 Nanosphere lithography

6.1.1 Nano-patterning for light extraction

Much effort has been made during last decade to improve the efficiency of InGaN based LEDs through either the IQE or LEE. Due to the high refractive index contrast between GaN and air, a lot of the light is trapped inside the LED epi-structure, and by employing surface texturing the LEE can be improved. Surface roughening on the p-GaN surface has been investigated using chemical or laser etching to form roughness heights in the range of 5-20 nm improving the wall-plug efficiency.[105,106] When nano-structures are fabricated on the n-GaN surface after removing the sapphire substrate, it is possible to achieve larger structures due to

larger etch depths and it has been reported that an output power increase by a factor of 2-3 could be obtained with feature sizes on the order of 500 nm.[107]

As opposed to random surface patterning, fabricating periodic and ordered nano-structures would allow a higher degree of control over the dimensions. One example of nano-patterning that can improve light extraction by inhibiting lateral propagation of light in the semiconductor is photonic crystral (PhC) structure, which also has the possibility of modifying the IQE through the Purcell effect. PhC hole-pattern structure has been demonstrated on the *p*-GaN layer without penetrating the active region, showing improved output power.[108,109] PhC structure has also been investigated using a tunnel-junction LED to enhance current spreading through the PhC region with a resulting extraction efficiency improvement by a factor of 1.5.[110] For flip-chip LED design the PhC structure needs to be formed on the *n*-GaN side, which has also been demonstrated by Wierer *et al.*[111] The formation of nano-structures is not limited to the epi-layers. Recently attempts have been made to improve the device efficiency by fabricating PhC structures on a post-growth deposition layer without modifying the epi-layers, which evades the disadvantage of active region damages from reactive-ion etching (RIE) processes.[102,112,113]

Simply etching the *n*-GaN or *p*-GaN layer to form nano-structures would not significantly modify the fabrication steps required to make ohmic-contacts for LEDs. There is, however, a larger potential for efficiency improvement by etching through the active region to induce strain relaxation and weaken the quantum-confined Stark effect (QCSE).[114–123] Compared to blue, green InGaN quantum-well (QW) structures have a higher strain due to larger lattice mismatch as the InN mole fraction is increased.[27] The strain relaxation effects and the resulting IQE improvement is therefore expected to be higher for long-wavelength QW emitters.

Fabricating nano-structures to induce strain relaxation can be achieved in several ways including cost-effective techniques such as the use of self-assembled metal nanoparticles as etch mask[117–119] or nanosphere lithography (NSL).[120–125] The latter has the advantage of providing some degree of control over the periodicity and structure size in addition to the possibility of maximizing the active region fill factor. Early attempts at fabricating nanopillar structures using NSL with closely-packed polystyrene (PS) nanospheres have employed metal templates formed in the interstices of the nanospheres, as etch mask.[124] Another approach is to directly use PS nanospheres as the masking material whereby nanopillar structures can be formed through an RIE process, and the pillar diameter can be varied by oxygen plasma etching of the nanospheres.[125]

For GaN/InGaN LED epi-structures, the effects of nano-structure size on strain relaxation and photoluminescence (PL) improvement have been investigated using periodic structures.[114–116] Various RIE damage curing techniques have been tested including thermal annealing,[114] KOH to etch damaged side-walls,[116,119,122] and hydrochloric acid (HCl) treatment,[118,119] all exhibiting improved PL compared to as-etched samples.

In this chapter we employ NSL in fabricating nanopillars on green LED epi-structures, and Raman spectroscopy is used to confirm that strain relaxation takes place after nanopillar etching. We investigate two different post-etch damage curing techniques, i.e. rapid thermal annealing (RTA) and HCl chemical treatment, and how they can be combined to yield an even higher improvement. We also consider how the treatments depend on nanopillar sizes.

6.1.2 Polystyrene nanosphere coating

The possibility of self-assembling a mono-layer of dielectric nanospheres on a surface has been thoroughly investigated over the past years.[126–129] Nanosphere sizes down to 50 nm can be assembled as a closely-packed mono-layer, and even have different geometries, such as triangular and rectangular shapes.[130] Various techniques for self-assembly are available, such as drop-coating, dip-coating and spin-coating.[131] This enables the nanospheres to be used as templates during nano-lithography processes; denoted NSL. Closely-packed nanospheres can provide a periodic hexagonal structure, which makes it a cost-effective alternative to nano-patterning methods such as e-beam and nanoimprint lithography. Polymer nanospheres are commercially available in aqueous solutions with sizes ranging from below 100 nm to micrometre scales, and in different concentrations.

6.1.2.1 Drop-coating

We investigated two different ways of coating a closely-packed mono-layer of PS nanospheres as templates for nanopillar fabrication on LED epi-structures. The first was the drop-coating method, which involves spreading a dilute drop of nanosphere suspension on a horizontal surface. As the solvent (water) evaporates, the nanospheres can, under the right conditions, self-assemble into a closely-packaged hexagonal lattice. The procedure critically depends on the concentration of solids in the suspension, ambient pressure, humidity, and substrate condition. We used commercially available PS nanosphere suspension (from Fisher Scientific ApS) with 10 % concentration of solids, having average diameter of 490 nm and a 2.5 % coefficient of variation. A surface treatment of the substrate is necessary to achieve a hydrophilic nature, for the adhesion of nanospheres before their coating. In this case a layer of SiO_2 deposited using plasma-enhanced chemical vapour deposition (PECVD) will have the hydrophilic property needed.

The schematics of the drop-coating procedure is shown in Fig. 6.1. A Cu-wire is used as a boundary, and a glass plate is clamped on top of the Cu-wire. The nanosphere suspension is injected into the region bounded by the substrate, Cu-wire and glass plate. The sample will be left for about six hours for the evaporation of the solvent.

The result of the drop-coating is shown in Fig. 6.2(a), where a layer of nanosphere coating is obtained on SiO_2 surface. The bright boundaries are vacancy

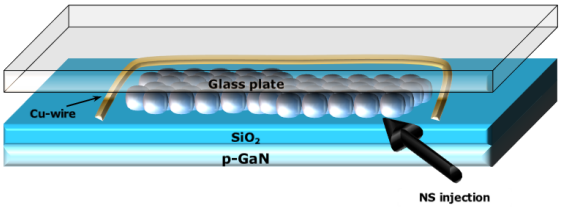

Figure 6.1: Illustration of the drop-coating procedure showing.

and lattice defect regions. The mono-layer nature of the coating is shown in Fig. 6.2(b). Although a relatively large area of uniform mono-layer coating is obtained, the large-scale view shows that the coating is limited to certain areas of the surface despite having spread the suspension throughout the region in view. It is very difficult to control the success-area coverage during the coating, and the only optimization parameter available in our case is the concentration of solids in the suspension.

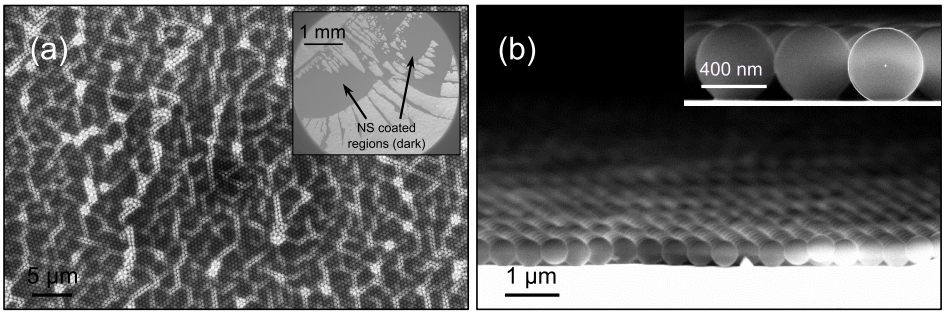

Figure 6.2: Formation of closely-packed mono-layer of nanospheres on SiO_2 surface following the drop-coating method. **(a)** Top-view SEM image. Inset shows a large-scale view where the dark regions are mono-layers and remaining regions are largely dispersed or non-existent nanospheres. **(b)** Cross-sectional SEM view.

6.1.2.2 Spin-coating

The drop-coating method is not a feasible solution for large-scale applications. In contrast using the spin-coating method, closely-packed mono-layer of nanospheres has been successfully demonstrated with even wafer-scale uniformity.[132–136] The spin-coating process is not without difficulties compared to the drop-coating method, and although it is possible to obtain large-scale coating uniformity, the process depends on a large number of parameters. These include, but are not limited to: Spin-speed, -acceleration, -duration and number of steps; substrate surface condition and size; droplet quantity; suspension concentration and age; nanosphere size.

We use the same PS nanosphere suspension as used for the drop-coating, which consisted of 10 % solids. The substrate is coated with SiO_2 as required by the lithography process, but is also necessary for nanosphere adhesion. Even though the SiO_2 surface is hydrophilic after the PECVD process, the samples still required a treatment to increase the hydrophilicity of the surface in order to achieve the best possible spread of the droplet prior to spinning. This treatment consisted of exposing the SiO_2 surface to oxygen plasma for 10 min at 100 W RF power using a plasma ashing process. We employed a two-step spin-coating process with a fast spin to spread the nanospheres followed by a slow spin for drying. The recipe is illustrated in Fig. 6.3, where the initial acceleration is 600 rpm/sec, and the first spin-speed is a variable parameter to be optimized, while the rest of the given parameters such as the second acceleration and speed, are fixed to 200 rpm/sec and 1000 rpm, respectively. The samples tested were approximately 1×1 cm in size, and the suspension droplet was 10 μL on each test.

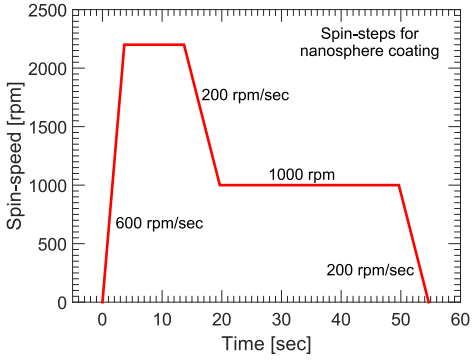

Figure 6.3: Two-step spin-coating recipe for nanosphere suspension of 10 % solids with 490 nm of diameter.

Fig. 6.4 shows the result of spin-coating using spin-speeds from 2600-1800 rpm. A mono-layer of nanospheres is obtained with the highest spin-speed in (a) and (b), however, the disperse nature of the particles begs to reduce the spin-speed. The optimal speed appears to be around 2200 rpm, with the corrosponding results shown in (c) and (d), where a closely-packed mono-layer is seen to be formed on the surface. Unfortunately, even with thorough optimization of the spin-speed, double-layered regions could not entirely be eliminated. One such example is marked in (c). Increasing the spin-speed worsens the amount of defects seen in (d). Decreasing the speed gives a higher quality mono-layer, but the amount of double-layered domains also increase as shown in (e) and (f). After tedious optimizations, we settled for the following spin-parameters: 10 sec at 2200 rpm with 600 rpm/sec, followed by 30 sec at 1000 rpm with 200 rpm/sec.

One way of improving the spin-coating process would be to use a surfactant called Triton X-100 diluted with methanol.[125,137] Another approach is to modify the nanosphere solvent to a 1:1 solution of de-ionized water and ethanol.[136] We

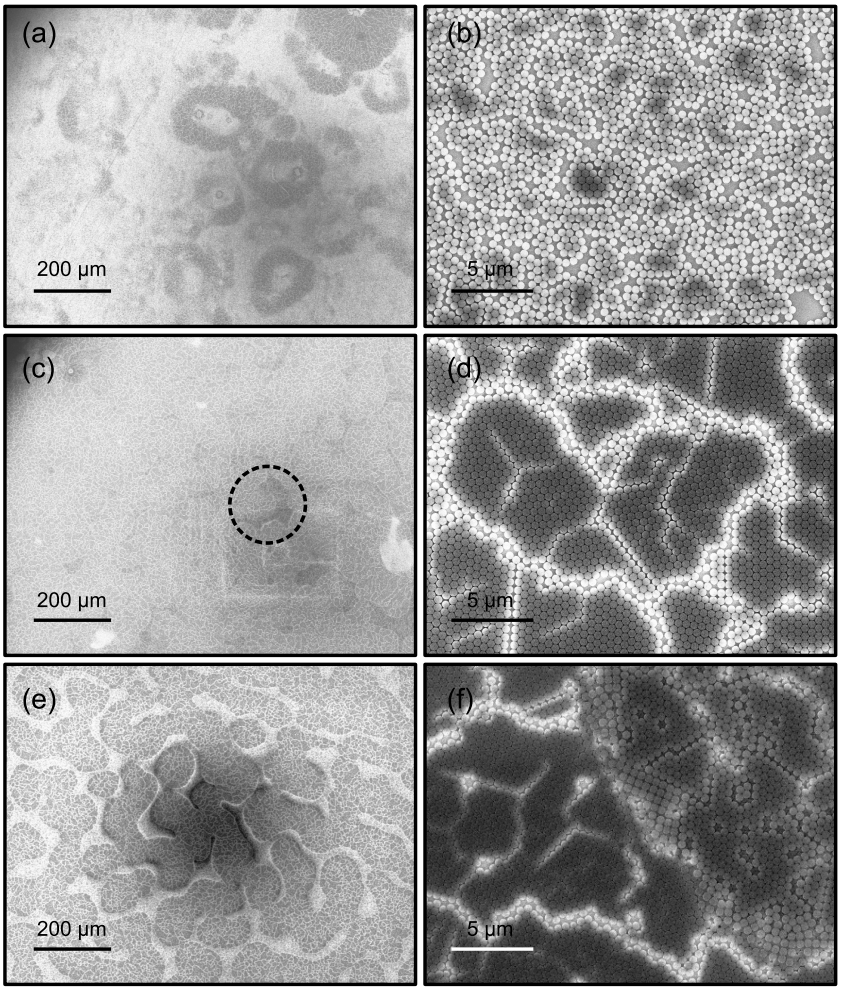

Figure 6.4: Results of spin-coating a suspension of nanospheres with a concentration of 10 % on an SiO_2 surface treated with oxygen plasma. The spin speeds are: **(a,b)** 2600 rpm, **(c,d)**, 2200 rpm and **(e,f)** 1800 rpm.

tested the latter mentioned, which unfortunately did not yield a successful result. This was due to the formation of large nanosphere clusters during the water extraction process from the suspension to increase the concentration. Clusters had a disastrous effect on the spin-coating and its reproducibility. The surfactant, Triton X-100, will be investigated in future studies.

6.1.3 Fabrication of nanopillars

For the nanopillar LED experiments we used commercially available GaN epi-wafers (from Precision Micro-Optics LLC) consisting of a similar epitaxial structure as those considered in the previous chapters with an active region consisting of five QWs. The *p*-GaN layer was 150 nm thick, and a capping of 1 nm InGaN was grown on top of the *p*-GaN. For the NSL process we deposited 150 nm SiO_2 by means of PECVD. A process flow overview to form nanopillar structures using PS nanospheres as template is shown in Fig. 6.5. A closely-packed mono-layer of PS nanospheres with diameter of 490 nm was spin-coated on the oxygen plasma treated SiO_2 surface with the recipe mentioned above, and the spheres were then shrunk in size and the pattern transferred to the SiO_2 layer using RIE processes. The pattern from SiO_2 to GaN was then transferred using ICP-RIE followed by nanosphere and SiO_2 removal. These steps will be described in more details in what follows.

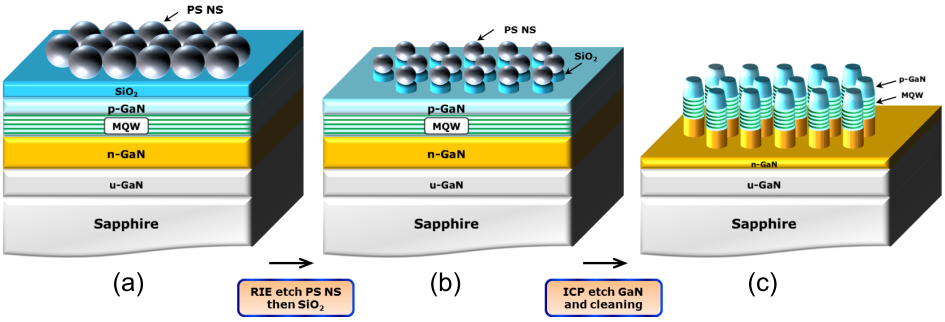

Figure 6.5: Nanopillar fabrication process using nanosphere lithography. **(a)** SiO_2 layer is deposited prior to nanosphere spin-coating to serve as etch mask for GaN etching. **(b)** RIE is used to shrink the nanosphere size and form SiO_2 nanopillars. **(c)** The pattern is then transferred to GaN by ICP-RIE process. Acetone and HF is used to remove the nanospheres and the SiO_2 layer.

6.1.3.1 Nanosphere size reduction

To investigate different cross-sectional sizes of nanopillars, the nanospheres were shrunk in size using an O_2 RIE process with 45 sccm O_2 flowrate and 40 mTorr of chamber pressure. Although it seems like a straight forward task to shrink the nanosphere size, it nonetheless proved to be a difficult process to control. One of the important aspects to have gotten under control was the chamber condition and its history. Since the SiO_2 layer was to be etched using a CHF_3/N_2 chemistry after shrinking the sphere size, the next sample's sphere-shrinking process was

highly affected even though the only process gas present was O_2. It was therefore necessary with a cleaning and pre-conditioning step before the nanosphere etching, using O_2 cleaning of the chamber with an RF power of 100 W. The importance of chamber cleaning is illustrated in Fig. 6.6. Etching the PS nanospheres in a chamber that has gone through a CHF_3 RIE process prior to the PS etching, resulted in a non-uniform nanosphere shape with higher etch-rate.

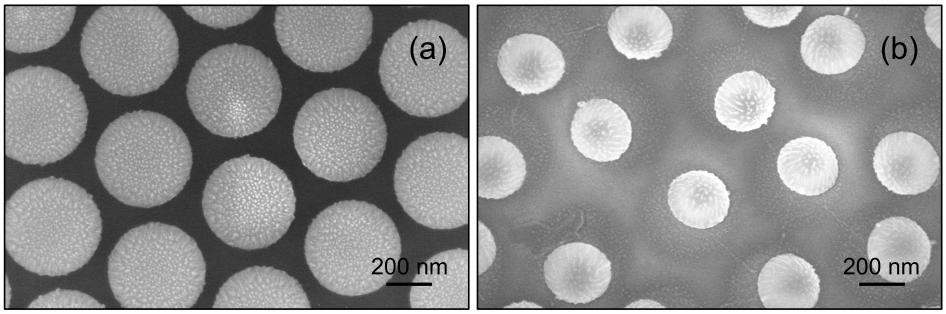

Figure 6.6: PS nanospheres etched for 30 sec in O_2 RIE with 45 W RF power **(a)** with and **(b)** without a chamber cleaning after a CHF_3 RIE for SiO_2 etching.

Another critical point was the etch-rate drift over time which is illustrated in Fig. 6.7. This variation made it imperative to consistently measure the etch-rate prior to every process, to ensure that the desired dimensions could be obtained. The given etch-rate is calculated from the change in diameter measured from the top-view cross-section.

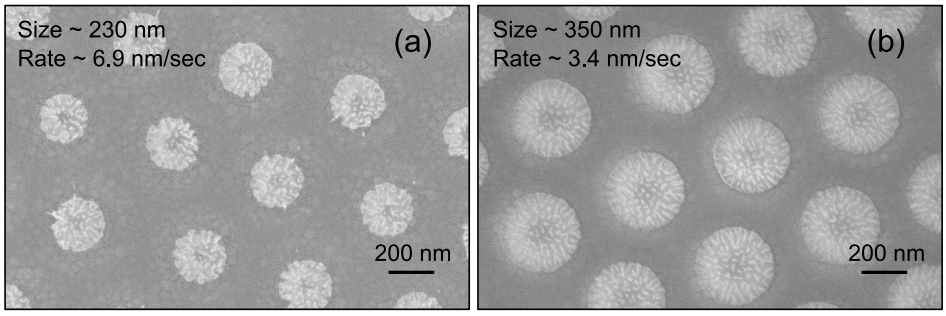

Figure 6.7: Illustration of nanosphere etch-rate variation using an O_2 RIE process at 100 W RF power for 36 sec in both cases, with the same pre-conditioning. The results of **(a)** and **(b)** are obtained on the same day with approximately 3 hours apart.

It is also noticed that the sphere shape is distorted the more it is etched, and this process depends on the plasma RF power. Fig. 6.8 shows nanospheres which are shrunk to around the same size using various RF powers. Although a low RF power gives better result for small size reductions as shown in Fig. 6.6(a), this is not the case for larger size reductions such as below 300 nm in diameter. Comparing Fig. 6.8(a) and (c), the low power RIE at 20 W distorts the shape of the spheres producing sharp peripheries, which is not seen from the high power RIE at 100 W. We therefore employed a 60 W RIE to reach nanosphere sizes around 400 and 300 nm, and 100 W to reach around 200 nm or below.

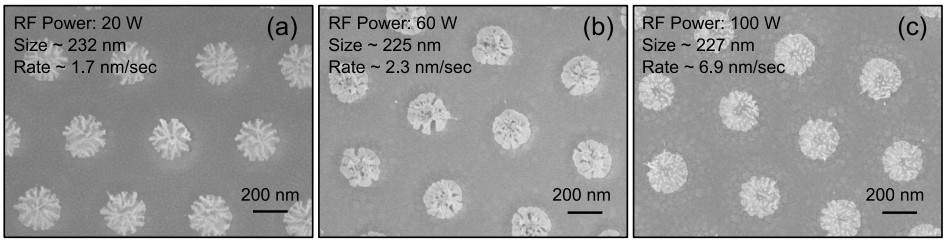

Figure 6.8: Influence of the O_2 RIE plasma power on the nanosphere shape. The results are obtained by etching for **(a)** 150 sec at 20 W, **(b)** 112 sec at 60 W, and **(c)** 36 sec at 100 W.

Starting with a nanosphere diameter of 490 nm, the aim was to obtain various dimensions, including diameters below 100 nm by etching the nanospheres. However, it proved to be rather difficult to shrink the spheres below 200 nm in diameter, due to shape distortion as shown in Fig. 6.9. The shape was difficult to preserve with long etch durations, hence the desired diameters below 200 nm were not achievable.

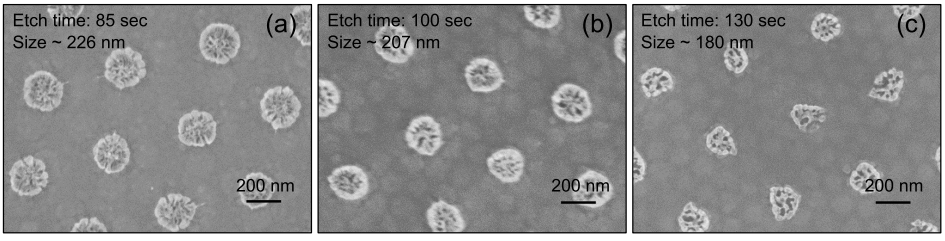

Figure 6.9: Nanosphere size-decrease with increasing O_2 RIE duration at 100 W RF power for **(a)** 85 sec, **(b)** 100 sec, and **(c)** 130 sec.

For the nanopillar LED investigations, four different samples were fabricated, each with a different nanosphere diameter. For three of the samples (A-C) the PS nanospheres were shrunk prior to SiO_2 etching, and for the fourth sample (D) the nanospheres remained as-deposited and closely-packed. As such the different nanosphere diameters for samples A-D were 220, 360, 430 and 490 nm, respectively.

6.1.3.2 SiO_2 etching

To transfer the pattern from the PS nanospheres the samples were etched using a CHF_3/N_2 chemistry at 50 W RF power, with flowrates of 8/43 sccm and a chamber pressure of 38 mTorr. It was important that the plasma did not contain O_2 to avoid etching the PS nanospheres. The effect of CHF_3 RIE on the PS nanospheres is illustrated in Fig. 6.10. The SiO_2 etch-rate was in the range of 26 to 30 nm/min. The masking cross-section of the nanospheres is seen to remain nearly unaffected by the process with an insignificant lateral etch suggesting that the nanospheres mainly went through a physical etching. The selectivity of nanosphere diameter-shrinking relative SiO_2 etch-rate is approximately 1:3. This leads to SiO_2 nanopillars with angled side-walls of about 80° relative to the horizontal plane. The vertical etch-rate of the nanospheres was around 16 nm/min which roughly gives a vertical selectivity of 1:1.6 between PS and SiO_2.

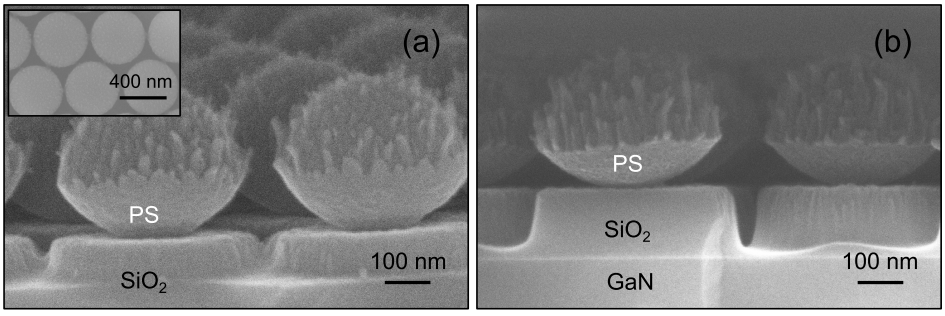

Figure 6.10: The impact of the SiO_2 dry-etching on PS nanospheres using a CHF_3/N_2 RIE process for a duration of **(a)** 150 sec and **(b)** 300 sec. The inset shows a top-view image of the size-reduced nanospheres before the SiO_2 etch.

As shown previously, reducing the nanosphere size resulted in a distortion of the sphere shape, and this pattern is naturally expected to be transferred to the SiO_2 nanopillar structures. Fig. 6.11(a) shows the rough SiO_2 side-wall formation from nanospheres shrunk to around 325 nm in diameter prior to SiO_2 etching as shown in the inset. During the O_2 RIE process the nanospheres are etched from all directions and their heights are therefore also reduced. Further reducing the nanosphere diameter to 225 nm, the templates do not remain throughout the SiO_2 dry-etching process as shown in Fig. 6.11(b), where the nanospheres are not visible on top of the SiO_2 nanopillars. This not only distorts the nanopillar shape in the lateral direction, but also in the vertical direction.

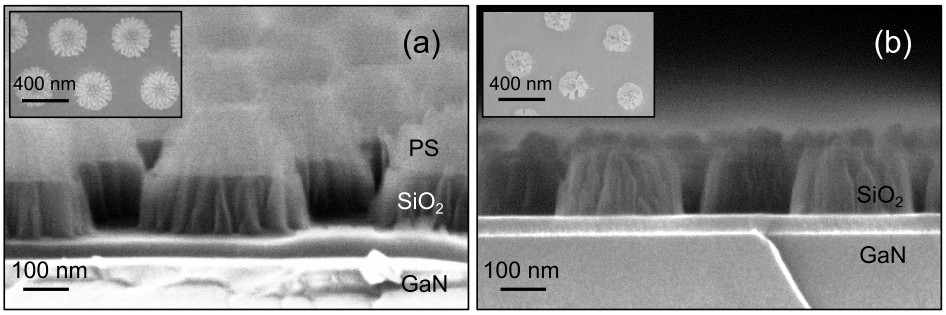

Figure 6.11: Pattern transfer from size-reduced PS nanospheres to SiO_2 from 300 sec of CHF_3 RIE process, with nanosphere diameters of **(a)** 325 nm and **(b)** 225 nm. The insets show the size-reduced nanospheres before SiO_2 etching in each case.

6.1.3.3 Pattern transfer to GaN/InGaN epi-structure

Following the pattern definition on SiO_2, ICP-RIE was employed to transfer the pattern to the LED epi-structures (see Fig. 6.5(c)). An ICP-RIE Plasmalab-100 system from Oxford Instruments was used to etch GaN/InGaN layers with Cl_2/Ar chemistry where SiO_2 and the remaining PS nanospheres acted as etch mask. Process parameters were 400/75 W of coil/platen RF power, 20/3 sccm flowrate of Cl_2/Ar, 5 mTorr pressure, and 20 °C platen temperature. Samples were etched for 210 sec, and the obtained structure heights were in the range from 570 to 610 nm, yielding an etch-rate between 163 to 174 nm/min. The selectivity between SiO_2 and GaN was around 1:5, but due to the presence of PS nanospheres the selectivity was higher. Results of ICP dry-etching for samples with three different nanosphere diameters are shown in Fig. 6.12. The profile of the irregular nanospheres is seen to be transferred to GaN nanopillar walls similar to the situation with SiO_2 nanopillars when the nanospheres are shrunk below 400 nm in diameter. Another feature to notice is the decreasing side-wall angle with nanosphere size, where the angles for 430 nm, 325 nm, and 223 nm sphere diameters are 89°, 85° and 79°, respectively. It was not done in this work, but if desired, a short KOH treatment can be applied to the GaN/InGaN nanopillars as anisotropic etching to produce vertical side-walls.[116]

Possible remnants of the PS nanospheres were cleaned using acetone followed by oxygen plasma etching, and subsequently the SiO_2 layer was removed by 5 % hydrofluoric acid (HF) wet-etching. Damage curing treatments, including RTA and HCl, were then applied at this step of the process. The nanopillar structures of the four samples to be investigated, A-D, are shown in Fig. 6.13. Since the nanospheres were not shrunk in case of sample D, neighbouring nanopillars are seen to be connected. Sample A has a roughened pillar-floor with random nano-structures between the pillars as seen in Fig. 6.13(a). This appears to be

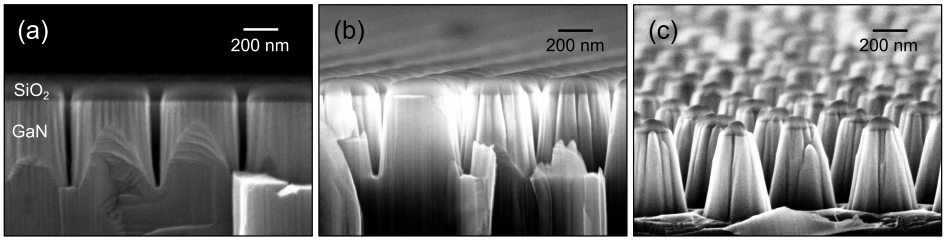

Figure 6.12: Formation of GaN/InGaN epi-structure nanopillars after Cl_2/Ar based ICP dry-etching with SiO_2 as masking layer. The PS nanosphere diameters prior to the SiO_2 pattern definition were **(a)** 430 nm, **(b)** 325 nm, and **(c)** 223 nm.

related with micro-masking effects possibly originating from PS residues of the size-reduced nanospheres whose pattern is transferred during the SiO_2 dry-etching process.

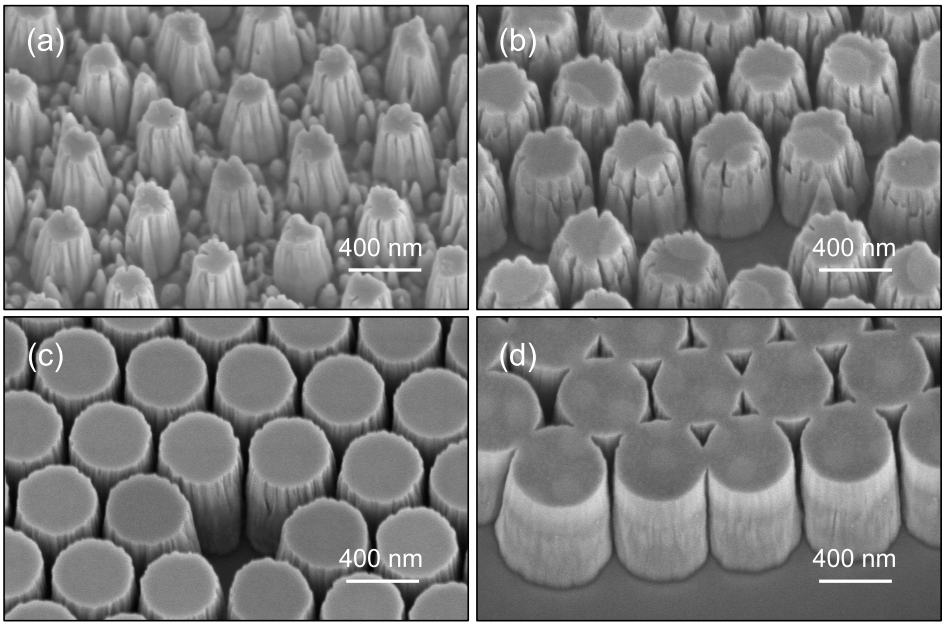

Figure 6.13: The structure of the nanopillars after removing the SiO_2 layer and PS nanospheres for the samples to be investigated; i.e. **(a)** sample A with 205 nm, **(b)** sample B with 350 nm, **(c)** sample C with 425 nm, and **(d)** sample D with 490 nm of top-surface diameter.

6.1.4 Conclusions

The NSL process considered in this section can be divided into four main parts including nanosphere coating, nanosphere size reduction, pattern transfer to SiO_2, and pattern transfer to the LED epi-structure. The first two parts are the most critical as they determine the geometrical properties of the final nano-structures, and they also constitute the most challenging aspect of the process. The aim is to achieve a closely-packed mono-layer of nanosphere coating, and preserve the circular cross-sectional shape during the size-reducing O_2 RIE process. Although we have employed nanospheres of a fixed diameter and modified the dimension subsequently, it can be avoided by using nanospheres of different sizes, where the spheres need to be etched just enough to achieve disconnected nanopillars. Such an approach was very difficult to realize due to the challenge in obtaining a closely-packed mono-layer of nanospheres using smaller sphere sizes such as 150 and 300 nm diameters with the spin-coating and drop-coating methods.

6.2 Characterizations

6.2.1 Surface treatments

After the ICP etching and removal of SiO_2 together with PS nanospheres, PL measurements were conducted using a 405 nm excitation laser. The excitation and detection were from the sapphire-side of the samples. The PL spectra of samples B and C are shown in Fig. 6.14, where all the intensities are normalized to the reference (as-grown) sample peak value. As mentioned previously, the ICP etching process of GaN/InGaN causes damage to the QWs. To investigate the effects of different damage curing techniques, we first performed RTA for 10 min at 500 °C on sample B. The result is shown in Fig. 6.14(a), where PL intensity is enhanced compared to the as-etched nanopillar sample with an integrated PL enhancement (IPLE) factor of 1.96. Succeeding the RTA process by an acidic treatment with 38 % HCl at room temperature for one hour, further enhanced the PL. The combination of RTA-HCl treatment resulted in an enhancement by a factor of 2.82. On sample C, we first investigated the effect of HCl treatment alone, and the result was an enhancement by a factor of 1.57 relative to the as-etched sample. Following the HCl treatment by RTA did not show a significant improvement as shown in Fig. 6.14(b). Apparently the sequence of these damage curing techniques is important when considering PL improvement and the combination provides a better result than either of them separately. This is witnessed by performing the RTA-HCl process on sample C and observing a higher enhancement compared to the HCl-RTA case in Fig. 6.14(b).

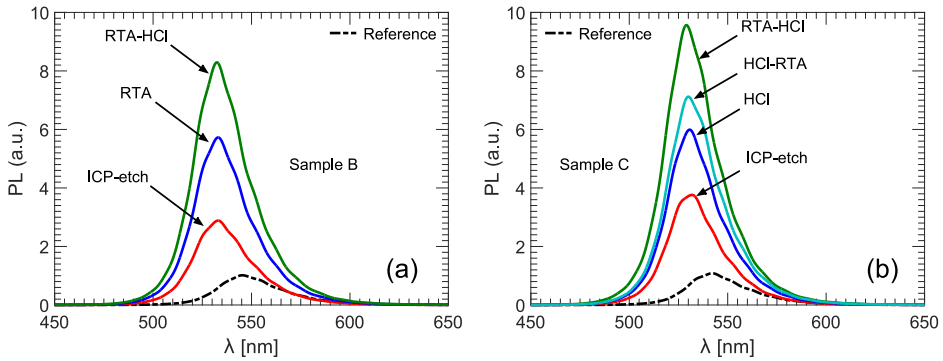

Figure 6.14: **(a)** PL spectra of sample B after formation of nanopillars (ICP-etch), after thermal annealing (RTA) and a combination of thermal annealing followed by 1 hr HCl treatment. **(b)** The PL spectrum of sample C and the effects of between different damage curing techniques.

From the PL spectra of Fig. 6.14, it is noticed that the emission peak is blue-shifted compared to the as-grown sample, and this is an indication of strain relaxation. To further consolidate the strain relaxation effects, Raman spectra were measured using a Thermo Scientific Raman DXR microscope. The excitation laser wavelength was 780 nm focused to a spot size of 3.1 μm with 20 mW power. The Raman spectra of the samples are shown in Fig. 6.15. Considering the E_2 (high) phonon mode of GaN we notice that the peaks of the etched samples are located around 569 cm^{-1} whereas the reference sample has its E_2 (high) peak at 571 cm^{-1}. The E_2 phonon-mode peak shift towards lower energy affirms that strain relaxation has taken place in the GaN/InGaN QWs.[123,138,139]

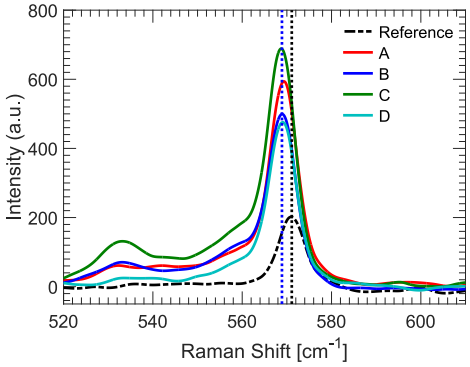

Figure 6.15: Raman spectra of the samples A-D after nanopillar formation compared to the as-grown sample.

6.2.2 Characterization of surface chemistry

To further understand the effects of different treatments we performed XPS measurements using a Thermo K-Alpha system from Thermo Scientific with an Al K-Alpha source. The pass energy was set to 200.0 eV for survey scan and 50.0 eV for high resolutions scans. The reference peak energy is C1s, C-C peak at 284.4 eV. Survey scan spectra are shown in Fig. 6.16. Comparing the as-etched sample spectrum with that of the reference, a difference to note is the F 1s peak at 685 eV, indicating the presence of fluorine contaminants, and is more clearly resolved in Fig. 6.17(a). Fluorine contaminants could have been introduced during the CHF_3 based RIE process, although their trace is eliminated either by thermal annealing or HCl treatment.

Significant Cl 2p and Cl 2s peaks are present in the HCl treated sample as shown in Fig. 6.17(b). It appears that the Cl_2 based ICP dry-etching of GaN/InGaN is not introducing similar levels of chlorine contaminants as the HCl treatment is. It has been known that HCl cleaning of GaN helps eliminate oxygen contaminants but leaves significant traces of chlorine, however, the benefit of Cl

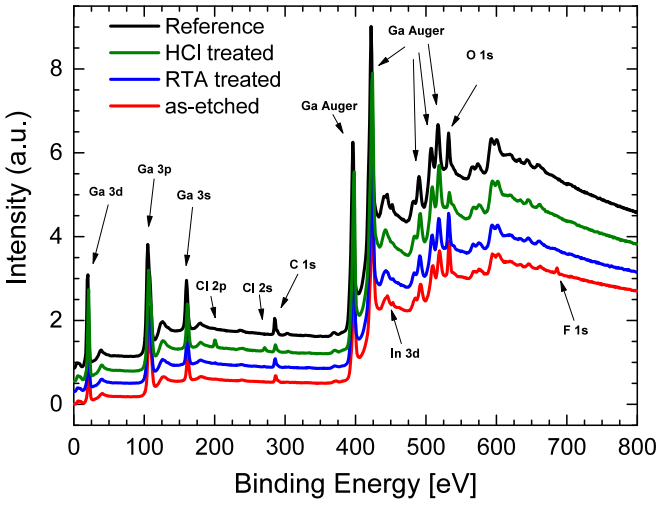

Figure 6.16: XPS spectra and highlight of notable differences between reference, etched and surface treated samples. The strong peaks near 400 eV are from Ga LMM Auger transitions.[140] The spectra are vertically shifted from each other for visibility.

is that it can tie up nitride dangling bonds and make the surface more resistant to re-oxidization.[141]

Since the as-grown sample has an InGaN capping layer, In $3d_{5/2}$ and In $3d_{3/2}$ core level peaks are measurable around binding energies of 444.8 eV and 452.2 eV, respectively, as seen from Fig. 6.17(c). The peak at 444.8 eV is likely due to indium native oxides (In_2O_3).[142] The two In $3d$ peaks vanish when the as-etched sample is cleaned in 5 % HF to remove the SiO_2 mask. When the etched sample is exposed to air over a prolonged time, indium native oxides will be formed on the exposed surface of the InGaN well. It is therefore imperative that the nanopillar side-walls are protected e.g. through a passivation layer. The thermal annealing and HCl treatments can also by themselves get rid of the native oxides (not shown). Fig. 6.17(c) shows the combined effect of RTA-HCl treatment.

In Fig. 6.17(d) we consider the O $1s$ core level peak which for the reference is deconvolved into three peaks at 530.4, 531.5 and 532.9 eV. For the as-etched sample, the lowest binding energy could not be resolved. The O $1s$ binding energy at 530.4 eV can be due to indium native oxides, In_2O_3.[142] The disappearance of this peak from the etched sample spectrum agrees with the findings from the In $3d$ spectra, where indium oxide has no trace for the as-etched sample. To understand why the peak disappears, we note that the as-etched sample has been treated with HF to remove SiO_2 mask. The HF treatment is expected to have etched away indium oxides hence leaving no trace in the XPS spectra. The binding energy at 531.5 eV can be ascribed to chemisorbed oxygen atoms forming gallium oxides,

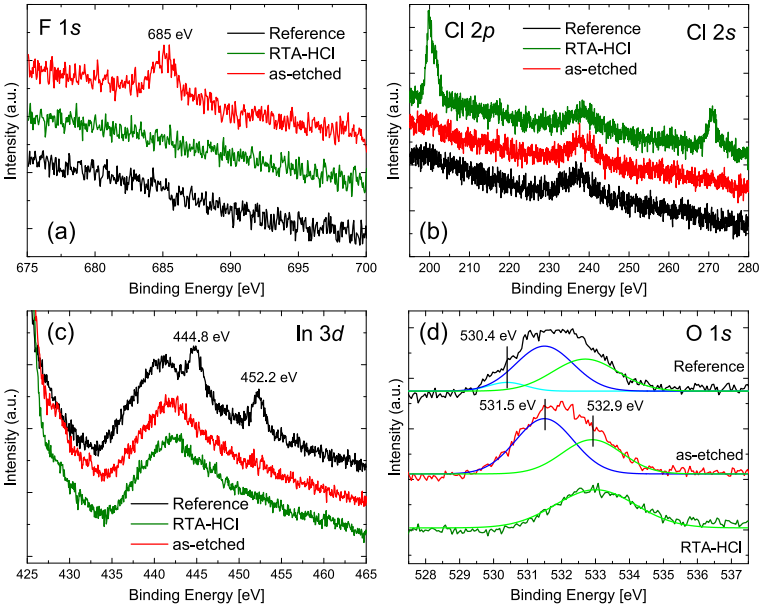

Figure 6.17: **(a)** F 1*s* spectra, **(b)** Cl 2*p* and Cl 2*s* spectra, and **(c)** In 3*d* spectra are shown for the reference, etched and RTA-HCl treated samples. **(d)** O 1*s* spectra and peak deconvolution into three components for different samples. The as-etched spectra are after removing the SiO_2 masking layer using HF.

Ga_2O_3, while the higher binding energy is likely due to O-H bonding from OH species.[141–145]

It is seen that the RTA-HCl treatment has left no trace of the 531.5 eV peak, indicating the removal of gallium oxides. The suppression of the O 1*s* peak was not achieved by the thermal annealing process alone, as happened to be case with the HCl treatment alone (Fig. 6.16). From these considerations it would appear that HCl treatment outperforms thermal annealing, yet the combination of the treatments accomplish a better result as witnessed by the PL emissions. An explanation could be that the wet chemical treatment of HCl only acts on the surface of the nanopillars, while RIE-induced damage and contaminants in the interior of the structures remain unaffected. Thermal annealing on the other hand will also affect the interior of the nanopillars and have the possibility of out-diffusing contaminants, and in this regard it might have been advantageous to thermally anneal at higher temperatures.[114] This was not tested as we wanted to avoid annealing the samples at temperatures similar to or above the epi-layer growth temperature. The combination of thermal annealing and HCl treatment is therefore expected to first cure interior damages and out-diffuse contaminants to the surface, while the HCl treatment thereafter cures the surface.

6.2.3 Nanopillar size dependence

The damage curing technique of thermal annealing followed by HCl treatment was then applied to samples A-D, and their PL spectra following this treatment are recorded in Fig. 6.18(a). Compared to the as-etched spectra all samples demonstrate improved PL emission after the treatment. The integrated PL enhancements after nanopillar formation (post-ICP) and after the RTA-HCl treatment (total enhancement) are given in Table 6.1. The PL intensity is seen to increase from sample A to C, which is not a significant result considering that the active region fill factor increases from A to C due to diameter variations with a fixed pitch. In contrast, sample D with the largest fill factor demonstrates the lowest PL intensity. The inset of Fig. 6.18(a) shows a titled SEM view of sample D where most nanopillars are seen to be connected to neighbouring pillars. The connections can be expected to reduce the strain relaxation effects in the QWs, and therefore, despite having the largest fill factor, the PL intensity of D is the weakest amongst the different samples.

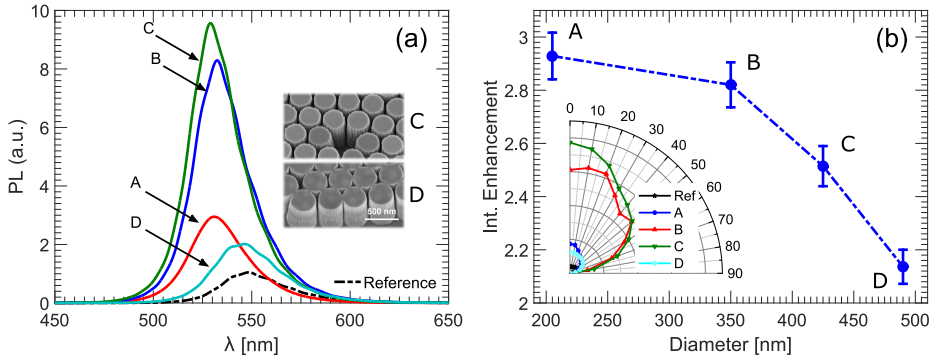

Figure 6.18: **(a)** PL spectra of the samples after RTA-HCl treatment. Inset shows SEM images of sample C and D. **(b)** The IPLE relative to the as-etched samples against nanopillar diameters. Inset is the angle-resolved PL for samples A-D.

Blue-shifts of the emission peaks are observed for all the etched samples relative to the reference indicating a reduced QCSE and strain relaxation. However, the amount of blue-shift decreases with increasing nanopillar diameter (see Table 6.1), implying a higher strain relaxation with smaller nanopillar sizes, in agreement with earlier investigations.[115] We notice here that sample D demonstrates a smaller blue-shift compared to the others, which gives another indication of, that strain relaxation effects are inhibited due to the connections between the nanopillars.

The integrated enhancement due to RTA-HCl treatment (relative as-etched samples) is shown in Fig. 6.18(b) for the various sizes of nanopillars present in different samples. The included errorbars are estimated from a 2 % uncertainty

Table 6.1: Sample characteristics and integrated PL ratios (IPLE).

Sample	Diameter [nm]	Emission CM blue-shift [nm]	Post-ICP IPLE	RTA-HCl IPLE	Total IPLE
A	205	17.9	0.88	2.93	2.59
B	350	14.4	2.61	2.82	7.39
C	425	12.5	3.19	2.51	8.03
D	490	5.8	0.95	2.14	2.03

in the PL intensities. The total enhancement factors relative to the as-grown sample are listed in Table 6.1. Sample C demonstrated an IPLE by a factor of 8 – the highest among all the samples. However, we notice from Fig. 6.18(b) that the damage curing treatment is more effective for smaller sized nanopillars. The enhancement for sample A with a pillar diameter of 205 nm is around a factor of 2.9, while that of the sample C is around 2.5. This trend could be due to larger amount of damage introduced by the RIE processes when forming nanopillars of smaller diameters and thereby etching larger portions of the GaN/InGaN material. In such a scenario the RTA-HCl treatment has a larger damage curing potential. However, since smaller nanopillars have a larger side-wall relative to the QW area, another explanation could be that the HCl treatment has the possibility of reaching a larger surface area of the QW side-walls relative the QW area on a single nanopillar. Larger nanopillars will have a smaller percentage QWs exposed from the side-walls of a single nanopillar and therefore less amount of damage can be cured by the HCl treatment.

The inset of the Fig. 6.18(b) shows the far-field emission patterns. As a figure-of-merit (FOM) for the directionality we estimate the percentage of power emitted inside a cone of 30° centred on the normal emission direction, which for the reference sample is 44 %. The FOM for samples B and C are 59 and 60 %, respectively, while sample A demonstrates the highest FOM of 65 %. Not only did sample D show the weakest PL emission, but also a poor directionality with a FOM of 55 %. Small pillar sizes seem to be favourable when high directionality is desired.

6.2.4 Dielectric passivation

We have previously discussed the importance of surface passivation when the active region is expected to be exposed in certain regions, such as pits and trenches. With the nanopillar structures, the active region is exposed to air on the side-walls which is expected to degrade the IQE due to surface states. Here we consider dielectric passivation coating for the nanopillars. However, as seen from the SEM images in Fig. 6.13, the nearly vertical side-walls will pose a challenge for the dielectric coating using PECVD method. We therefore designed a process where the PS nanospheres constitute the main etch-mask during the GaN/InGaN dry-etching process. This is achieved using the same process employed for the above considered samples, except with a thin SiO_2 layer whose only purpose is to provide the surface

condition necessary for PS nanosphere coating. The SiO_2 thickness used was 15 nm by PECVD prior to nanosphere coating. Furthermore the spheres in this case did not undergo a size reduction step using O_2 RIE, but where kept as deposited in their close-packed mono-layer configuration. Using the same ICP dry-etching recipe as described earlier, nanopillars where formed as shown in Fig. 6.19(a). The achieved side-wall angle was 65°. The contamination on the nanopillars seen in the figure is expected to come from the PS nanospheres, although we have not been able to confirm this. Surface treatment using HCl was performed on the nanopillars after the dry-etching process.

Having nanopillars with angled side-walls, a layer of SiN with a thickness of 15 nm was deposited on the surface using PECVD for passivation purpose. In addition, we also investigated Ag NPs for localized surface plasmon (LSP) coupling effects, which were formed by first depositing 15 nm Ag TF on the surface by e-beam evaporation, followed by thermal annealing. The formed Ag NPs are shown in Fig. 6.19(b), where it is seen that metal particles are formed on the side-walls. Besides the Ag NPs on the top *p*-GaN surface with average sizes around 130 nm, the particles on the side-walls have relatively small sizes ranging from 20 to 50 nm.

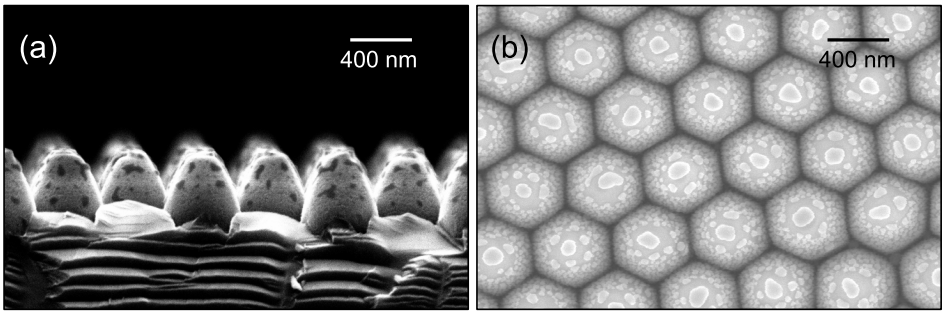

Figure 6.19: **(a)** Cross-sectional SEM image of the formed nanopillar structures when using only PS nanospheres as etch-mask during ICP dry-etching of GaN/InGaN. **(b)** Top-view of the nanopillar after Ag TF deposition and thermal annealing to form Ag NPs.

To investigate the passivation properties of the SiN-TF layer on the nanopillars we conducted PL measurements with sapphire-side excitation and emission detection. The spectra are recorded in Fig. 6.20(a), where the PL intensity after ICP-etching is seen to be enhanced relative to the as-grown emission, with an IPLE by a factor of 4.0, which is larger than what was obtained for sample C considered earlier. The results of HCl treatment was an IPLE by a factor of 2.5 and is comparable to the enhancement for sample C using the combined RTA-HCl treatment. The strongest enhancement is however obtained from the SiN-TF coating, which resulted in an IPLE of 3.1 relative to the HCl treated PL intensity. This is comparable to the results from the Section 5.1, where SiN-TF coating of the

defect-dominated top GaN surface resulted in an enhancement by a factor of 2.3. The surface passivation of SiN is expected to reduce surface states, and thereby improve the IQE of the active region inside the nanopillars. The total IPLE relative to the as-grown sample with HCl treatment followed by SiN passivation is seen to be a factor of 31.

On the other hand, Ag NPs are seen to have significantly suppressed the PL intensity as shown in Fig. 6.20(b), regardless of whether SiN passivation layer is present or not. The integrated PL is degraded by a factor of 15.3 due to the Ag NP relative to the HCl treated emission. However, with the SiN layer, the suppression is by a factor of 2.7 relative to the SiN-TF coated nanopillars. This is expected from metal NPs in contact with the QWs on the nanopillar side-walls, where they introduce surface states degrading the IQE. The problem is mitigated by the SiN layer, although the result is still a degraded PL intensity. The PL suppression is expected to be related to the small sized Ag NPs which have a large absorption. This is similar to the situation observed previously with Ag NPs on the top GaN surface, where particles with dimensions below 100 nm resulted in PL suppression.

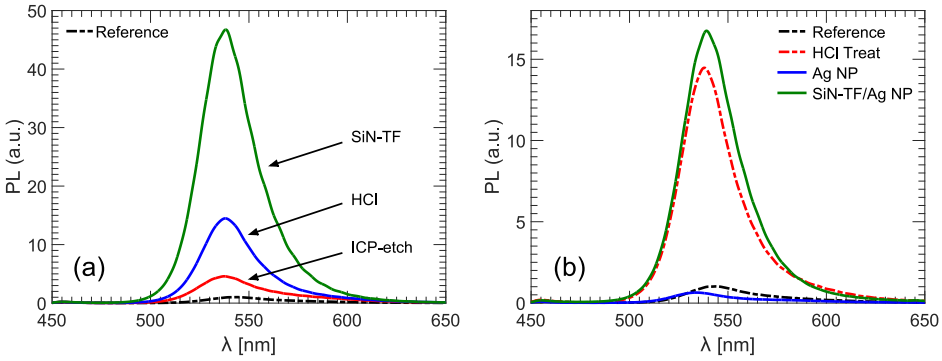

Figure 6.20: **(a)** PL spectra showing the effects of SiN-TF coating after HCl treatment. **(b)** PL spectra after formation of Ag NPs on nanopillars without and with SiN-TF coating (solid lines) compared to the as-grown sample emission and the HCl treated nanopillar structure (dashed lines).

6.2.5 Conclusions

We fabricated nanopillar structures on GaN/InGaN MQW LED using nanosphere lithography, and investigated the optical properties of different sized nanopillar structures. We could confirm that post-RIE damage treatment is critical for the optical performance of the LED, and in addition found that by combining two damage treatment methods, i.e. thermal annealing and HCl treatment, the PL improvement is better than either of them separately. The order of these treatments is also of significance, with RTA-HCl resulting in a better performance than HCl-RTA. By using thermal annealing followed by HCl acidic treatment an enhancement by a factor of 8 could be obtained relative to the as-grown sample. We also found that the RTA-HCl treatment was more effective for samples with smaller nanopillar diameters, i.e. when more of the active region had been etched away.

Passivation by SiN is seen to enhance the PL by an additional factor of 3 compared to the thermal and chemical treatments, which might be a necessary step to prevent degradation of the PL intensity over time due to surface oxidation. Using Ag NPs to provide LSP coupling and enhance the IQE did not yield the desired results. The PL was seen to be quenched as a results of the NPs, and the problem was due to the NP sizes.

CHAPTER 7

Towards electrically driven SP-LED

Until this chapter, we have applied and characterized plasmonic metal nanoparticles using optical pumping, i.e. photoluminescence (PL) measurements. Real devices, however, operate with electrical current injection, which has to be considered in the design of surface plasmon (SP)-LEDs. The implementation will depend on whether a thin or thick *p*-GaN epi-structure is used, and the device fabrication process can be more complicated than that for conventional LEDs. We will in this chapter review the methods for fabricating electrically driven LEDs with surface plasmonic compatibility, and present a design that can be used with thin *p*-GaN epi-structures where the SP-metal can be coated on the *p*-GaN surface.

7.1 Device fabrication

7.1.1 SP-LED devices

We have previously discussed SP-LED designs for conventional LED epitaxial structures in Section 3.1, where one of the possibilities was to embed SP-metals inside the epitaxial layers. Examples included metal deposition before the epitaxial growth of the active region, i.e. in the *n*-GaN layer,[40,48] or even after the active region growth, i.e. inside the *p*-GaN layer in close proximity to the quantum-wells (QWs).[46,47,146,147] With such designs, the fabrication process for an electrically driven SP-LED device would be similar to that of a conventional LED. However, the interruption of the growth process and the risk of chamber contamination from metallic particles may not be a possibility in industrial processes for LED epi-wafer growth. This has lead researchers to investigate alternative ways of applying SP-metals with electrically driven devices.

Using a conventional LED epi-structure, one option is to etch the *p*-GaN to deposit SP-metal in the near-field of the QWs similar to the investigations of Section 3.1. Cho *et al.*[148] demonstrated this concept with micro-holes in *p*-GaN, where they employed Ag thin film (TF) (similar to sample D in Fig. 3.6) to act as SP-metal and current spreading layer (CSL). The design showed 45 % electroluminescence (EL) enhancement. Nanohole pattern on *p*-GaN and a subsequent deposition of Ag TF was fabricated by Chen *et al.*,[84] where the Ag TF also

served as a CSL on *p*-GaN. They obtained a 75 % EL enhancement relative to a device without nano-pattern and with Ag TF as CSL. These implementations can only be used for flip-chip LEDs, where the emission is from the sapphire-side, as the SP-metal will function as a reflector.

Still considering conventional LED epi-structures, another approach which has been investigated, is to etch through the active region similar to the situation considered in Chapter 6, where metal particles can be embedded to achieve SP-QW coupling. This was demonstrated by Lee *et al.*[149] with micro-holes etched through active region from the *p*-GaN side. They passivated the side-walls with 50 nm SiO_2, and deposited synthetic Ag nanoparticles (NPs) and nano-wires in the micro-holes and on the *p*-GaN surface, where the purpose of the nano-wires was to improve current spreading. The CSL on *p*-GaN consisted of indium tin oxide (ITO), which was deposited before the micro-hole pattern definition. With this configuration, they could demonstrate a wall-plug efficiency improvement by 150 % at 100 mA driving current.

Etching nanopillar structures through the active region requires a more complicated device fabrication process for electrical injection. Nonetheless, this method has been applied for SP-LED applications by Zhu *et al.*,[62] who formed nanopillars using self-assembled Ni NPs as etch-mask. They used 10 nm HfO_2 as side-wall passivation before depositing 9 nm Ag TF followed by thermal annealing to form Ag NPs in the vicinity of the QWs. To prevent *p*-contact connection with *n*-GaN, spin-on-glass was applied in the regions between the nanopillars. Due to the improved carrier recombination rate from localized surface plasmon (LSP) coupling, the device demonstrated an improved modulation bandwidth. However, the PL and EL intensities were degraded due to the Ag NPs.

Output power enhancement using Ag NPs with nanopillar structures was demonstrated by Yun *et al.*,[150] where nanopillars were formed using self-assembled Ni NPs. They employed synthetic SiO_2-coated Ag NPs with diameters in the range of 50-80 nm, which were spin-coated to fill up the region between the nanopillars for insulation and LSP-QW coupling. The internal quantum efficiency (IQE) was shown to be enhanced from 11 % to 14 %. On the other hand, the EL intensity was improved by almost a factor of 2, which was demonstrated using on-wafer electrical characterization with In contact. The nanopillar LED device with and without Ag NP, however, displayed poor IV properties with operating voltage above 8 V.

Thin *p*-GaN designs for LED epi-structures can enable SP coupling from metallic TFs or NPs deposited on the as-grown *p*-GaN surface. Such a design was investigated by Yeh *et al.*,[54] who demonstrated 50 % EL enhancement due to an Ag TF using LED epi-structure with 70 nm *p*-GaN. The CSL consisted of a thin Ni/Au grid-structure where SP-metal could couple with active region in the areas without Ni/Au. Later on, the same group demonstrated that with a 60 nm *p*-GaN structure and Ag NPs in the regions between the Ni/Au grid, an EL enhancement up to a factor of 2 could be obtained.[59] They also claimed that the efficiency-droop

of LEDs could be reduced due to SP coupling by using this configuration.[60,151] Common for all their devices, was the active region, which consisted of a single QW. With a single QW the effects of SP coupling can more easily be analysed, though it is more common to employ three or more QWs for the active region of GaN/InGaN LEDs.

We will in this chapter analyse a similar grid pattern for the *p*-contact and apply it for an LED with 30 nm *p*-GaN thickness for SP coupling with Ag NPs in the regions between the grid. The active region of the LEDs in our case consists of five QWs.

7.1.2 Fabrication process

The LED device-fabrication process presented here is equally applicable to conventional LEDs. The process flow overview is shown in Fig. 7.1, which is divided into two categories – mesa structure formation, and metallizing ohmic-contacts. The mesa height should be such that the *n*-GaN layer will be exposed for *n*-contact deposition. Photolithography was used for pattern definition on AZ photoresist (PR). The PR variant used in all cases was the AZ5214E, which for the mesa pattern was used a positive tone resist, while in the case of metallization an image reversal step was employed to change the polarity of the PR. The illustrated process flow can both be used for conventional LED and SP-LED devices.

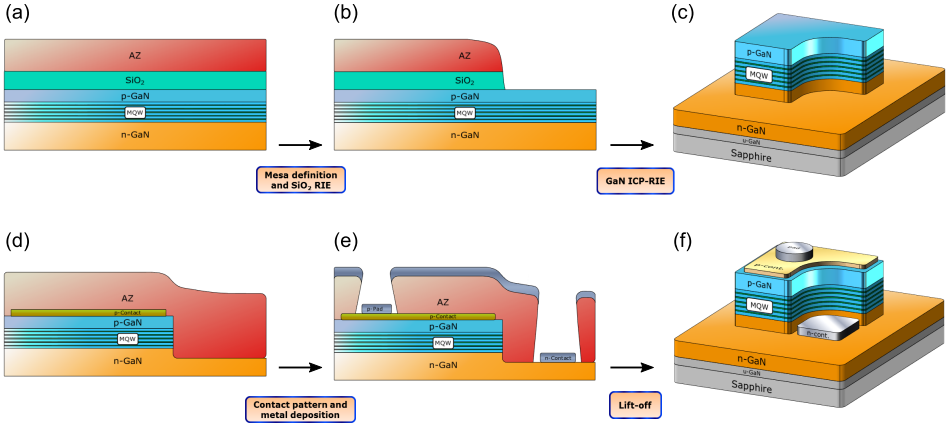

Figure 7.1: Device fabrication process flow for GaN/InGaN LEDs. **(a)-(c)** Mesa structure definition and **(d)-(f)** metallization lithography.

In order to achieve SP-metal compatibility we consider a *p*-contact design which does not cover the entire mesa surface. A conventional (type A) and an SP-metal compatible (type B) *p*-contact design are shown in Fig. 7.2(a) and (b), respectively. In general the purpose of the shown *p*-contact is to function as a CSL. The mesa

structure, n-contact and p-pad have the same dimensions in both cases. For type B the grid has a period of 20 μm and the ridges have a width of 5 μm. The design for SP-metal deposition in the areas between the ridges is shown in Fig. 7.2(c,d), with each unit of SP-metal having a dimension of 11×11 μm. The current spreading between the grid arms is expected to occur in the p-GaN layer.

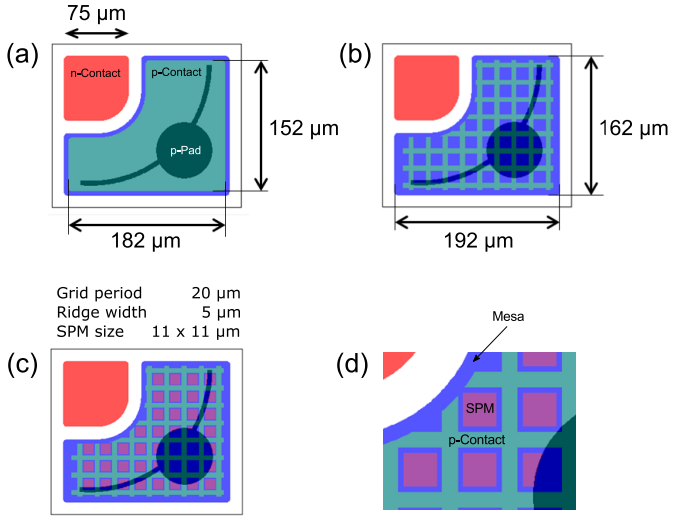

Figure 7.2: Top-view of the mask patterns for the mesa, n- and p-contact, as well as p-pad. The p-contact has two different designs, with **(a)** type A completely covering the mesa surface and **(b)** type B consisting of a grid-structure. **(c)** SP-metal (SPM) combined with type B p-contact in a non-overlapping configuration and **(d)** a zoomed view.

7.1.2.1 Mesa definition

For the mesa etching process it is advantageous to use SiO_2 as etch mask during the inductively-coupled plasma (ICP) dry-etching of GaN, instead of AZ PR. We used 300 nm SiO_2 obtained by plasma-enhanced chemical vapour deposition (PECVD), which was then surface treated with HMSD gas to promote PR adhesion. AZ5214E PR was then spin-coated with a thickness of 1.6 μm, followed by hard-baking at 90 °C. The mesa pattern was defined on the PR and developed using a solution of 1:5 AZ351:H_2O. The SiO_2 was etched using CHF_3/N_2 reactive-ion etching (RIE) process with the recipe described in the previous chapter. Before etching GaN, the PR was removed using O_2 plasma ashing, and thereby leaving only the SiO_2 layer on top. Using only AZ resist during the GaN etching, would have involved fewer processing steps, however, the PR was seen to leave traces on the mesa surface even after acetone cleaning as shown in Fig. 7.3(a). Although the PR traces could

be removed by O_2 plasma ashing, another disadvantageous was the small side-wall angle which was around 30-40° with the horizontal surface.

The mesa structure obtained by using SiO_2 as etch-mask is shown in Fig. 7.3(b). The SiO_2 was removed by wet-etching using 5 % HF. The mesa height could be measured by a profilometer, and was in a range from 500 to 600 nm which is enough to expose the *n*-GaN layer.

It is at this stage important to perform surface treatments to account for the ICP-induced damage to the GaN surface which is known to degrade the electrical performance.[49,50] Examples of surface treatments that have been demonstrated to improve the device performance include sulfur,[152] HCl[99,152] and thermal annealing.[104] In our situation we used the same surface treatment as that employed for the nanopillar structure in Chapter 6, i.e. the RTA-HCl combination.

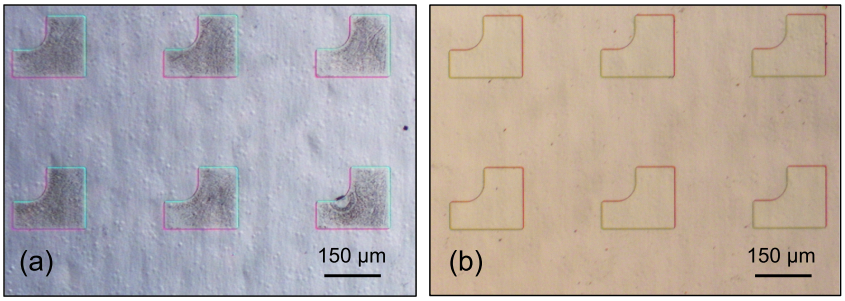

Figure 7.3: **(a)** Microscope view of the mesa pattern after ICP dry-etching of GaN using AZ5214E PR as etch mask. **(b)** The mesa structure using SiO_2 as etch mask. The SiO_2 has been removed in the picture.

7.1.2.2 Ohmic contacts

In the photolithography process for the ohmic-contact pattern, a PR image reversal was used to develop the un-exposed areas for metal deposition, i.e. the areas for *p*-contact, *n*-contact and *p*-pad as shown in Fig. 7.2. Image reversal is in general achieved through a reversal-bake step, e.g. at 120 °C, after the UV exposure, which makes the exposed areas inert and insoluble in the developer. A flood exposure following the reversal-baking will make the areas which were not exposed during the first exposure, soluble in the developer.

For *p*-contact of type B, the grid-structure posed a challenge during the developer step due to the poor adhesion of the AZ5214E PR to GaN. In the mesa pattern lithography, the PR was coated on top of an HMDS treated SiO_2, which could not be used in our case of ohmic-contact lithography. We used a commercial adhesion promoter called Surpass 3000 (from DisChem, Inc.), which was applied to the surface by immersing the sample for 30 sec in the solution and then rinse with de-ionized water. Nonetheless, the dimensions of type B *p*-contact made it

difficult for the PR to adhere to the surface in the grid-patterned regions. An example of PR adhesion failure with different development durations is shown in Fig. 7.4. Unlike PR on a layer of SiO_2, where an over-etch results in size reduction, the structures are seen to be peeled off. It was therefore important to develop just enough to reach to the GaN surface and avoid over-development.

It is also equally important to fully develop the resist. If a thin layer of PR remains, the ohmic-contact performance will be degraded. The usual way to ensure no residual PR layer remains, is to apply O_2 plasma ashing after PR development, however, this step will oxidize the GaN surface also leading to a very poor ohmic-contact.

Once the *p*-contact area is developed, another surface treatment step can be performed before metal deposition to reduce the contact resistance. To remove surface oxides that could have been introduced during lithography step, a 5 % HF treatment was applied for 1 min, which did not affect the PR pattern. It is imperative that the surface is as clean as possible before the ohmic-contact deposition to minimize contact resistance.

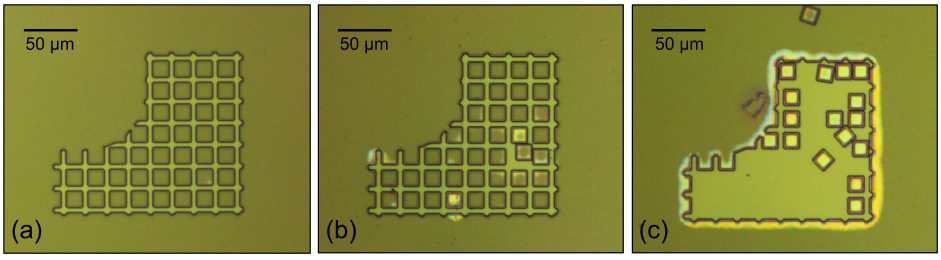

Figure 7.4: Pattern formation for type B *p*-contact after **(a)** 40 sec, **(b)** 50 sec, and **(c)** 60 sec duration in the developer.

For lateral LED design with light emission from the *p*-GaN side a transparent CSL is desired. High transparency in the visible region in addition to conductivity is provided by transparent conductive oxides (TCOs). A widely-used example of TCO on *p*-GaN functioning as a CSL is ITO, which has been reported to have excellent transparency (above 90 % transmittance) at green emission wavelengths.[153–155] Other examples of TCO include doped zinc oxide (ZnO) films, where Ga-doped ZnO (GZO)[156] and Al-doped ZnO (AZO)[157] have been demonstrated in GaN LED applications.

Metal contacts such as Ni/Au also provide low contact resistance as well as a high transparency (up to 80 % transmittance) when oxidized on *p*-GaN.[158] One way which has been shown to improve the transmittance has been through a Ni/Au grid-structure[159] similar to the one shown in Fig. 7.2(b). Such a grid-structure has also been applied by Yeh *et al.*[54] for SP-LED device designs.

We investigated both ITO and Ni/Au as *p*-contact. The thickness for Ni/Au was 10/40 nm deposited by e-beam evaporation, which following the lift-off pro-

cess was annealed at 525 °C for 5 min in O_2 atmosphere for oxidization. ITO was deposited by RF sputter-deposition (using Lesker Sputter-system CMS 18) with 75 W power and 3 mbar pressure. The obtained thickness was about 180 nm. After deposition and lift-off, the ITO was thermally annealed for 8 min in N_2 atmosphere to improve its conductivity and transparency. The optical properties of the ITO were investigated by transmittance measurements. The as-deposited ITO had poor transparency as shown in Fig. 7.5(a). Thermal annealing did improve the transparency for temperatures above 350 °C. The transmittance spectra of ITO on silica glass obtained from the different annealing conditions are shown in Fig. 7.5(b). The optical transparency is significantly improved after 350 °C annealing. Although the transmission levels appear similar for 350 and 600 °C annealing, there is a slight difference and the one annealed at 600 °C appear more transparent than the rest as seen from the photograph in Fig. 7.5(a).

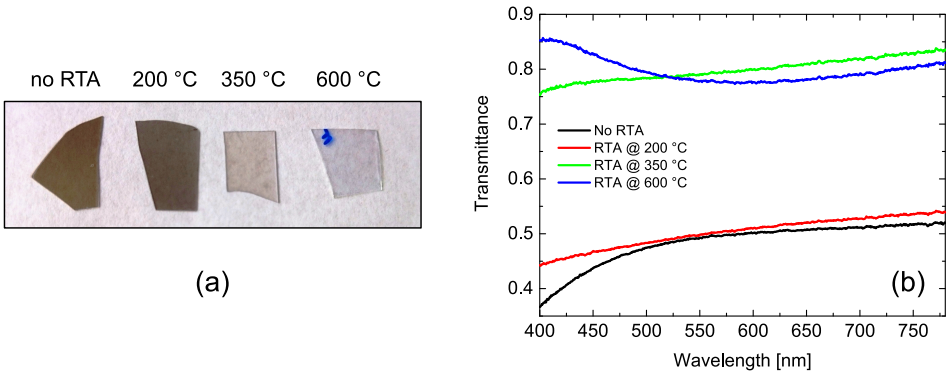

Figure 7.5: **(a)** Silica glass samples with 180 nm ITO on top gone through different annealing conditions, and **(b)** their transmittance spectra measured from the ITO-side of the samples.

Lift-off difficulties were experienced with the grid-structured ITO layer as shown in Fig. 7.6(a) despite ultrasonic treatment. On rare occasions, it was necessary to gently use cotton swabs to complete the lift-off. A successful lift-off is shown in Fig. 7.6(b). The difficulties were related to the thickness of the ITO layer, as it was not experienced for the Ni/Au with a total layer thickness of 50 nm.

Regarding ohmic-contacts for *n*-GaN, several metal combinations exist, including, but not limited to, Cr/Au,[160,161] Cr/Ni/Au,[162] Ti/Au,[163] and Ti/Al/Ti/Au.[164–166] We used non-alloyed Ti/Au as *p*-pad on ITO and Ni/Au, i.e. no thermal annealing was performed on the Ti/Au metal combination. For the *n*-contact we investigated both Ti/Au and Ti/Al/Ti/Au. The latter mentioned was annealed at 525 °C for 5 min in N_2 atmosphere, although it has been suggested that non-alloyed Ti/Al/Ti/Au can be used if a proper surface cleaning is performed.[166] The layer thicknesses of Ti/Au was 30/100 nm, while that of Ti/Al/Ti/Au was

10/100/20/100 nm. The advantage of using Ti/Au as n-contact is that the p-pad and n-contact can be deposited simultaneously, saving time and fabrication cost. The result of using Ti/Au and ITO in the final device phase is shown in Fig. 7.6(c) and (d) for device type A and B, respectively.

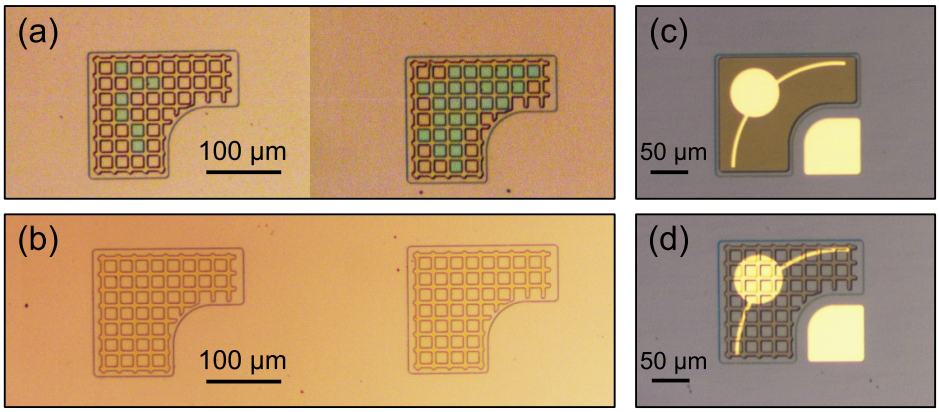

Figure 7.6: **(a)** Lift-off difficulties for 180 nm ITO with grid-structure. The green square regions are ITO on AZ resist. **(b)** Successful ITO lift-off. **(c)** Type A and **(d)** type B p-contact designs for the final device with ITO as p-contact and Ti/Au as p-pad and n-contact.

7.1.3 Conclusions

The presented fabrication process flow can be equally applied for a conventional and thin p-GaN LED for SP coupling. The challenge lies in ensuring a clean GaN surface prior to metal deposition to achieve the lowest possible contact resistance between the metal-semiconductor junction. A residual resist layer will inevitably degrade the device performance, and steps must be taken to ensure the complete development during the photolithography step. This is a critical aspect regarding the grid-structured p-contact where the resist development time cannot be longer than necessary.

7.2 Device performance

7.2.1 Electrical characterizations

Four different device samples (C1-4) are investigated in this section where the p-contact consists of either 180 nm ITO or 10/40 nm Ni/Au, and the n-contact consists of either 10/100/20/100 nm Ti/Al/Ti/Au or 30/100 nm Ti/Au. The p-pad for all the samples consists of 30/100 nm Ti/Au. The details are summarized in Table 7.1.

The IV-characterizations for devices of type A and B in case of Ni/Au p-contact is shown in Fig. 7.7(a). Although the performance of the fabricated devices is far from what can be achieved for GaN based LEDs using Ni/Au in terms of forward voltage,[159] the behaviour of type A and type B devices are seen to be similar. Furthermore, n-contacts based on Ti/Al/Ti/Au (C1) and Ti/Au (C2) do not show a noticeable difference in IV-characteristics. The large forward voltage is due to a high contact resistance, and can be improved by optimizing the fabrication process. The process before p-contact deposition is the most critical part, but was not optimized for this batch of samples in terms of a proper surface treatment.

For samples C3 and C4 which is using ITO as p-contact, there is a difference between type A and B, with A performing worse than B as shown in Fig. 7.7(b). In general the ITO is performing worse than the Ni/Au p-contact. This is related to the sputter deposition of ITO which has to be investigated and optimized to improve the conductivity of the ITO layer. The difference between Ti/Au and Ti/Al/Ti/Au is in this case more noticeable with Ti/Au having the best performance. In case of Ti/Au the metallization of n-contact and p-pad on ITO consisted of a single lithography step as opposed to the two steps with Ti/Al/Ti/Au n-contact. Hence, it is expected that the contact between ITO and Ti/Au is degraded due to the separate n-contact lithography. It is therefore more beneficial to use Ti/Au as the n-contact and p-pad and combine their deposition into a single step.

A difference between type A and type B devices is the contact between the p-pad and its underlying surface, which in case of type A entirely consists of either Ni/Au or ITO. In case of type B, however, the p-pad is also in direct contact with the p-GaN surface as seen in Fig. 7.6(d). This does not appear to show a noticeable difference when the p-contact is Ni/Au, but with ITO, the performance

Table 7.1: Device details.

				Current at 6 V [mA]	
Sample	p-Contact	n-Contact	p-Pad	Type A	Type B
C1	Ni/Au	Ti/Al/Ti/Au	Ti/Au	22.5	23.0
C2	Ni/Au	Ti/Au	Ti/Au	22.5	29.9
C3	ITO	Ti/Al/Ti/Au	Ti/Au	52×10^{-3}	0.16
C4	ITO	Ti/Au	Ti/Au	112×10^{-3}	0.23

is clearly degraded when the ITO completely separates the *p*-pad from the *p*-GaN surface as is the case with type A devices.

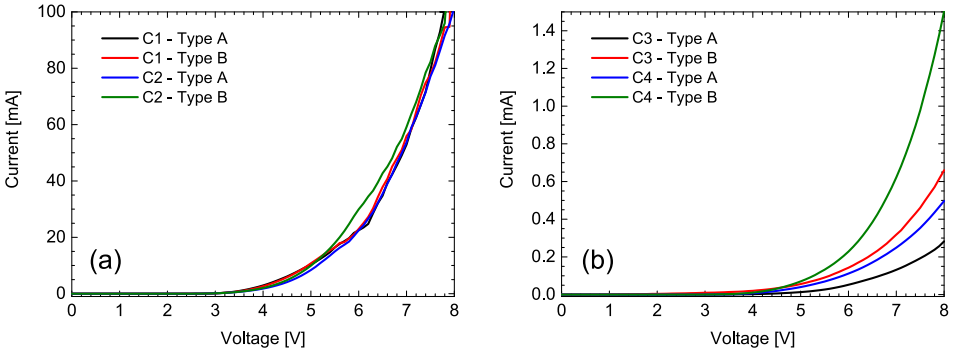

Figure 7.7: IV relations for device type A and B using **(a)** Ni/Au, and **(b)** ITO as *p*-contact.

Leakage currents are obtained by driving the LED in reverse bias, and the results are shown in Fig. 7.8 for different samples and device types. The type of the *p*-contact does not appear to be the cause behind the variations between the samples, rather this is related to the property of the individual devices. Sample C3 with ITO and Ti/Al/Ti/Au shows a relatively large leakage current compared to C4 with ITO and Ti/Au. Whether this is due to the contacts or the processing and its impact on the *pn*-junction is difficult to determine. Leakage current can in general be associated with the *pn*-junction quality and the epi-structure, and in this investigation all the samples are from the same epi-wafer.

The *n*-contact resistance can be estimated through an *n*-*n* IV measurement. In Fig. 7.9, this relation is shown for the two *n*-contact metal combinations used,

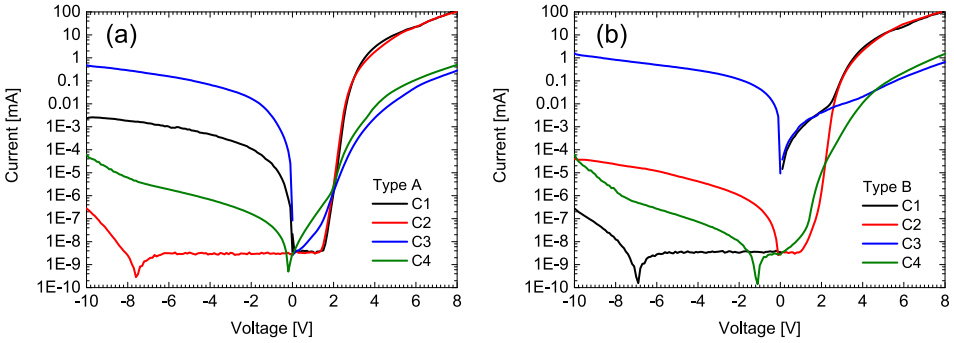

Figure 7.8: IV relations for the different samples including (absolute value of) the leakage current for device **(a)** type A, and **(b)** type B.

both of which are showing ohmic behaviour. The resistance values obtained are 15 Ω and 40 Ω for Ti/Au and Ti/Al/Ti/Au contacts, respectively. This shows that given the fabrication process steps, the Ti/Au has a better performance compared to the four layered metal combination as an n-contact metallization.

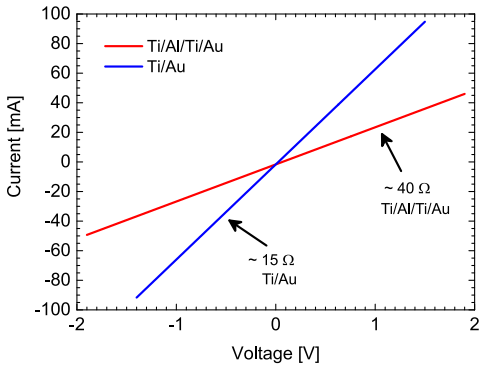

Figure 7.9: The n-to-n IV relation for Ti/Al/Ti/Au and Ti/Au n-contacts.

7.2.2 Electroluminescence

The EL of the samples were characterized from the polished sapphire-side. The EL spectra for samples C1 and C2 at 3 V forward voltage are shown in Fig. 7.10(a). The low intensity of the sample C1-A is due to a poor IV-relation demonstrated by the given chip which is not a characteristic of the p-contact type. Considering sample C2 (with Ti/Au n-contact) the EL intensities for p-contact type A and B are seen to be on a comparable level, which is not a significant result when taking into account the similar IV-relations of these samples. The non-degraded emission intensity of type B compared to type A is an important aspect if type B design has to be implemented for SP-metal compatibility and SP enhancement.

EL intensities for the samples with ITO p-contact are shown in Fig. 7.10(b), which is driven at 6 V due to the poor IV-characteristics and the low EL intensity at 3 V. As expected from the IV-relations, the samples with Ti/Au n-contact (C4) perform better than the four layered metal combination. Type B devices show a higher EL intensity than type A, but this can be explained by the difference in IV-relation and the injected current at the given voltage levels.

Microscope images of sample C1 is shown in Fig. 7.11 illustrating the difference between type A p-contact and type B under 3 V bias voltage. The grid-structure is not seen to impede the current spreading and the emission is not limited to the area beneath the Ni/Au grid-structure. This suggests the current spreading inside the p-GaN layer, and allows for the possibility to employ this design with SP-metals between the p-contact. SP coupling would be meaningless without carrier generation under the area covered by the SP-metal.

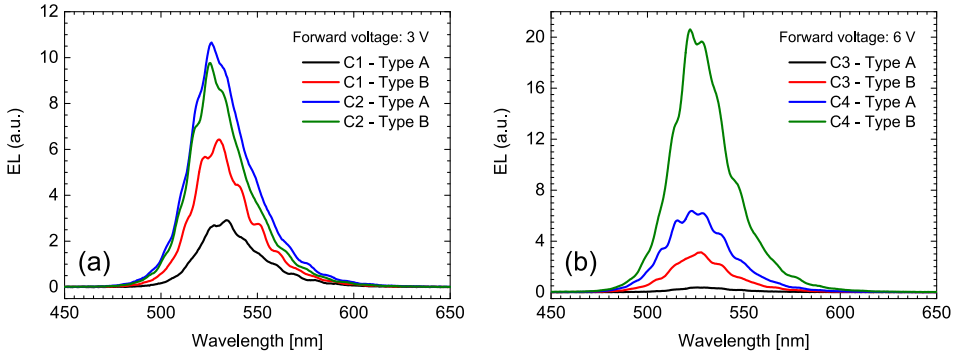

Figure 7.10: **(a)** EL spectra measured from the sapphire-side of the samples with Ni/Au *p*-contact under the same forward bias condition of 3 V. **(b)** EL spectra for the ITO *p*-contact samples driven at 6 V bias.

For the samples with ITO and Ti/Al/Ti/Au contacts, the difference between the emission from type A and type B device is shown in Fig. 7.12(a) and (b). When the ITO is totally covering the surface the current injection is seen to be concentrated in isolated regions exhibiting bright spots. In case of type B device where the Ti/Au *p*-pad is in direct contact with the *p*-GaN surface, the current

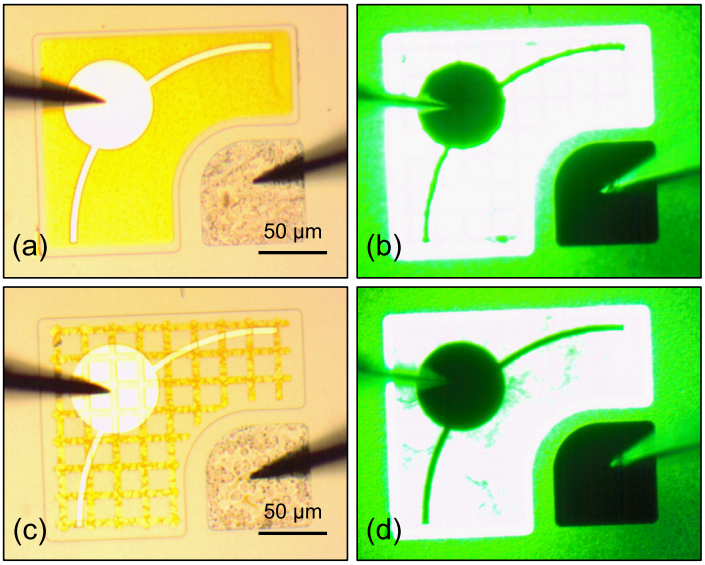

Figure 7.11: Sample C1 with Ti/Al/Ti/Au *n*-contact observed from the *p*-GaN side. **(a)** Type A device with and **(b)** its operation at 3 V bias. **(c)** Type B device and **(d)** its operation at 3 V bias.

spreading is seen to be better than type A, although certain areas (north from the pad) still have poor current injection.

The uniformity is seen to be improved for sample C4, both regarding type A and type B p-contact designs as illustrated in Fig. 7.12(c) and (d), respectively. The extra lithography process involved with sample C3 compared to C4, appears to have affected the contact resistance between the ITO and Ti/Au p-pad. The ITO undergoes an additional step of thermal annealing in relation with the Ti/Al/Ti/Au n-contact annealing at 525 °C. The lower n-contact resistance of Ti/Au, as seen in Fig. 7.9, is also expected to have a contribution to the improvement of C4 compared to C3.

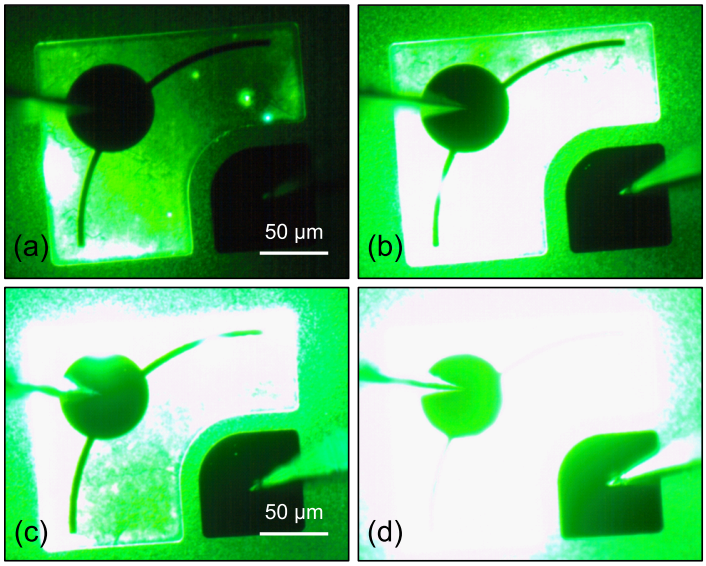

Figure 7.12: Operation of the samples with ITO p-contact at 6 V forward voltage observed from the p-GaN side. **(a)** C3-A, **(b)** C3-B, **(c)** C4-A, and **(d)** C4-B.

For a better comparison between the device types, the EL spectra are measured at equal driving current and is shown in Fig. 7.13. Except for the C1-B device, the samples show nearly identical emission intensities. For SP implementation it is necessary to avoid degrading the device performance compared to a conventional one due to a customized p-contact design, in order to reach the full potential of the emission enhancement from SP coupling. This is seen to be the case for sample C2 where the p-contact consists of Ni/Au, and the n-contact together with the p-pad are simultaneously deposited in a single lithography step. The degraded emission from C1-B might have been caused by the additional lithography resulting in an increased contact resistance between the p-pad and p-GaN.

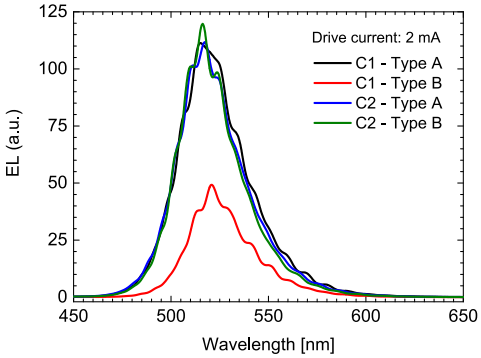

Figure 7.13: EL spectra for the Ni/Au *p*-contact samples at 2 mA driving current measured from the sapphire-side.

7.2.3 Thin *p*-GaN device

7.2.3.1 Electrical properties

The thickness of the *p*-GaN layer for the LEDs considered above has been 150 nm, but for a strong SP coupling as well as maintaining an efficient *pn*-junction, the thickness has to be around 30-70 nm as discussed previously. Therefore we also investigated an LED epi-wafer with a *p*-GaN thickness of 30 nm which allows for Ag NPs on the *p*-GaN surface to couple with the QWs. The metallization was identical to that used for sample C2, i.e. the *p*-contact consisted of 10/40 nm Ni/Au, while the *n*-contact and *p*-pad both consisted of 30/100 nm Ti/Au.

As part of the process optimization, we employed an additional acidic treatment step prior to *p*-contact deposition. It has been shown that GaN surface cleaning is crucial for obtaining low-loss ohmic contacts even in the absence of dry-etch damage.[167] With the previous samples, an HF treatment was done after the *p*-contact pattern development and before the Ni/Au deposition. For the thin *p*-GaN samples, following the HF treatment, a 10 min HCl treatment was applied to the *p*-GaN surface, which showed an improvement of the device performance. Fig. 7.14(a) shows the IV performance of the thin and thick *p*-GaN devices, where the former had an HF-HCl treatment while the latter (sample C2) only had an HF treatment. The leakage currents are shown in Fig. 7.14(b), where the it is seen that the thin *p*-GaN devices have a similar performance as those of the conventional epi-structure devices with leakage current below 1 nA.

A difference is observed in the IV characteristics between type A and type B *p*-contact designs. Unlike the 150 nm *p*-GaN LEDs, the 30 nm *p*-GaN LEDs also show a difference between the EL intensities of type A and type B designs as shown in Fig. 7.15. The difference is more pronounced as the injection current is increased.

The difference between the plain and grid-structured *p*-contact can be attributed to insufficient current spreading in the regions between the Ni/Au grids

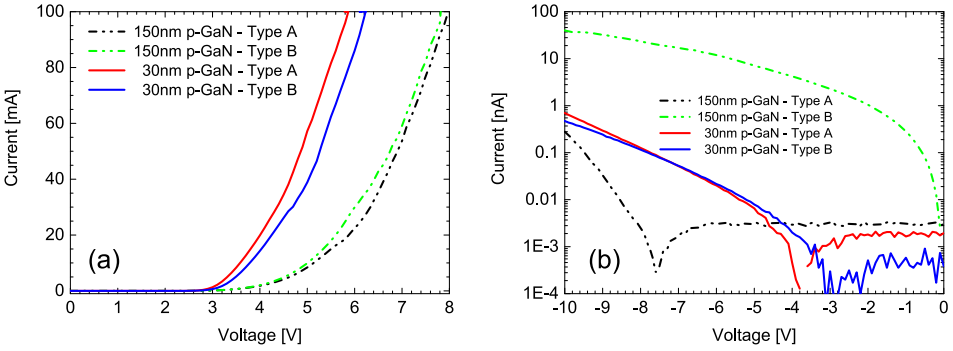

Figure 7.14: **(a)** Measurement of IV characteristics of thin p-GaN (solid lines) compared with thick p-GaN (dashed lines) LED devices for type A and type B p-contacts. **(b)** Leakage current measured up to a reverse bias of 10 V.

due to the thin p-GaN thickness. The current spreading capabilities of the thin and thick p-GaN epi-structures are illustrated in Fig. 7.16. The light emission from the 150 nm p-GaN LED is seen to be uniform across the mesa structure, while the emission from the 30 nm p-GaN LED is seen to be concentrated beneath the Ni/Au grid. This example shows that if the p-GaN thickness is too small, current spreading will not occur to the region between the p-contact grid-structure, and this is a detrimental effect to SP coupled LED operation.

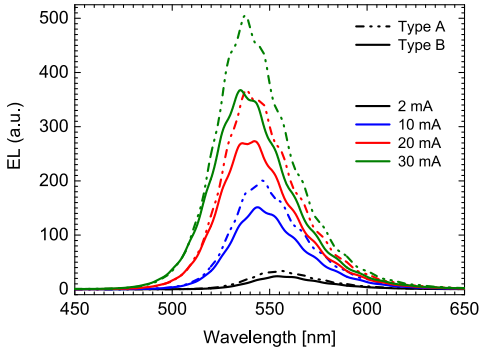

Figure 7.15: EL spectra measured from the sapphire-side for the thin p-GaN device for type A and type B p-contact designs.

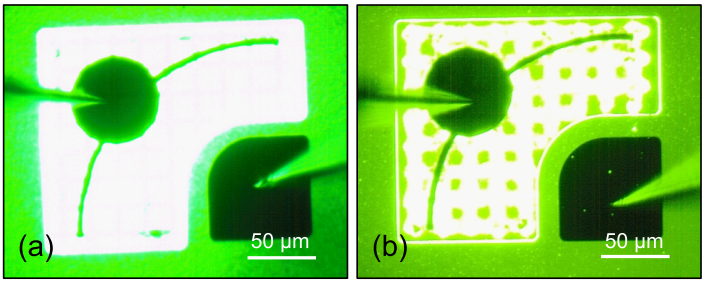

Figure 7.16: Operation of LEDs with Ni/Au *p*-contacts of type B on an epi-structure with **(a)** 150 nm *p*-GaN and **(b)** 30 nm *p*-GaN, observed from the *p*-GaN side.

7.2.3.2 Device with Ag nanoparticles

The design for Ag NP deposition between the Ni/Au *p*-contact grid was illustrated in Fig. 7.2(c). By going through an additional photolithography process using AZ5214E PR with image-reversal, the Ag-pattern was defined on some of the type B devices available on the sample. The remaining type B devices were to be used as reference without Ag NPs. Prior to Ag deposition, the exposed *p*-GaN surface was coated by 15 nm SiO_2. The dielectric was deposited using reactive sputter-deposition (Lesker Sputter-system) with Si source and 30 % O_2 in Ar gas, 115 W power, and 6 mTorr pressure. This method was used due to restrictions of the PECVD system concerning metal contamination. After the SiO_2 deposition, 12 nm Ag TF was deposited by e-beam evaporation. Following a lift-off process of the SiO_2/Ag layer, the Ag TF was thermally annealed at 350 °C for 15 min in vacuum.

The IV characteristics of the sample gone through the Ag-pattern lithography process (including the SiO_2/Ag deposition, lift-off and thermal annealing process) were seen to be degraded even without Ag NPs. IV-curves for the devices without Ag NPs before and after the additional lithography step are shown in Fig. 7.17(a). The device with Ag NPs demonstrates an even lower performance.

The EL spectra measured from the sapphire-side for the type B devices with and without Ag NPs (after Ag lithography step) are shown in Fig. 7.17(b) at various current levels. The difference between the spectra is seen to be marginal. Considering the poor current spreading in the thin *p*-GaN observed in Fig. 7.16(b), it is difficult to expect an EL enhancement if none or insufficient amount of carriers exist beneath the Ag NPs to enable LSP-QW coupling.

The operation of the devices with and without Ag NPs are shown in Fig. 7.18 under equal current injection levels. The areas with Ag NPs are seen to be brighter compared to the device without Ag NPs, and the difference is larger for higher injection currents. This is the effect behind the small difference in EL intensity observed in Fig. 7.17(b). With high injection current, more carriers will flow into

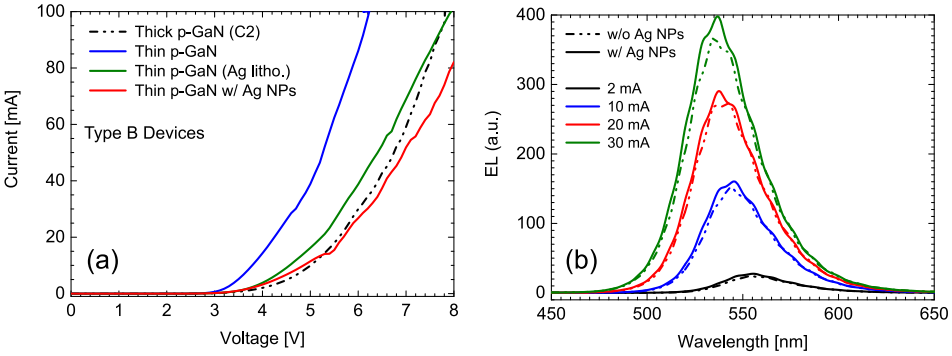

Figure 7.17: **(a)** IV characteristics of devices with grid-structured Ni/Au *p*-contacts showing the performance of thin *p*-GaN samples before and after Ag-pattern lithography, as well as the performance with Ag NPs. The IV-curve of the 150 nm *p*-GaN sample (C2) is also shown for reference (dashed line). **(b)** The EL spectra for type B devices after Ag-pattern lithography with (solid lines) and without (dashed lines) Ag NPs with various driving currents.

the region between the grids, and the Ag NPs are seen to provide an enhancement that elevates the emission between the grids up to the levels observed underneath the grid (compare Fig. 7.18(c) and (f)). The lift-off with SiO_2/Ag did not yield 100 % success-rate throughout the device surface, and the cross-marked sections in Fig. 7.18(d) are areas without Ag NPs. The dark regions observed in Fig. 7.18(f) seem to correspond with the cross-marked regions in (d) where Ag NPs are absent. This is a clear indication of the improvements by Ag NPs although to a very small degree as witnessed by the EL spectra.

7.2.4 Conclusions

We have analysed a specially designed *p*-contact CSL consisting of a grid-structure which allows for SP-metal deposition in-between the grid arms. For this purpose we considered two different *p*-contact types, including Ni/Au and ITO. Although the ITO transparency was improved by a thermal annealing process, the conductivity was seen to be worse than that of Ni/Au. To improve the ITO performance the sputter-deposition process has to be optimized.

With a conventional thick *p*-GaN LED, the performance of the grid-structure was similar to that of fully covering the *p*-GaN surface with the *p*-contact. However, employing an epi-structure with 30 nm *p*-GaN revealed a degraded performance of the grid-pattern due to a poor current spreading in the *p*-GaN layer. This was also believed to be the reason behind the absence of EL enhancement when Ag NPs were applied for LSP-QW coupling. Without electron-hole generation beneath the Ag NPs, LSP-QW coupling will not take place to improve the emission efficiency.

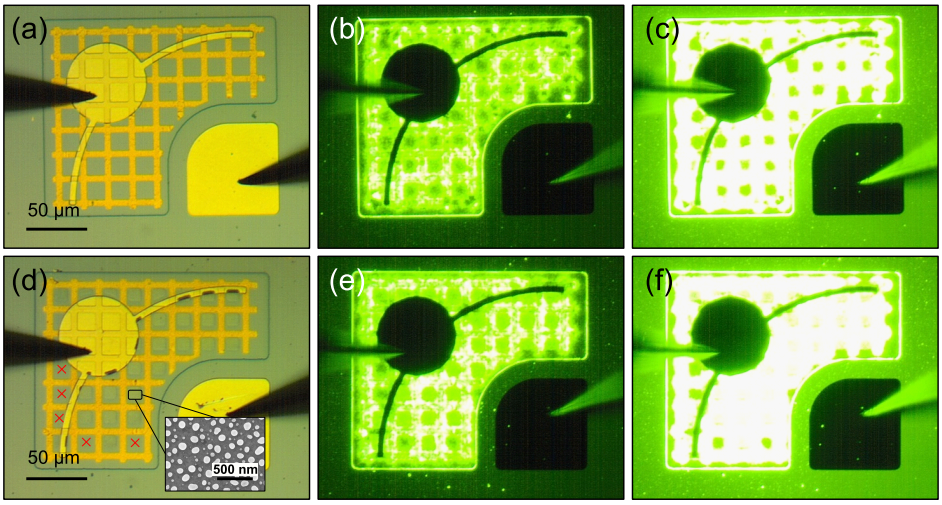

Figure 7.18: Thin *p*-GaN type B device operation after Ag-pattern lithography. **(a)** Device without Ag NPs and its operation under **(b)** 0.5 mA, and **(c)** 2 mA driving current. **(d)** Device with Ag NPs, where the crossed regions have no Ag NPs due to bad lift-off. **(e)** Device operation at 0.5 mA, and **(f)** 2 mA driving current.

CHAPTER 8

Conclusions and outlook

Surface plasmonics from metallic thin films (TFs) and nanoparticles (NPs) were applied to improve the low efficiency of InGaN semiconductor light-emitters at green emission colours – a topic which is being intensively researched in recent years. The main aspects of this technology investigated in this project include the surface plasmon (SP) coupling with the active region (Chapter 3), metal NP radiative properties (Chapter 4), enhancement from patterned dielectric combined with SP coupling (Chapter 5), SP compatible nanopillar LED and surface treatments (Chapter 6), and design for an electrical driven device with SP compatibility (Chapter 7). The key results of the findings are summarized in the following.

8.1 Surface plasmon coupling

Considering a conventional LED epi-structure with a *p*-GaN thickness around 130 nm, the surface was partially etched as a hole-pattern to allow for the SP-metal deposition in the near-field of the active region consisting of five quantum-wells (QWs). The photoluminescence (PL) was seen to be quenched with Ag NPs placed 30 nm from the top-most QW inside nanohole structures, while an enhancement was obtained when placed 80 nm away, contrary to expectations. The PL quenching was not observed when micro-hole structures were considered. These findings suggested that if NPs are desired in the near-field of the QWs, their sizes have to be well controlled to achieve SP enhancement. Our hypothesis is that the small-sized Ag NPs (on order of 50 nm in diameter) which are formed inside the nanohole structures, have a large absorption from dissipation inside the metal compared to larger particles. This will affect the energy coupled into the localized surface plasmon (LSP) mode from the electron-hole pairs, which is dissipated inside the metal instead of being radiated.

One aspect which can be investigated in the future, is to passivate the surface of the etched region to eliminate the creation of surface states near the QWs. Additionally, the deposition process of Ag inside the nano-structures has to be such that small sized NPs are prevented from forming inside the nanoholes, which is mainly the case when thermal annealing is employed to smooth-out the NP shape.

The NP size dependence was also analysed on an LED epi-structure with a *p*-GaN thickness of 30 nm, using self-assembled Ag NPs from thermal annealing. Based on temperature-dependent PL measurements, the internal quantum efficiency (IQE) enhancement due to the Ag NP coating could be investigated. It

was observed that the PL enhancement was larger than the IQE enhancement which could be attributed to light extraction efficiency (LEE) improvement due to the NPs on the semiconductor interface. The largest IQE enhancement was attained from the largest NPs considered, and it was also demonstrated that the lower as-grown sample IQE is, the higher the enhancement is from Ag NPs. This is a desirable feature of SP coupling for low-efficiency light-emitters, and has been theoretically investigated.[63]

8.2 Nanoparticle radiative efficiency

Motivated by the different enhancing capabilities of NPs, we investigated various sizes of Ag NPs formed on a dielectric layer coated on the top GaN surface. Having a 15 nm SiN would allow for LSP coupling with the QWs due to the 30 nm distance between the GaN surface and the active region. Numerical simulations were employed to analyse the observed features from the PL measurements. It was found that the scattering and absorptions cross-sections of NPs on GaN or GaN/SiN substrate, has an important role in determining whether the LSP coupling will enhance or degrade the emission.

The radiative efficiency of LSP modes is an important parameter to keep in mind when designing NPs for LSP-QW coupling. If the NPs cannot radiate the coupled energy from the QWs, the IQE will not be enhanced. Therefore, if absorption inside the metal is to be avoided, particles with a large scattering cross-section are required. The latter was seen to depend on the substrate.

8.3 Patterned dielectric

Further analysing the effects of dielectric TF coating, it was seen that a thin SiN could improve the emission when coated on the GaN surface. The enhancement could be attributed to the passivation aspect of SiN, as parts of the active region were exposed to air in pit and trench defects observed from the samples investigated.

Fabricating nano-rod (NR) structures on the dielectrics revealed a large enhancement of the emission which could be attributed to LEE enhancement. By using thin dielectrics of 20 nm thickness, the heights of the NRs could allow for LSP-QW coupling when Ag NPs were deposited on top. This configuration allowed us to obtained both LEE and IQE enhancement.

Since the particle sizes in this work, could only be partially controlled through the thickness of the pre-annealed Ag TF, it is desirable to employ advanced nanolithography to fabricate Ag NPs with a fixed size. Densely spaced NPs with an optimized size will have the potential of providing a larger IQE enhancement. By also controlling the spacing the between NPs, grating structures can be designed to improve the light out-coupling from the NPs.[73]

8.4 Nanopillar LED

Commercial LED epi-structures usually have a *p*-GaN thickness around 150 nm, which is too large for efficient SP-QW coupling, but needed for efficient *pn*-junctions and current spreading. Nanopillar structures were therefore fabricated by etching through the QW active region. Besides the SP compatibility, the design also provides strain relaxation in the QWs which improves the IQE. For this purpose, a nanosphere lithography (NSL) process was employed to form nanopillar structures with subsequent surface treatment and passivation techniques to cure dry-etch damages.

To form Ag NPs, an Ag TF was deposited on the nanopillar structures followed by thermal annealing. This approach, however, resulted in a significant PL quenching from the Ag NPs despite using a SiN passivation layer on the side-walls. The PL quenching was believed to be consequence of surface states from metal particles, in addition to small sized NPs (with insufficient scattering-to-absorption ratio) on the size-walls.

As opposed to the previously considered nanohole pattern in *p*-GaN, the space between the nanopillars can be filled with synthetic Ag NPs of uniform size which has been demonstrated to improve the emission from similar structures.[150] By controlling the dimensions and periodicity of the nanopillar structures, and tapping into the photonic crystral (PhC) properties, the LEE and the emission pattern can be optimized.[111]

8.5 Electrically driven SP-LED

As an initial step towards realizing an electrically driven SP enhanced LED device, special *p*-contact designs were investigated. The design consisted of a grid structure with isolated regions of *p*-GaN surface not covered by the *p*-contact (SP-regions), where it would be possible to deposit SP-metal disconnected from the *p*-contact. Using a conventional LED epi-structure, the *p*-GaN layer was seen to provide enough current spreading to enable efficient light emission from the SP-regions. With a *p*-GaN thickness of 30 nm, however, a poor current spreading was observed and the emission from the SP-regions was seen to be weak in comparison to the region covered by the *p*-contact metal grid.

The insufficient current spreading in the thin *p*-GaN posed a challenge for SP coupling with the QWs when Ag NPs were coated on the SP-regions. Although a small enhancement could be observed due to the NPs, the poor current injection into the SP-region limited the SP enhancement capabilities.

These results suggest, that in order to apply surface plasmonics with an electrically driven device, a different *p*-contact designs has to be used. The different *p*-contact design could consist of a transparent conductive oxide (TCO) coated over Ag NPs on the *p*-GaN surface. Alternatively, the *p*-GaN layer thickness

could be increased just enough to enable efficient current spreading while at the same time allowing for SP-QW coupling, which has been shown to be possible with 50 nm *p*-GaN.[60]

An important issue regarding SP-LEDs is the long term stability of the surface plasmonic metals deposited to enhance the emission. Furthermore, it is of high interest to investigate the SP-metal enhancement at the final stages of an LED fabrication process, i.e. after dicing and packaging. If the metal NPs are not protected, their performance could be affected during this final processing. It is also interesting to investigate the SP induced enhancement during the lifespan of the LED device, and to see whether such improvements are stable. Commercial LEDs are today boasting with lifetimes above 50.000 hours, hence for SP-LEDs to be industrially feasible, their lifetime and stability must be able to compete with currently existence products.

Acronyms

AFM atomic-force microscope

AZO Al-doped ZnO

CM center-of-mass

CSL current spreading layer

DOS density of states

EL electroluminescence

EQE external quantum efficiency

FDTD finite-different time-domain

FOM figure-of-merit

FWHM full width at half maximum

GZO Ga-doped ZnO

HF hydrofluoric acid

HCl hydrochloric acid

ICP inductively-coupled plasma

IPLE integrated PL enhancement

IQE internal quantum efficiency

ITO indium tin oxide

LED light-emitting diode

LEE light extraction efficiency

LSP localized surface plasmon

LSPR localized surface plasmon resonance

LT low temperature

MOVPE metalorganic vapor-phase epitaxy

MQW multiple quantum-well

NIL nanoimprint lithography

NH nanohole

NP nanoparticle

NR nano-rod

NS nanosphere

NSL nanosphere lithography

PECVD plasma-enhanced chemical vapour deposition

PhC photonic crystral

PL photoluminescence

PR photoresist

PS polystyrene

QCSE quantum-confined Stark effect

QD quantum-dot

QW quantum-well

RIE reactive-ion etching

RMS root-mean-square

RT room temperature

RTA rapid thermal annealing

SEM scanning electron microscope

SER scattering-to-extinction ratio

SL super-lattice

SP surface plasmon

SPP surface plasmon polariton

TCO transparent conductive oxide

TD threading dislocation

TF thin film

TIR total internal reflection

TRPL time-resolved PL

XPS x-ray photoelectron spectroscopy

Bibliography

1. Amano, H, Kito, M & Hiramatsu, K. P-type conduction in Mg-doped GaN treated with low-energy electron beam irradiation (LEEBI). *Jpn. J. Appl. Phys* **28,** L2112–L2114 (1989).
2. Round, H. J. A Note on Carborundum. *Electr. World* **19,** 309 (1907).
3. Amano, H. *et al.* Metalorganic vapor phase epitaxial growth of a high quality GaN film using an AlN buffer layer. *Appl. Phys. Lett.* **48,** 353 (1986).
4. Nakamura, S. & Krames, M. R. History of gallium-nitride-based light- emitting diodes for illumination. *Proc. IEEE* **101,** 2211–2220 (2013).
5. Saleh, B. E. A. & Teich, M. C. *Fundamentals of Photonics* 2nd ed. (Wiley, 2007).
6. Jain, S. C. *et al.* III-nitrides: Growth, Characterization and Properties. *Appl. Phys. Rev.* **87** (2000).
7. Nakamura, S., Mukai, T. & Senoh, M. Si- and Ge-Doped GaN Films Grown with GaN Buffer Layers. *Jpn. J. Appl. Phys.* **31,** 2883–2888 (1992).
8. Nakamura, S. *et al.* Thermal Annealing Effects on P-Type Mg-Doped GaN Films. *Jpn. J. Appl. Phys.* **31,** L139–L142 (1992).
9. Schubert, E. F. *Light-Emitting Diodes* 2nd ed. (Cambridge, 2006).
10. Teisseyre, H. *et al.* Temperature dependence of the energy gap in GaN bulk single crystals and epitaxial layer. *J. Appl. Phys.* **76,** 2429–2434 (1994).
11. Guo, Q. & Yoshida, A. Temperature dependence of band gap change in InN and AlN. *Japanese J. Appl. Physics, Part 1 Regul. Pap. Short Notes Rev. Pap.* **33,** 2453–2456 (1994).
12. Davydov, V. Y. *et al.* Absorption and emission of hexagonal InN. Evidence of narrow fundamental band gap. *Phys. Status Solidi Basic Res.* **229,** 1972–1974 (2002).
13. Wu, J. *et al.* Unusual properties of the fundamental band gap of InN. *Appl. Phys. Lett.* **80,** 3967–3969 (2002).
14. Wu, J. *et al.* Universal bandgap bowing in group-III nitride alloys. *Solid State Commun.* **127,** 411–414 (2003).
15. Walukiewicz, W. *et al.* Optical properties and electronic structure of InN and In-rich group III-nitride alloys. *J. Cryst. Growth* **269,** 119–127 (2004).

16. Ohkawa, K. *et al.* 740-nm emission from InGaN-based LEDs on c-plane sapphire substrates by MOVPE. *Journal of Crystal Growth* **343,** 13–16 (2012).

17. Yamada, M. *et al.* InGaN-Based Near-Ultraviolet and Blue-Light-Emitting Diodes with High External Quantum Efficiency Using a Patterned Sapphire Substrate and a Mesh Electrode. *Jpn. J. Appl. Phys.* **41,** L1431–L1433 (2002).

18. Narukawa, Y. *et al.* Improvement of luminous efficiency in white light emitting diodes by reducing a forward-bias voltage. *Japanese J. Appl. Physics, Part 2 Lett.* **46,** 48–51 (2007).

19. Nakamura, S. GaN Growth Using GaN Buffer Layer. *Jpn. J. Appl. Phys.* **30,** L1705–L1707 (1991).

20. Lü, W *et al.* Generation and behavior of pure-edge threading misfit dislocations in InGaN/GaN multiple quantum wells in InGaN/GaN multiple quantum wells. *J. Appl. Phys.* **96,** 5267–5270 (2004).

21. Hino, T. *et al.* Characterization of threading dislocations in GaN epitaxial layers. *Appl. Phys. Lett.* **76,** 3421 (2000).

22. Nikishin, S. a. *et al.* High quality GaN grown on Si(111) by gas source molecular beam epitaxy with ammonia. *Appl. Phys. Lett.* **75,** 2073 (1999).

23. Wang, H. M. *et al.* AlN/AlGaN superlattices as dislocation filter for low-threading-dislocation thick AlGaN layers on sapphire. *Appl. Phys. Lett.* **81,** 604–606 (2002).

24. Wang, C. L. *et al.* Influence of AlGaN/GaN superlattice inserted structure on the performance of InGaN/GaN multiple quantum well light emitting diodes. *Mater. Sci. Eng. B Solid-State Mater. Adv. Technol.* **138,** 180–183 (2007).

25. Nakamura, S., Mukai, T. & Senoh, M. In situ monitoring and Hall measurements of GaN grown with GaN buffer layers. *J. Appl. Phys.* **71,** 5543–5549 (1992).

26. Kumakura, K. *et al.* Minority carrier diffusion length in GaN: Dislocation density and doping concentration dependence. *Appl. Phys. Lett.* **86,** 1–3 (2005).

27. Takeuchi, T. *et al.* Quantum-Confined Stark Effect due to Piezoelectric Fields in GaInN Strained Quantum Wells. *Jpn. J. Appl. Phys.* **382,** L382 (1997).

28. Takeuchi, T., Amano, H. & Akasaki, I. Theoretical study of orientation dependence of piezoelectric effects in wurtzite strained GaInN/GaN heterostructures and quantum wells. *Japanese J. Appl. Physics* **39,** 413–416 (2000).

29. Nakamura, S. The Roles of Structural Imperfections in InGaN-Based Blue Light-Emitting Diodes and Laser Diodes. *Science* **281,** 956–961 (1998).

30. Narukawa, Y. *et al.* White light emitting diodes with super-high luminous efficacy. *J. Phys. D. Appl. Phys.* **43,** 354002 (2010).

31. Maranowski, S. A. *et al.* High-performance AlGaInP light-emitting diodes. *Proc. SPIE* **3002,** 110–118 (1997).

32. Peter, M. *et al.* Green ThinGaN power-LED demonstrates 100 lm. *Phys. Status Solidi Curr. Top. Solid State Phys.* **5,** 2050–2052 (2008).

33. Schiavon, D. *et al.* Optically pumped GaInN/GaN multiple quantum wells for the realization of efficient green light-emitting devices. *Appl. Phys. Lett.* **102** (2013).

34. Maier, S. A. *Plasmonics: Fundamentals and Applications* first (Springer US, 2007).

35. Bagchi, A. *et al.* Measurement of Surface-Plasmon Dispersion in Aluminum by Inelastic Low-Energy Electron Diffraction. *Phys. Rev. Lett.* **27,** 998–1001 (15 1971).

36. Liebsch, A. Surface plasmon dispersion of Ag. *Phys. Rev. Lett.* **71,** 145–148 (1 1993).

37. Gontijo, I, Boroditsky, M & Yablonovitch, E. Coupling of InGaN quantum-well photoluminescence to silver surface plasmons. *Phys. Rev. B* **60,** 564–567 (1999).

38. Neogi, A. *et al.* Enhancement of spontaneous recombination rate in a quantum well by resonant surface plasmon coupling. *Phys. Rev. B* **66,** 1–4 (2002).

39. Okamoto, K. *et al.* Surface-plasmon-enhanced light emitters based on InGaN quantum wells. *Nat. Mater.* **3,** 601–5 (2004).

40. Kwon, M.-K. *et al.* Surface-Plasmon-Enhanced Light-Emitting Diodes. *Adv. Mater.* **20,** 1253–1257 (2008).

41. Zhang, Z.-h. *et al.* Improved InGaN/GaN light-emitting diodes with spreading layer. *Opt. Express* **21,** 1066–1072 (2013).

42. Lee, I.-H., Jang, L.-W. & Polyakov, A. Y. Performance enhancement of GaN-based light emitting diodes by the interaction with localized surface plasmons. *Nano Energy* **13,** 140–173 (2015).

43. Lu, C.-H. *et al.* Enhancement of Green Emission from InGaN/GaN Multiple Quantum Wells via Coupling to Surface Plasmons in a Two-Dimensional Silver Array. *Adv. Funct. Mater.* **21,** 4719–4723 (2011).

44. Jiang, S. *et al.* Fabrication and Effects of Ag Nanoparticles Hexagonal Arrays in Green LEDs by Nanoimprint. *IEEE Photonics Technol. Lett.* **27,** 1363–1366 (2015).

45. Zhang, H. *et al.* Surface-plasmon-enhanced GaN-LED based on a multilayered M-shaped nano-grating. *Opt. Express* **21,** 13492–13501 (2013).

46. Cho, C.-Y. *et al.* Surface plasmon-enhanced light-emitting diodes using silver nanoparticles embedded in p-GaN. *Nanotechnology* **21,** 205201 (2010).

47. Cho, C.-Y. *et al.* Surface plasmon-enhanced light-emitting diodes with silver nanoparticles and SiO2 nano-disks embedded in p-GaN. *Appl. Phys. Lett.* **99,** 041107 (2011).

48. Jang, L.-W. *et al.* Enhanced light output of InGaN/GaN blue light emitting diodes with Ag nano-particles embedded in nano-needle layer. *Opt. Express* **20,** 6036–41 (2012).

49. Cao, X. a. *et al.* Electrical effects of plasma damage in p-GaN. *Appl. Phys. Lett.* **75,** 2569–2571 (1999).

50. Lee, J.-M. *et al.* Dry-etch damage and its recovery in InGaN/GaN multiquantum-well light-emitting diodes. *Semicond. Sci. Technol.* **18,** 530–534 (2003).

51. Kim, D. J. *et al.* Thermal activation energies of Mg in GaN : Mg measured by the Hall effect and admittance spectroscopy. *J. Appl. Phys.* **88,** 2564–2569 (2000).

52. Schmeits, M., Nguyen, N. D. & Germain, M. Competition between deep impurity and dopant behavior of Mg in GaN Schottky diodes. *J. Appl. Phys.* **89,** 1890–1897 (2001).

53. Okamoto, K. *et al.* Surface plasmon enhanced spontaneous emission rate of InGaN∕GaN quantum wells probed by time-resolved photoluminescence spectroscopy. *Appl. Phys. Lett.* **87,** 071102 (2005).

54. Yeh, D.-M. *et al.* Surface plasmon coupling effect in an InGaN∕GaN single-quantum-well light-emitting diode. *Appl. Phys. Lett.* **91,** 171103 (2007).

55. Paiella, R. Tunable surface plasmons in coupled metallo-dielectric multiple layers for light-emission efficiency enhancement. *Appl. Phys. Lett.* **87,** 111104 (2005).

56. Henson, J. *et al.* Controlling the recombination rate of semiconductor active layers via coupling to dispersion-engineered surface plasmons. *Opt. Soc. Am. B* **25,** 1328–1335 (2008).

57. Khurgin, J. B., Sun, G. & Soref, R. a. Enhancement of luminescence efficiency using surface plasmon polaritons: figures of merit. *J. Opt. Soc. Am. B* **24,** 1968 (2007).

58. Yeh, D.-M. *et al.* Formation of various metal nanostructures with thermal annealing to control the effective coupling energy between a surface plasmon and an InGaN/GaN quantum well. *Nanotechnology* **18,** 265402 (2007).

59. Yeh, D.-M. *et al.* Localized surface plasmon-induced emission enhancement of a green light-emitting diode. *Nanotechnology* **19,** 345201 (2008).

60. Lin, C.-h. *et al.* Further reduction of efficiency droop effect by adding a lower-index dielectric interlayerin a surface plasmon coupled blue light-emitting diode with surface metalnanoparticles. *Appl. Phys. Lett.* **105,** 101106 (2014).

61. Lin, C.-H. *et al.* Modulation behaviors of surface plasmon coupled light-emitting diode. *Opt. Express* **23,** 8150 (2015).

62. Zhu, S.-C. *et al.* Enhancement of the modulation bandwidth for GaN-based light-emitting diode by surface plasmons. *Opt. Express* **23,** 13752 (2015).

63. Sun, G., Khurgin, J. B. & Soref, R. a. Plasmonic light-emission enhancement with isolated metal nanoparticles and their coupled arrays. *J. Opt. Soc. Am. B* **25,** 1748 (2008).

64. Henson, J. *et al.* Plasmon enhanced light emission from InGaN quantum wells via coupling to chemically synthesized silver nanoparticles. *Appl. Phys. Lett.* **95,** 151109 (2009).

65. Kuzma, A. *et al.* Influence of surface oxidation on plasmon resonance in monolayer of gold and silver nanoparticles. *J. Appl. Phys.* **112,** 103531 (2012).

66. Jang, L.-w. *et al.* Localized surface plasmon enhanced quantum efficiency of InGaN/GaN quantum wells by Ag/SiO2 nanoparticles. *Opt. Express* **20,** 2116–2123 (2012).

67. Jensen, T. R. *et al.* Nanosphere Lithography: Tunable Localized Surface Plasmon Resonance Spectra of Silver Nanoparticles. *J. Phys. Chem. B* **104,** 10549–10556 (2000).

68. Tan, B. J. Y. *et al.* Fabrication of Size-Tunable Gold Nanoparticles Array with Nanosphere Lithography, Reactive Ion Etching, and Thermal Annealing. *J. Phys. Chem. B,* 11100–11109 (2005).

69. Mak, G. Y. *et al.* Metallic nanoparticle array on GaN by microsphere lithography. *Phys. Status Solidi* **6,** S654–S657 (2009).

70. Mochizuki, Y. *et al.* Enhancement of photoluminescence from silicon nanocrystals by metal nanostructures made by nanosphere lithography. *J. Appl. Phys.* **106,** 013517 (2009).

71. Huang, C.-W. *et al.* Fabrication of surface metal nanoparticles and their induced surface plasmon coupling with subsurface InGaN/GaN quantum wells. *Nanotechnology* **22,** 475201 (2011).

72. Henson, J. *et al.* Enhanced near-green light emission from InGaN quantum wells by use of tunable plasmonic resonances in silver nanoparticle arrays. *Opt. Express* **18,** 21322–9 (2010).

73. Henson, J. *et al.* Plasmon-enhanced light emission based on lattice resonances of silver nanocylinder arrays. *Opt. Lett.* **37,** 79–81 (2012).

74. Sung, J.-H. *et al.* Enhancement of electroluminescence in GaN-based light-emitting diodes by metallic nanoparticles. *Appl. Phys. Lett.* **96,** 261105 (2010).

75. Zuloaga, J. & Nordlander, P. On the energy shift between near-field and far-field peak intensities in localized plasmon systems. *Nano Lett.* **11,** 1280–1283 (2011).

76. Mertens, H., Koenderink, a. & Polman, a. Plasmon-enhanced luminescence near noble-metal nanospheres: Comparison of exact theory and an improved Gersten and Nitzan model. *Phys. Rev. B* **76,** 115123 (2007).

77. Watanabe, S. *et al.* Internal quantum efficiency of highly-efficient InxGa1-xN-based near-ultraviolet light-emitting diodes. *Appl. Phys. Lett.* **83,** 4906–4908 (2003).

78. Zheng, C. *et al. Enhancing Light Output of GaN-based Light-emitting Diodes with Nanoparticle-assembled on-top Layers* in *Nano/Micro Eng. Mol. Syst.* (2012), 376–379.

79. Lu, Y.-C. *et al.* Temperature dependence of the surface plasmon coupling with an InGaN/GaN quantum well. *Appl. Phys. Lett.* **90,** 193103 (2007).

80. Lee, Y.-j. *et al.* Study of the Excitation Power Dependent Internal Quantum Efficiency in InGaN/GaN LEDs Grown on Patterned Sapphire Substrate. *IEEE J. Sel. Top. Quantum Electron.* **15,** 1137–1143 (2009).

81. Della Sala, F. *et al.* Free-carrier screening of polarization fields in wurtzite GaN/InGaN laser structures. *Appl. Phys. Lett.* **74,** 2002 (1999).

82. Kuroda, T. & Tackeuchi, A. Influence of free carrier screening on the luminescence energy shift and carrier lifetime of InGaN quantum wells. *J. Appl. Phys.* **92,** 3071 (2002).

83. Jiang, S. *et al.* Resonant absorption and scattering suppression of localized surface plasmons in Ag particles on green LED. *Opt. Express* **21,** 12100–12110 (2013).

84. Chen, H.-S. *et al.* Surface plasmon coupled light-emitting diode with metal protrusions into p-GaN. *Appl. Phys. Lett.* **102,** 041108 (2013).

85. Lamprecht, B *et al.* Metal nanoparticle gratings: influence of dipolar particle interaction on the plasmon resonance. *Phys. Rev. Lett.* **84,** 4721–4 (2000).

86. Biteen, J. *et al.* Plasmon-Enhanced Photoluminescence of Silicon Quantum Dots: Simulation and Experiment. *J. Phys. Chem. C* **111,** 13372–13377 (2007).

87. Dulkeith, E. *et al.* Fluorescence Quenching of Dye Molecules near Gold Nanoparticles: Radiative and Nonradiative Effects. *Phys. Rev. Lett.* **89,** 203002 (2002).

88. Kulakovich, O. *et al.* Enhanced Luminescence of CdSe Quantum Dots on Gold Colloids. *Nano Lett.* **2,** 1449–1452 (2002).

89. Chen, T *et al.* Tailoring the photoluminescence of ZnO nanowires using Au nanoparticles. *Nanotechnology* **19,** 435711 (2008).

90. Cho, C.-Y. *et al.* Enhanced optical output power of green light-emitting diodes by surface plasmon of gold nanoparticles. *Appl. Phys. Lett.* **98,** 051106 (2011).

91. Kwon, M.-K., Kim, J.-Y. & Park, S.-J. Enhanced emission efficiency of green InGaN/GaN multiple quantum wells by surface plasmon of Au nanoparticles. *J. Cryst. Growth* **370,** 124–127 (2013).

92. Chen, Y. *et al.* Pit formation in GaInN quantum wells. *Applied Physics Letters* **72,** 710–712 (1998).

93. Iida, D. *et al.* Analysis of strain relaxation process in GaInN/GaN heterostructure by in situ X-ray diffraction monitoring during metalorganic vapor-phase epitaxial growth pss. **214,** 211–214 (2013).

94. Yamamoto, T. *et al.* In situ X-ray diffraction monitoring of GaInN/GaN superlattice during organometalic vapor phase epitaxy growth. *Journal of Crystal Growth* **393,** 108–113 (2014).

95. Hikosaka, T. *et al.* Impact of InGaN growth conditions on structural stability under high temperature process in InGaN/GaN multiple quantum wells. *Physica Status Solidi (C)* **8,** 2016–2018 (2011).

96. Sahonta, S.-L. *et al.* Properties of trench defects in InGaN/GaN quantum well structures. *Physica Status Solidi (a)* **210,** 195–198 (2013).

97. Massabuau, F. C.-P. *et al.* Morphological, structural, and emission characterization of trench defects in InGaN/GaN quantum well structures. *Applied Physics Letters* **101,** 212107–212107–4 (2012).

98. G.L Martinez, M.R. Curiel, B.J. Skromme, R. M. Surface Recombination and Sulfide Passivation of GaN. *Journal of Electronic Materials* **29,** 7 (2000).

99. Huh, C. *et al.* Effects of sulfur treatment on electrical and optical performance of InGaN/GaN multiple-quantum-well blue light-emitting diodes. *Applied Physics Letters* **78,** 1766 (2001).

100. Xi, J. Q. *et al.* Very low-refractive-index optical thin films consisting of an array of SiO2 nanorods. *Optics letters* **31,** 601–3 (2006).

101. Yan, X. *et al.* Deep-ultraviolet tailored- and low-refractive index antireflection coatings for light-extraction enhancement of light emitting diodes. *Journal of Applied Physics* **113,** 163105 (2013).

102. Byeon, K.-j. *et al.* Fabrication of SiN x -based photonic crystals on GaN-based LED devices with patterned sapphire substrate by nanoimprint lithography. *Optics Express* **20,** 11423–11432 (2012).

103. Shei, S. C. & Chu, M. H. SiNx nanopillars on GaN-based LED to enhance light-extraction efficiency by a successive ionic layer adsorption and reaction method. *Journal of Lightwave Technology* **31,** 2413–2418 (2013).

104. Yang, Y. & Cao, X. a. Removing plasma-induced sidewall damage in GaN-based light-emitting diodes by annealing and wet chemical treatments. *Journal of Vacuum Science & Technology B: Microelectronics and Nanometer Structures* **27,** 2337 (2009).

105. Huh, C. *et al.* Improved light-output and electrical performance of InGaN-based light-emitting diode by microroughening of the p-GaN surface. *Journal of Applied Physics* **93,** 9383 (2003).

106. Huang, H.-W. *et al.* Enhanced light output of an InGaN/GaN light emitting diode with a nano-roughened p-GaN surface. *Nanotechnology* **16,** 1844–1848 (2005).

107. Fujii, T. *et al.* Increase in the extraction efficiency of GaN-based light-emitting diodes via surface roughening. *Applied Physics Letters* **84,** 855 (2004).

108. Oder, T. N. *et al.* III-nitride blue and ultraviolet photonic crystal light emitting diodes. *Applied Physics Letters* **84,** 466–468 (2004).

109. Kim, S. H. *et al.* Fabrication of photonic crystal structures on light emitting diodes by nanoimprint lithography. *Nanotechnology* **18,** 055306 (2007).

110. Wierer, J. J. *et al.* InGaN/GaN quantum-well heterostructure light-emitting diodes employing photonic crystal structures. *Applied Physics Letters* **84,** 3885 (2004).

111. Wierer, J. J., David, A. & Megens, M. M. III-nitride photonics-crystal light-emitting diodes with high extraction efficiency. *Nature Photonics* **3,** 163–169 (2009).

112. Truong, T. a. *et al.* Light extraction from GaN-based light emitting diode structures with a noninvasive two-dimensional photonic crystal. *Applied Physics Letters* **94,** 023101 (2009).

113. Li, K. H. & Choi, H. W. InGaN light-emitting diodes with indium-tin-oxide photonic crystal current-spreading layer. *Journal of Applied Physics* **110,** 053104 (2011).

114. Keller, S. *et al.* Optical properties of GaN nanopillar and nanostripe arrays with embedded InGaN/GaN multi-quantum wells. *Journal of Applied Physics* **100,** 054314 (2006).

115. Ramesh, V. *et al.* Strain relaxation effect by nanotexturing InGaN/GaN multiple quantum well. *Journal of Applied Physics* **107,** 114303 (2010).

116. Bae, S.-y. *et al.* Size-controlled InGaN/GaN nanorod array fabrication and optical characterization. *Optics express* **21,** 16854 (2013).

117. Wang, Q *et al.* Influence of strain relaxation on the optical properties of InGaN/GaN multiple quantum well nanorods. *Journal of Physics D: Applied Physics* **44,** 395102 (2011).

118. Zhu, J. *et al.* Light extraction efficiency improvement and strain relaxation in InGaN/GaN multiple quantum well nanopillars. *Journal of Applied Physics* **109,** 1–6 (2011).

119. De-sheng, J. & Hai, W. Fabrication and Optical Characterization of GaN-Based Nanopillar Light Emitting Diodes. *Chinese Physics Letters* **3485,** 3485 (2008).

120. Chen, L.-Y. *et al.* High performance InGaN/GaN nanorod light emitting diode arrays fabricated by nanosphere lithography and chemical mechanical polishing processes. *Optics express* **18,** 7664–9 (2010).

121. Li, K. H. & Choi, H. W. Air-spaced GaN nanopillar photonic band gap structures patterned by nanosphere lithography. *Journal of Applied Physics* **109,** 023107 (2011).

122. Li, Q. *et al.* Optical performance of top-down fabricated InGaN/GaN nanorod light emitting diode arrays. *Optics express* **19,** 25528–34 (2011).

123. Dong, P. *et al.* Optical properties of nanopillar AlGaN/GaN MQWs for ultraviolet light-emitting diodes. *Optics Express* **22,** A320 (2014).

124. Kuo, C.-W. *et al.* Fabrication of Size-Tunable Large-Area Periodic Silicon Nanopillar Arrays with Sub-10-nm Resolution. *The Journal of Physical Chemistry B* **107,** 9950–9953 (2003).

125. Cheung, C. L. *et al.* Fabrication of nanopillars by nanosphere lithography. *Nanotechnology* **1339** (2006).

126. Reculusa, S. & Ravaine, S. Synthesis of Colloidal Crystals of Controllable Thickness through the Langmuir-Blodgett Technique. *Chemistry of Materials* **15,** 598–605 (2003).

127. Wong, S., Kitaev, V. & Ozin, G. a. Colloidal crystal films: advances in universality and perfection. *Journal of the American Chemical Society* **125,** 15589–98 (2003).

128. Kosiorek, A. *et al.* Fabrication of nanoscale rings, dots, and rods by combining shadow nanosphere lithography and annealed polystyrene nanosphere masks. *Small (Weinheim an der Bergstrasse, Germany)* **1,** 439–44 (2005).

129. Zhang, X. *et al.* Advances in Contemporary Nanosphere Lithographic Techniques. *Journal of Nanoscience and Nanotechnology* **6,** 1920–1934 (2006).

130. Zhou, H.-P., Zhang, C. & Yan, C.-H. Controllable assembly of diverse rare-earth nanocrystals via the Langmuir-Blodgett technique and the underlying size- and symmetry-dependent assembly kinetics. *Langmuir: The ACS journal of surfaces and colloids* **25,** 12914–25 (2009).

131. Ye, X. & Qi, L. Two-dimensionally patterned nanostructures based on monolayer colloidal crystals: Controllable fabrication, assembly, and applications. *Nano Today* **6,** 608–631 (2011).

132. Mihi, a., Ocaña, M. & Míguez, H. Oriented Colloidal-Crystal Thin Films by Spin-Coating Microspheres Dispersed in Volatile Media. *Advanced Materials* **18,** 2244–2249 (2006).

133. Jiang, P. & Mcfarland, M. J. Large-Scale Fabrication of Wafer-Size Colloidal Crystals , Macroporous Polymers and Nanocomposites by Spin-Coating. *Journal of the American Chemical Society* **126,** 13778–13786 (2004).

134. Jiang, P. & McFarland, M. J. Wafer-scale periodic nanohole arrays templated from two-dimensional nonclose-packed colloidal crystals. *Journal of the American Chemical Society* **127,** 3710–1 (2005).

135. Jiang, P. *et al.* Two-dimensional nonclose-packed colloidal crystals formed by spincoating. *Applied Physics Letters* **89,** 011908 (2006).

136. Chen, J. *et al.* Controllable fabrication of 2D colloidal-crystal films with polystyrene nanospheres of various diameters by spin-coating. *Applied Surface Science* **270,** 6–15 (2013).

137. Colson, P., Cloots, R. & Henrist, C. Experimental design applied to spin coating of 2D colloidal crystal masks: a relevant method? *Langmuir: The ACS journal of surfaces and colloids* **27,** 12800–6 (2011).

138. Sugiura, T. *et al.* Raman Scattering Study of InGaN Grown by Metalorganic Vapor Phase Epitaxy on (0001) Sapphire Substrates. *Japanese Journal of Applied Physics* **40,** 5955–5958 (2001).

139. Puech, P. *et al.* GaN nanoindentation: A micro-Raman spectroscopy study of local strain fields. *Journal of Applied Physics* **96,** 2853–2856 (2004).

140. Metson, J. B. *et al.* X-ray absorption spectroscopy in the analysis of GaN thin films. *Surface and Interface Analysis* **35,** 719–722 (2003).

141. King, S. W *et al.* Cleaning of AlN and GaN surfaces. *Journal of Applied Physics* **84,** 5248–5260 (1998).

142. Moulder, J. & Chastain, J. *Handbook of X-ray Photoelectron Spectroscopy: A Reference Book of Standard Spectra for Identification and Interpretation of XPS Data* (Physical Electronics Division, Perkin-Elmer Corporation, 1992).

143. Prabhakaran, K., Andersson, T. G. & Nozawa, K. Nature of native oxide on GaN surface and its reaction with Al. *Applied Physics Letters* **69,** 3212 (1996).

144. Li, D. *et al.* Selective etching of GaN polar surface in potassium hydroxide solution studied by x-ray photoelectron spectroscopy. *Journal of Applied Physics* **90,** 4219–4223 (2001).

145. Mishra, M. *et al.* Pits Assisted Oxygen Chemisorption on GaN Surfaces. *Phys. Chem. Chem. Phys.* **17,** 15201–15208 (2015).

146. Hong, S.-h. *et al.* Localized surface plasmon-enhanced near-ultraviolet emission from InGaN/GaN light- emitting diodes using silver and platinum nanoparticles. *Optics express* **21,** 3138–3144 (2013).

147. Hong, S.-H. *et al.* Enhanced optical output of InGaN/GaN near-ultraviolet light-emitting diodes by localized surface plasmon of colloidal silver nanoparticles. *Nanotechnology* **26,** 385204 (2015).

148. Cho, C.-Y. *et al.* Enhanced Emission Efficiency of GaN-Based Flip-Chip Light-Emitting Diodes by Surface Plasmons in Silver Disks. *Applied Physics Express* **5,** 122103 (2012).

149. Lee, K. J. *et al.* Enhanced optical output power by the silver localized surface plasmon coupling through side facets of micro-hole patterned InGaN/GaN light-emitting diodes. *Optics Express* **22,** A1051 (2014).

150. Yun, J.-h. *et al.* Enhanced optical properties in nanopillar light emitting diodes by coupling localized surface plasmon of Ag/SiO2 nanoparticles. *Applied Physics Express* **8,** 092002 (2015).

151. Lu, C.-F. *et al.* Reduction in the efficiency droop effect of a light-emitting diode through surface plasmon coupling. *Applied Physics Letters* **96,** 261104 (2010).

152. Kim, J. K. *et al.* Effect of surface treatment by (NH4)2Sx solution on the reduction of ohmic contact resistivity of p-type GaN. *Journal of Vacuum Science & Technology B: Microelectronics and Nanometer Structures* **17,** 497 (1999).

153. Kim, D. W. *et al.* A study of transparent indium tin oxide (ITO) contact to p-GaN. *Thin Solid Films* **398-399,** 87–92 (2001).

154. Lin, Y. C. *et al.* InGaN/GaN light emitting diodes with Ni/Au, Ni/ITO and ITO p-type contacts. *Solid-State Electronics* **47,** 849–853 (2003).

155. Chang, K. M., Chu, J. Y. & Cheng, C. C. Investigation of indium-tin-oxide ohmic contact to p-GaN and its application to high-brightness GaN-based light-emitting diodes. *Solid-State Electronics* **49,** 1381–1386 (2005).

156. Sheu, J.-K. *et al.* Ga-Doped ZnO Transparent Conductive Oxide Films Applied to GaN-Based Light-Emitting Diodes for Improving Light Extraction Efficiency. *IEEE Journal of Quantum Electronics* **44,** 1211–1218 (2008).

157. Ou, S. L. *et al.* Pulsed laser deposition of ITO/AZO transparent contact layers for GaN LED applications. *Optics Express* **19,** 16244 (2011).

158. Ho, J.-K. *et al.* Low-resistance ohmic contacts to p-type GaN. *Applied Physics Letters* **74,** 1275 (1999).

159. Su, S.-H. *et al.* InGaN/GaN light emitting diodes with Ni/Au mesh p-contacts. *Solid-State Electronics* **49,** 1905–1908 (2005).

160. Lee, M.-L., Sheu, J.-K. & Hu, C. C. Nonalloyed Cr/Au-based Ohmic contacts to n-GaN. *Applied Physics Letters* **91,** 182106 (2007).

161. Dobos, L. *et al.* Bilayer Cr/Au contacts on n-GaN. *Vacuum* **86,** 769–772 (2012).

162. Cho, H. K., Kim, S.-K. & Lee, J. S. An improved non-alloyed ohmic contact Cr/Ni/Au to n-type GaN with surface treatment. *Journal of Physics D: Applied Physics* **41,** 175107 (2008).

163. Nam, Y.-I. & Lee, B.-T. Investigation of Ti/Au and Ti 2 N/Ti/Au ohmic contacts to n-GaN films. *Semiconductor Science and Technology* **26,** 085014 (2011).

164. Wang, D. F. *et al.* Low-resistance Ti/Al/Ti/Au multilayer ohmic contact to n-GaN. *Journal of Applied Physics* **89,** 6214–6217 (2001).

165. Davydov, a. V. *et al.* Combinatorial optimization of Ti/Al/Ti/Au ohmic contacts to n-GaN. *Physica Status Solidi C: Conferences* **2,** 2551–2554 (2005).

166. Motayed, A. *et al.* Two-step surface treatment technique: Realization of nonalloyed low-resistance Ti/Al/Ti/Au ohmic contact to n-GaN. *Journal of Vacuum Science & Technology B: Microelectronics and Nanometer Structures* **22,** 663 (2004).

167. Koide, Y. *et al.* Effects of annealing in an oxygen ambient on electrical properties of ohmic contacts to p-type GaN. *Journal of Electronic Materials* **28,** 341–346 (1999).

$\sqrt{17}$
$+ \Omega \int \delta e^{i\pi} = -1$
{2.7182818284}ϑφέρτυθιοπσδφγηξκλ
$\chi^2 \sum \gg \approx \lambda$
$\sum !$